



저작자표시-비영리-변경금지 2.0 대한민국

이용자는 아래의 조건을 따르는 경우에 한하여 자유롭게

- 이 저작물을 복제, 배포, 전송, 전시, 공연 및 방송할 수 있습니다.

다음과 같은 조건을 따라야 합니다:



저작자표시. 귀하는 원저작자를 표시하여야 합니다.



비영리. 귀하는 이 저작물을 영리 목적으로 이용할 수 없습니다.



변경금지. 귀하는 이 저작물을 개작, 변형 또는 가공할 수 없습니다.

- 귀하는, 이 저작물의 재이용이나 배포의 경우, 이 저작물에 적용된 이용허락조건을 명확하게 나타내어야 합니다.
- 저작권자로부터 별도의 허가를 받으면 이러한 조건들은 적용되지 않습니다.

저작권법에 따른 이용자의 권리는 위의 내용에 의하여 영향을 받지 않습니다.

이것은 [이용허락규약\(Legal Code\)](#)을 이해하기 쉽게 요약한 것입니다.

[Disclaimer](#)

공학박사 학위논문

**A Study on Charge Collecting Property of
Semiconducting Oxide Materials in
Photoelectric Energy Conversion System**

광·전 에너지 변환 시스템 내 산화물 반도체 물질의
전하 수집 능력 제어에 관한 연구

2015년 8월

서울대학교 대학원

재료공학부

박종훈

**A Study on Charge Collecting Property of
Semiconducting Oxide Materials in
Photoelectric Energy Conversion System**

A THESIS SUBMITTED TO THE
DEPARTMENT OF MATERIALS SCIENCE AND ENGINEERING
SEOUL NATIONAL UNIVERSITY

FOR THE DEGREE OF DOCTOR OF PHILOSOPHY

BY
JONG HOON PARK

AUGUST 2015

Abstract

A Study on Charge Collecting Property of Semiconducting Oxide Materials in Photoelectric Energy Conversion System

Jong Hoon Park

Department of Materials Science and Engineering

College of Engineering

Seoul National University

Nanostructured transparent n-type and p-type semiconducting oxides were synthesized and designed for enhancing device performance in photoelectric energy conversion system. The synthesized nanostructures were used as photoelectrodes and applied to photovoltaic devices, particularly in emerging photovoltaic (PV) system. The correlation between structural/compositional design of the photoelectrodes and their charge collecting property was explored. Concretely, inorganic semiconductor sensitized solar cells (ISSCs) and organic-inorganic hybrid perovskite solar cells (PSCs), which are

acceptable as typical emerging PVs in economic terms for environment conservation and energy generation, were studied. These ISSCs and PSCs currently face significant challenges in improving energy conversion efficiency and environmental stability. Since n-type and p-type semiconducting oxide based photoelectrodes are essential in charge collecting ability of photovoltaic devices, control and design of fundamental properties of semiconducting oxides are needed to overcome the above challenges. From this point of view, this thesis proposes two strategies for efficient charge collecting property in ISSCs and PSCs. First is structural design of semiconducting oxides. Second is compositional design of semiconducting oxides for effective charge injection from light absorbers to electron acceptors.

First, n-type titanium dioxide (TiO_2) and p-type nickel oxide (NiO) semiconducting oxides were explored to investigate the structural effect on electron-hole recombination and overall charge collecting property in emerging PV devices. For TiO_2 , hierarchically organized nano-architectures containing both large surface area and open channels of pores were synthesized on glass substrates using pulsed laser deposition (PLD) system. Growth mechanism of the architectures was studied and their charge collecting property in ISSCs was investigated. It was found that the morphology of photoelectrode strongly influenced the device performance. The open channels of pores between the TiO_2 domains which generated by the unique form of the architecture induced the infiltration of inorganic semiconductors (IS) and liquid polysulfide electrolytes more rapidly, resulting in higher light harvesting (efficient absorption of IS) and longer electron

lifetime compared to the conventional TiO₂ nanoparticle film. The enhanced light harvesting and charge collecting property led to the enhancement of overall energy conversion efficiency of the devices. Additionally, the larger surface area of nano-architecture further enhanced the light harvesting efficiency. For NiO, highly transparent, (111)-preferred oriented, column-shaped nanostructured films were grown on glass substrates and the optimum microstructure of NiO as hole transporting layer (HTL) for PSCs was investigated using PLD system. The device performance was explored using a p-i-n type PSCs, which is based on NiO/MAPbI₃/PCBM configuration. Compared to that of densely-packed NiO thin film or porous film, the overall efficiency was significantly enhanced with the nanostructured NiO film. The enhanced performance was attributed to the suppressed recombination rate during the extraction and transportation of the dissociated carriers.

Second, compositional design of TiO₂ nanostructured films was explored to enhance the charge injection property between light absorbing materials and electron accepting semiconducting oxides in ISSCs. From the basis that the energy difference between the conduction band (CB) of IS and TiO₂ serves as the driving force for electron injection and that the doping metal cation into TiO₂ lattice alters the CB position of TiO₂, the enhanced charge injection ability of TiO₂ was expected by Niobium (Nb) doping. The relationship between the Nb doping and their effects on the final photovoltaic device performance were investigated. As a consequence, the generated photocurrents were greatly improved by Nb doping compared to the undoped ISSC. The enhanced photocurrents and overall energy conversion efficiency

were attributed to the efficient electron injection between IS and Nb doped TiO₂, resulted from the enlarged energy difference of the CB edge between IS and TiO₂ by introduction of Nb dopants.

This thesis focused on understanding of the relation between the structural/compositional design of semiconducting oxides and their effect on charge collecting property in photoelectric energy conversion system. Through the study, this thesis proposes a guideline of designing the semiconducting oxide based photoelectrode and a possibility to solve the faced challenges in the fields of emerging PVs.

Keywords: Charge collecting property, Semiconducting oxide, Nanostructure, Hierarchical, Pulsed laser deposition, Photoelectric energy conversion, Inorganic semiconductor solar cells, Perovskite solar cells, Doping, CdS, CdSe, PbS, CH₃NH₃PbI₃, TiO₂, NiO

Student Number: 2008-22848

Table of Contents

Abstract.....	i
Table of Contents.....	v
List of Tables.....	ix
List of Figures.....	xi
Chapter 1. Introduction	1
1.1. Overview: Semiconducting Oxide Materials in Photoelectric Energy Conversion System.....	1
1.2. Aim and Strategies.....	6
1.3. Bibliography	9
Chapter 2. Background and Literature Review.....	11
2.1. Emerging Photovoltaics (PVs).....	11
2.1.1. History of Solar Cells	11
2.1.2. Operating Principles of the Emerging PVs	13
2.1.3. Inorganic Semiconductor Sensitized Solar Cells	16
2.1.4. Perovskite Solar Cells	13
2.2. Nanostructured Materials by Pulsed Laser Deposition.....	33
2.2.1. Pulsed Laser Deposition	33
2.2.2. Synthesis of Nanostructured Materials by PLD.....	35
2.3. Materials.....	40

2.3.1.	Titanium Dioxide (TiO ₂).....	40
2.3.2.	Nickel Oxide (NiO).....	43
2.4.	Bibliography.....	46
Chapter 3. Experiments		55
3.1.	Synthesis of Nanostructured Semiconducting Oxides.....	55
3.1.1.	TiO ₂ and Nb doped TiO ₂ Anatase Film.....	55
3.1.2.	NiO.....	56
3.2.	Preparation of Light Absorbing Materials	55
3.2.1.	Successive Ionic Layer Adsorption and Reaction of Light Absorbing Inorganic Semiconducting Materials	58
3.2.2.	Preparation of Methyl-ammonium Lead Iodide.....	60
3.3.	Device Fabrication.....	61
3.3.1.	Inorganic Semiconductor Sensitized Solar Cells	61
3.3.2.	Perovskite Solar Cells	61
3.4.	Characterizations	62
3.4.1.	Inorganic Semiconductor Sensitized Solar Cells	62
3.4.2.	Perovskite Solar Cells	63
3.5.	Bibliography	65
Chapter 4. Structural/Compositional Design of <i>n-type</i> Semiconducting Oxide.....		66
4.1.	Hierarchically Organized <i>n-type</i> TiO ₂ Architecture for Highly Efficient Inorganic Semiconductor Sensitized Solar Cells ...	66

4.1.1.	Introduction.....	66
4.1.2.	Characterization of the PLD-TiO ₂ Architecture.....	68
4.1.3.	Photovoltaic Performances of PLD-TiO ₂ and NP-TiO ₂	84
4.1.4.	Conclusion	98
4.1.5.	Bibliography	99
4.2.	Band Engineering of <i>n-type</i> TiO ₂ Electron Collecting Material by Nb Doping in Inorganic Semiconductor Sensitized Solar Cells.....	103
4.2.1.	Introduction.....	103
4.2.2.	Characterization of the Nb-doped TiO ₂ Nanostructured Films	106
4.2.3.	Photovoltaic Performances of Undoped and Nb-doped TiO ₂ Photoelectrodes.....	115
4.2.4.	Conclusion	128
4.2.5.	Bibliography	129
Chapter 5.	Structural Design of <i>p-type</i> Semiconducting Oxide	132
5.1.	Nanostructured <i>p-type</i> NiO as an Efficient Hole Collecting Layer in Inverted Perovskite Solar Cells	132
5.1.1.	Introduction.....	132
5.1.2.	Characterization of NiO Nanostructures.....	136
5.1.3.	Photovoltaic Performances of Perovskite Solar Cells Based on NiO as Hole Collecting Layer	143

5.1.4. Conclusion	163
5.1.5. Bibliography	164
Chapter 6. Conclusion.....	168
Abstract (in Korean).....	176
Research Achievements.....	180

List of Tables

Table 2.3.1 Crystal structures and properties for 3 common TiO ₂ polymorphs. [2.83]	45
Table 4.1.2.1 Photovoltaic parameters of CSSCs as a function of the oxygen gas pressure and the thickness.	82
Table 4.1.2.2 Photovoltaic parameters of CSSCs as a function of the thickness	83
Table 4.1.3.1 Photovoltaic parameters of CSSCs using PLD-TiO ₂ and conventional NP-TiO ₂ with different numbers of CdSe SILAR cycles.	95
Table 4.1.3.2 The amount of deposited Cd ions measured by Inductively Coupled Plasma (ICP) analysis on the NP and PLD-TiO ₂ photoelectrodes. CdS/CdSe-deposited electrodes were prepared with same area and thickness. The prepared samples were analyzed three times and averaged	96
Table 4.1.3.3 Internal surface area of PLD and NP-TiO ₂ films measured by Brunauer-Emmett-Teller (BET) method.....	97
Table 4.2.3.1 Photovoltaic parameters of prepared ISSCs using undoped and Nb-doped TiO ₂ films as the photoelectrode.....	127
Table 5.1.3.1 Photovoltaic parameters of PLD-NiO based perovskite solar cells as a function of oxygen partial pressure.....	160

Table 5.1.3.2 Photovoltaic parameters of perovskite solar cells using dense NiO _x films with different deposition time (thickness)	161
Table 5.1.3.3 Photovoltaic parameters of PLD-NiO based perovskite solar cells as a function of film thickness.....	162

List of Figures

Figure 1.1.1	The latest chart on record solar cell efficiencies (2015). [1.3]....	5
Figure 2.1.1	Schematic illustration of operating principles of a solar cell	26
Figure 2.1.2	Device configuration of a typical ISSC	27
Figure 2.1.3	Band energy levels of various inorganic semiconductor based light absorbers used in ISSCs. [2.28].....	28
Figure 2.1.4	Band energy levels of various metal halide based light absorbers used in PSCs. [2.28]	29
Figure 2.1.5	Crystal structure of cubic metal halide perovskites with the chemical formula ABX_3 . Organic cations occupy position A and inorganic metal cations occupy position B whereas halide anions occupy X position. [2.48]	30
Figure 2.1.6	Schematic illustrations for the two different type of PSC architectures which classified by the photoelectrode structure...	31
Figure 2.1.7	The PSC device structures based on n-i-p and p-i-n structure ..	32
Figure 2.2.1	Schematic illustration of general PLD system	38
Figure 2.2.2	Synthesis of nanostructured film using PLD system. [2.75].....	39
Figure 3.1.1	Schematic image of pulsed laser deposition (PLD) system	57
Figure 4.1.2.1	(a) Cross-sectional view and (b) plane view field emission scanning electron microscopy (FESEM) images, (c) high resolution transmission electron microscopy (HRTEM) images	

and (d) selected area diffraction (SAD) patterns of bare TiO ₂ nanostructured films synthesized by pulsed laser deposition (PLD) method	74
Figure 4.1.2.2 X-ray diffraction (XRD) patterns of bare, CdS and CdSe sensitized PLD-TiO ₂ films. CdS and CdSe were deposited by successive ionic layer adsorption and reaction (SILAR) method.	75
Figure 4.1.2.3 TEM images of (a) bare, (b) CdS sensitized and (c) CdS/CdSe co-sensitized PLD-TiO ₂ and (d) energy dispersive X-ray spectroscopy (EDS) elemental mapping images of Ti, O, Cd, S and Se elements in CdS/CdSe co-sensitized PLD-TiO ₂ sample. This indicates that the CdS and CdSe are well deposited onto TiO ₂ films	76
Figure 4.1.2.4 EDS elemental mapping images of Cd, S, Se, and Zn elements across the cross section of PLD-TiO ₂ films.....	77
Figure 4.1.2.5 XRD patterns of PLD-TiO ₂ films synthesized on glass/fluorine doped tin oxide (FTO) substrate as a function of oxygen pressure	78
Figure 4.1.2.6 Cross sectional FESEM images of PLD-TiO ₂ films synthesized at (a, b) 50 mTorr, (c, d) 100 mTorr, (e, f) 150 mTorr, (g, k) 200 mTorr and (i, j) 300 mTorr. (k) Cross sectional FESEM images of conventional TiO ₂ nanoparticle film.....	79
Figure 4.1.2.7 (a) The photocurrent density-voltage (<i>J-V</i>) curves and (b) electrochemical impedance spectroscopy (EIS) of CSSCs using	

PLD-TiO ₂ films with the oxygen pressures of 50, 100, 150, 200 and 300mTorr. EIS spectra of CSSCs were measured at open circuit potential under light illumination (100mW/cm ²)	80
Figure 4.1.2.8 <i>J</i> - <i>V</i> curves of CSSCs fabricated from PLD-TiO ₂ films with different film thickness	81
Figure 4.1.3.1 <i>J</i> - <i>V</i> curves of CSSCs using PLD-TiO ₂ and conventional NP-TiO ₂ photoelectrodes with different CdSe SILAR cycles.....	89
Figure 4.1.3.2 Histogram of solar cell parameters of CSSCs based on CdS/CdSe co-sensitized PLD-TiO ₂ (72 cells) and NP-TiO ₂ films (38 cells).....	90
Figure 4.1.3.3 (a) External quantum efficiency (EQE) curves of solar cells based on CdS/CdSe deposited PLD-TiO ₂ and NP-TiO ₂ films. (b) UV-Vis absorption spectra of CdS/CdSe adsorbed PLD-TiO ₂ and NP-TiO ₂ films.....	91
Figure 4.1.3.4 Absorbed photon to current efficiency (APCE) curves of CSSCs based on CdS/CdSe co-sensitized PLD-TiO ₂ and NP-TiO ₂ films.....	92
Figure 4.1.3.5 (a) Electron transport time and (b) electron lifetime of prepared CSSCs measured by intensity-modulated photocurrent spectroscopy (IMPS) and intensity-modulated photovoltage spectroscopy (IMVS). (c) EIS spectra of CSSCs based on CdS/CdSe co-sensitized PLD-TiO ₂ and NP-TiO ₂ films. EIS spectra of CSSCs were measured at open circuit potential under light illumination (100mW/cm ²).....	93

Figure 4.1.3.6 Effect of the open channels of pores on the infiltration of polysulfide electrolyte into the TiO ₂ electrode. Scheme on the left is an illustration of conventional NP-TiO ₂ film and the right is the vertically aligned column-like nanostructured film synthesized by PLD	94
Figure 4.2.2.1 Cross-sectional FESEM images (a, e) undoped and (b, f) 0.5, (c, g) 1.0 and (d, h) 1.5 at% Nb doped TiO ₂ films synthesized by PLD method. HRTEM images of (i) undoped and (j) 0.5 at% Nb doped TiO ₂ films. The inset images in (i) and (j) indicates the SAD patterns of undoped and 0.5 at% Nb-doped TiO ₂ , respectively	109
Figure 4.2.2.2 XRD patterns of undoped and Nb-doped (0.5, 1.0 and 1.5 at%) TiO ₂ films	110
Figure 4.2.2.3 XRD patterns of PbS and PbS/CdS-sensitized Nb-doped TiO ₂ films	111
Figure 4.2.2.4 Electron probe micro-analyzer (EPMA) data of prepared Nb-doped TiO ₂ targets (filled circles) and the deposited Nb-doped TiO ₂ films (hollow circles) as a function of Nb concentration ..	112
Figure 4.2.2.5 X-ray photoelectron spectroscopy (XPS) spectra of (a) Ti 2p and (b) Nb 3d peaks obtained for undoped and Nb-doped TiO ₂ films	113
Figure 4.2.2.6 Mott–Schottky plots of the undoped, 0.5, 1.0 and 1.5 at% Nb-doped TiO ₂ films. The Mott–Schottky analysis was performed in a three-electrode cell. The TiO ₂ films were used as the working	

electrodes, a convoluted Pt-wire as the counter electrode and a saturated calomel electrode (SCE) as the reference electrode. An aqueous solution of 0.1M Na₂SO₄ was used as the electrolyte..114

Figure 4.2.3.1 The *J-V* curves of PbS/CdS-sensitized solar cells. The PbS and CdS were adsorbed with the SILAR cycles of 4 and 7, respectively and the thickness of the cells were fixed to 15µm. 121

Figure 4.2.3.2 Dark currents of prepared PbS/CdS-sensitized solar cells as a function of Nb doping concentration..... 122

Figure 4.2.3.3 EQE spectra of PbS/CdS-sensitized solar cells based on undoped and 0.5 at% Nb-doped TiO₂ films..... 123

Figure 4.2.3.4 Experimentally determined light harvesting efficiency (LHE) for the PbS/CdS sensitized Nb doped TiO₂ films 124

Figure 4.2.3.5 (a) Electron transport time and (b) electron lifetime of ISSCs based on undoped and 0.5 at% Nb doped TiO₂ films measured by IMPS and IMVS. A red light-emitting diode (LED, 627 nm) was used as the modulated light source and (c) the charge collection efficiency calculated with the IMPS and IMVS data..... 125

Figure 4.2.3.6 Schematic images and band diagram of PbS sensitized undoped and Nb doped TiO₂ nanostructures 126

Figure 5.1.2.1 Characterization of the NiO films prepared by pulsed laser deposition (PLD) method at different oxygen partial pressures. (a) Cross-sectional and plane-view field emission scanning electron microscopy (FESEM) images and (b) transmittance spectra of the

NiO films. All the prepared films were deposited on glass/tin doped indium oxide (ITO) substrates	140
Figure 5.1.2.2 High resolution X-ray diffraction (HR-XRD) patterns of NiO films synthesized by PLD as a function of oxygen partial pressure	141
Figure 5.1.2.3 X-ray photoelectron spectroscopy (XPS) spectra of (a) Ni 2p _{3/2} and (b) O 1s peaks obtained for prepared NiO films.....	142
Figure 5.1.3.1 (a) XRD patterns of glass/ITO/NiO/methyl-ammonium lead iodide (MAPbI ₃) multi-layered film and (b) the diagram of the device configuration and energy levels of each layer. (c) FESEM images showing the complete device structure. The various layers are tinted with different colors.....	150
Figure 5.1.3.2 Photocurrent density-voltage (<i>J-V</i>) curves of perovskite solar cells based on PLD-NiO films, deposited at various oxygen partial pressures. The thickness for the NiO _x and PLD-NiO films were 30nm and 150 ± 20nm, respectively	151
Figure 5.1.3.3 (a) <i>J-V</i> curves of perovskite solar cells based on dense NiO _x films with different deposition time (thickness). (b) The transmittance spectra of NiO _x films as a function of deposition time	152
Figure 5.1.3.4 (a) Dark currents and (b) the recombination lifetime of the devices based on thin, nanostructured and disordered NiO layers. The thin, nanostructured and disordered NiO films were prepared at oxygen partial pressures of 10, 200 and 900 mT, respectively	

.....	153
Figure 5.1.3.5 Effect of the morphology and growth of the PLD-NiO films as a hole transporting layer, on the solar cell performance. Schematic images of thin, nanostructured and disordered NiO films fabricated using PLD as an electron blocking layer/hole extraction layer in the NiO/MAPbI ₃ /PCBM heterojunction solar cells.....	154
Figure 5.1.3.6 XRD patterns and plane-view FESEM images of MAPbI ₃ layers coated on the NiO films synthesized at 10, 200 and 900 mT, respectively.....	155
Figure 5.1.3.7 (a) Cross-sectional FESEM images of PLD-NiO films deposited at the oxygen partial pressures of 200 mT with the thickness of 100, 180, 250, 340 nm. (b) <i>J</i> - <i>V</i> characteristics of PLD-NiO based perovskite solar cells with different NiO layer thickness, measured under simulated AM 1.5 100 mW·cm ⁻² sunlight. (c) The transmittance spectra of PLD-NiO films and (d) the normalized external quantum efficiency (EQE) spectra of prepared solar cells as a function of film thickness.....	156
Figure 5.1.3.8 (a) <i>J</i> - <i>V</i> curves and (b) EQE spectra for the best cell using nanostructured NiO film with a thickness of 150 nm. The photovoltaic parameters of the best cell are shown in the inset table.....	157
Figure 5.1.3.9 Steady-state current density measured at a maximum power point (0.906V) of the champion cell and its stabilized power	

output..... 158

Figure 5.1.3.10 *J-V* curves of 200 mT-NiO based device under reverse (from V_{oc} to J_{sc}) and forward (from J_{sc} to V_{oc}) scan directions. The scan speed was 0.25 V/s 159

Chapter 1. Introduction

1.1 Overview: Semiconducting Oxide Materials in Photoelectric Energy Conversion System

The availability of energy source is vital for social and economic development of human race. Today, as a result of the generalization of agricultural, industrial and domestic activities the demand for energy has increased remarkably. [1.1] According to the previous reports, world's population will reach 8.3 billion by 2030, which means an additional 1.3 billion people, and the world's income in 2030 is expected to be roughly double the 2011 level. Population and income growth are the key factors behind growing demand for energy. As a result, world energy consumption is projected to grow by 1.6% every year from 2011 to 2030, adding 36% to global consumption by 2030. [1.2] Such ever-increasing demand could provoke the crisis on the energy shortage by resource depletion and the environmental problems such as greenhouse gas emissions and global warming. Achieving solutions for such energy crisis requires long-term exertion for development of sustainable energy. In this point of view, renewable energy resources appear to be the one of the most efficient and effective solutions to overcome the energy crisis.

Among the renewable energy resources, solar energy is one of the most abundant and sustainable source which available in both direct, *i.e.* solar cooking, heating, drying, and conversion to electricity and indirect forms, *i.e.* biomass, wind, and water. The amount of solar energy that reaches the earth a minute is nearly equivalent to the amount of world energy demand a year. Thus, using the solar power as an alternative energy could be a pertinent solution for both energy shortage and environmental problems.

Photovoltaic (PV) device as photoelectric energy conversion system using solar energy has been of great interests to scientists and researchers all over the world and has been a challenging object for the last several decades. Over the last three decades, various types of solar cells have been investigated and developed. As a result, the highest energy conversion efficiency over 40 % was achieved, as shown in Figure 1.1.1. [1.3] At present, silicon based solar cells dominate the 90 % of the global photovoltaic market. Recent reductions in the manufacturing costs of silicon based solar cell technology assure the future large-scale use of photovoltaic devices, which is expected to contribute nearly 30 % of new electricity generation capacity worldwide between 2013 and 2030. [1.4] However, despite of the reduction of manufacturing cost, the silicon based solar cells is still not free from the cost problem and the opportunities for achieving both high energy conversion efficiency and low processing cost still remain.

Dye or inorganic semiconductor sensitized solar cells (D(I)SSCs), organic photovoltaic (OPV) cells and organic-inorganic hybrid perovskite solar cells

(PSCs) have found acceptance as the emerging PVs due to their relatively low manufacturing cost, environmental friendly and strong solar absorption for the possibility to reach high energy conversion efficiency. However, the emerging PVs still suffer from their relatively low cell performances under ~15 % of efficiency. Recently for the last 5 years, PSCs have strongly attracted the attention in PV community due to their superb efficiency and have reached the highest energy conversion efficiency among the emerging PVs, over 20 %, but their efficiency and environmental stability is still inferior to the conventional type solar cells.

N-type and p-type semiconducting oxides such as titanium dioxide (TiO_2) and nickel oxide (NiO) with wide band gap (> 3.0 eV) to transmit light are one of the key materials to generate high electric power from sun light in emerging PVs as a charge (electron and hole) accepting and transporting phase. [1.5 - 1.9] Because their charge accepting and transporting ability determines charge collecting property and overall efficiency of solar cells, controlling their electrical and optical properties such as electron density, mobility, conduction band edge position and band gap as well as their configuration such as in a form of meso-porous, nanowire, nanotube, and nanostructure are the key technique to achieve high performance emerging PVs. [1.9] This thesis mainly focuses on the property control of semiconducting oxides in terms of structural and compositional design for improving charge collecting ability, in a broad sense including charge injection, extraction and transportation, in the emerging PVs, particularly in ISSCs and PSCs. Controlling the charge collecting ability through the

structural and compositional design is strongly expected to enhance the device performance of ISSCs and PSCs and consequently offers breakthrough to overcome their faced limits.

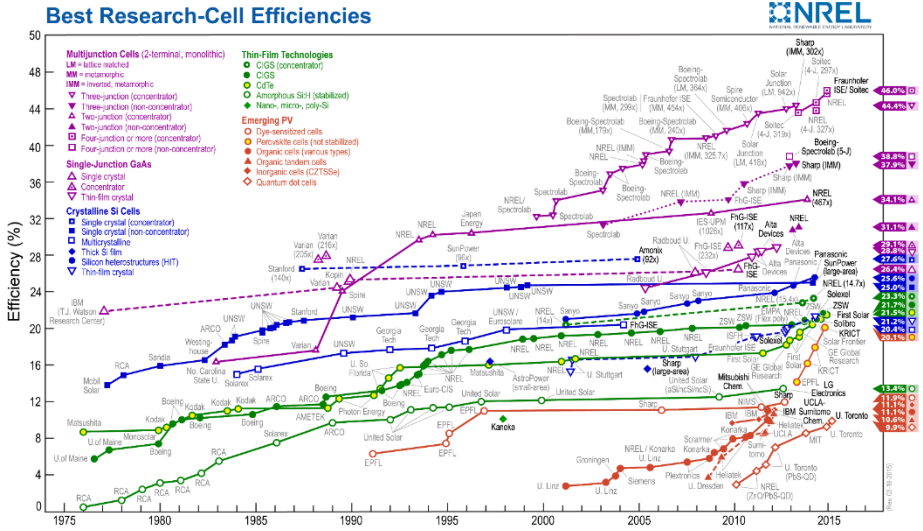


Figure 1.1.1 The latest chart on record solar cell efficiencies (2015). [1.3]

1.2 Aim and Strategies

Since the semiconducting oxides have great influence on determining the overall efficiency of the photoelectric energy conversion system, their intrinsic and extrinsic design can lead to enhancement in the photovoltaic performances of the emerging PVs such as ISSCs and PSCs. Particularly, controlling the charge collecting property through the semiconducting oxide photoelectrodes is one of the most important factor to achieve highly efficient ISSCs and PSCs. The aim of this thesis is to synthesize semiconducting oxide photoelectrodes having highly efficient charge collecting property through their structural and compositional design, and to propose a guideline of designing the desirable photoelectrode for highly efficient solar cells.

This thesis proposes two strategies for efficient charge collecting property in ISSCs and PSCs. First is the structural design of semiconducting oxide based photoelectrodes for suppression of recombination and efficient charge collection. Since the morphology of the photoelectrode strongly affects the charge extraction/transportation and lifetime, controlling the morphology is required. Second is the compositional design for effective charge injection from light absorbers to electron acceptors, which enhances the photovoltaic performances.

In chapter 2, basic theoretical concept of the emerging PVs and the fundamental understandings about their operating principles are described.

Moreover, synthesis of nanostructured materials using pulsed laser deposition (PLD) system is represented and reviewed. Finally, the semiconducting oxides used in this thesis are introduced.

In chapter 3, experimental procedures about synthesis of semiconducting oxide photoelectrodes and light absorbing materials, fabrication of the solar cells and their characteristic analysis methods used in this thesis are described.

In chapter 4, structural design for n-type TiO_2 semiconducting oxides is explored as photoelectrodes in ISSCs. The TiO_2 photoelectrodes containing various forms are synthesized on glass substrates by PLD system and the device performances of ISSCs are characterized in terms of light harvesting and charge collecting property. The correlation between the electrode structure and the charge collecting property are investigated. Furthermore, compositional design of n-type TiO_2 photoelectrodes is examined to enhance the charge injection ability in ISSCs. Finely controlled niobium (Nb) doped TiO_2 photoelectrodes are synthesized by PLD. From the basis that the energy difference between the conduction band (CB) of inorganic semiconductor (IS) and TiO_2 serves as the driving force for electron injection [1.10 – 1.11] and that the doping metal cation such as niobium (Nb) and tungsten (W) into TiO_2 lattice alters the CB position of TiO_2 , [1.12 – 1.13] the enhanced charge injection and collection of TiO_2 is expected by Nb doping. The relationship between the Nb doping and the band engineering of TiO_2 , and the following results on the charge injection ability and the final device performance are investigated.

In chapter 5, structural design of p-type nickel oxide (NiO) as hole transporting layers (HTL) in PSCs is investigated. Highly transparent nanostructured NiO films containing various density and porosity are grown on glass substrates by PLD. Compared to the densely-packed thin or porous NiO film applied-PSCs, the nanostructured NiO film applied-PSCs perform improved charge extraction and transportation. The correlation between the NiO structure and the charge collecting property in the device performances is investigated.

1.3 Bibliography

- [1.1] R. Baños, F. Manzano-Agugliaro, F.G. Montoya, C. Gil, A. Alcayde, J. Gómez, *Renew. Ener. Sust. Energ. Rev.* **2011**, 15, 1753.
- [1.2] BP Energy Outlook 2030, BP Global, <http://www.bp.com>
- [1.3] Research Cell Efficiency Records: latest chart, National Renewable Energy Laboratory (NREL), <http://www.nrel.gov/ncpv>
- [1.4] G. Turner, Global Renewable Energy Market Outlook 2013, Bloomberg New Energy Finance, <https://www.bnef.com/insightdownload/7526/pdf>, **2014**.
- [1.5] B. O'Regan and M. Grätzel, *Nature* **1991**, 353, 737.
- [1.6] M. White, D. Olson, S. Shaheen, N. Kopidakis and D. Ginley, *Appl. Phys. Lett.* **2006**, 89, 143517
- [1.7] J. H. Heo, S. H. Im, J. H. Noh, T. Mandal, C. Lim, J. A. Chang, Y. H. Lee, H. J. Kim, A. Sarkar, M. Nazeeruddin, M. Grätzel and S. I. Seok, *Nature Photonics* **2013**, 7, 486.
- [1.8] M. D. Irwin, D. B. Buchholz, A. W. Hains, R. P. H. Chang and T. J. Marks, *PNAS* **2008**, 105, 2783.
- [1.9] K. Wojciechowski, M. Saliba, T. Leijtens, A. Abate and H. Snaith, *Energy Environ. Sci.*, **2014**, 7, 1142.
- [1.10] A. Braga, S. Giménez, I. Concina, A. Vomiero and I. Mora-Seró, *J. Phys. Chem. Lett.* **2011**, 2, 454.

- [1.11] D. Wang, H. Zhao, N. Wu, M. Khakani and D. Ma, *J. Phys. Chem. Lett.* **2010**, 1, 1030.
- [1.12] X. Lü, X. Mou, J. Wu, D. Zhang, L. Zhang, F. Huang, F. Xu and S. Huang, *Adv. Funct. Mater.* **2010**, 20, 509.
- [1.13] X. Zhang, F. Liu, Q. Huang, G. Zhou and Z. Wang, *J. Phys. Chem. C* **2011**, 115, 12665.

Chapter 2. Background and Literature Review

2.1 Emerging Photovoltaics (PVs)

2.1.1 History of Solar Cells

Solar cell, in other words photovoltaic (PV) cell, is an electrical device that converts the energy of sunlight directly into electricity. The first PV effect was demonstrated by Edmond Becquerel in 1839. In 1883, Charles Fritts designed the first PV cell by coating the selenium inorganic semiconductor with a thin layer of gold, achieving a device efficiency of 1%. [2.1] Silicon based solar cells, which known as the first generation solar cell, was invented by Russell Ohl and in 1954, a silicon solar cell performing 6% of energy conversion efficiency with direct sunlight was fabricated. [2.2] Since then, solar cells have made remarkable process by research groups all over the world. The PV cells are commonly classified as first, second and third generation solar cells in terms of their manufacturing cost and efficiency; high cost/high efficiency (first generation, 1G), low cost/low efficiency (second generation, 2G) and low cost/high efficiency (third generation, 3G). [2.3] The first generation PV technology is known to be silicon based solar cells, which

not only leads to high efficiency (over 25% of efficiency [2.4]), but also high manufacturing cost due to their high purity requirements and fabrication temperature. The 2G was developed with the aim of reducing the high costs of 1G solar cells by reduction of the device thickness, using amorphous or polycrystalline silicon, Copper indium gallium selenide (CIGS) and cadmium telluride (CdTe). However, the thermodynamic limit of the light to electric energy conversion efficiency of single-junction PV cell (1G and 2G solar cells), optimized to the AM 1.5 G spectrum, is 32.9 %. [2.5] This Shockley–Queisser limit [2.6] originates from the fact that photons with energies below the band-gap energy are not absorbed, while photons with energies above the band-gap energy release the additional energy mostly as heat. This limit induced the development of 3G solar cells with advanced PV concepts such as multi-junction cells, optical up and down converters, multiple carrier generation by impact ionization, and impurity band cells including quantum dots based on III–V materials or novel device concepts such as semiconductor sensitized (mesoscopic) solar cells. Despite the development of 3G solar cells, still more improvements in device performances are required to be competitive with the previous generation solar cells in terms of cost per watt. Therefore, the 4G of PV technology based on cost-efficient organic, inorganic and organic-inorganic hybrid materials was introduced. These device architectures compose both organic and inorganic components to not only maintain the inexpensive nature but also improve the energy harvesting, charge dissociation, and charge transport of solar cells. [2.7]

2.1.2 Operating Principles of the Emerging PVs

The operation of a PV device requires 3 basic attributes: (1) the absorption of light and generating electron-hole pairs or excitons by light absorbers, (2) the separation of generated charge carriers of opposite types, and (3) the extraction of the separated carriers to an external circuit. The conventional PV device uses a donor and an acceptor type of materials, which form a heterojunction favoring the separation of the exciton into two carriers. Those formed carriers are then transported to the electrodes by the same materials that are used for the generation of an exciton. Hence, the exciton generating material for classical PV devices should have both efficient light harvesting and charge transporting properties, which is difficult to achieve. The emerging PVs, particularly dye or inorganic semiconductor sensitized solar cells (D(I)SSCs) and organic-inorganic hybrid perovskite solar cells (PSCs) which used in this thesis, separates the two requirements, which is the charge generation and charge transportation. The charge generation is done at the charge collecting material-light absorber interface and the charge transportation is done by the charge collecting materials, including electron/hole transporting materials (ETM/HTM) and the liquid electrolyte.

Based on this principle, ISSC and PSC are composed of 3 main components: (1) light absorbing materials which absorb light and generate the electron-hole pair, (2) electron transporting materials (ETM) and (3) hole transporting materials (HTM) which accept the generated electrons or holes

and transport them to the each side of the electrodes. Basic operating principles of solar cells are described in Figure 2.1.1. The first step is the absorption of light and excitation of electrons from the highest occupied molecular orbital (HOMO) to the lowest unoccupied molecular orbital (LUMO). The following step is the injection of excited electrons into the conduction band (CB) of ETM. After the injection, the injected electrons transport through the ETM network to arrive at the back contact and travel through the external circuit to the counter electrode to reduce the oxidant in HTM. A metal counter electrode such as gold, silver, aluminum or platinum catalyzes the electrochemical reduction. This completes the circuit.

Under illumination, an ideal device constitutes a regenerative and stable energy conversion system. However, some undesirable reactions occur resulting in the deterioration of device performance. One of the most undesirable reactions are the recombination of the injected electrons either with oxidized light absorber or with the oxidized HTM at the interface. For instance, the open circuit voltage (V_{oc}), which is the potential at which no current flow through the device, is determined by the energy difference between the Fermi level of ETM under illumination and the electrochemical potential of the HTM (the Nernst potential of the redox couple in the liquid electrolyte or the work function of hole transporting oxide semiconductors). However, the experimentally observed V_{oc} is smaller than the theoretical value. This is generally known as the competition between electron transfer and charge recombination pathways. [2.8] Furthermore, the fill factor (FF) is the ratio of the maximum power obtained with the device and the theoretical

maximum power, which represented in equation (2.1.1). [2.9]

$$FF = \frac{P_{max}}{P_{th}} = \frac{J_{mp}V_{mp}}{J_{sc}V_{oc}} - (2.1.1)$$

P_{max} is the obtained maximum power, P_{th} is the theoretical maximum power, J_{mp} is the current obtained at maximum power, V_{mp} is the voltage obtained at maximum power, J_{sc} is the short circuit current, and V_{oc} is the open circuit voltage. The FF reflects electrical and electrochemical losses occurring during operation of the solar cells, which also strongly influenced by the charge recombination. [2.10] Since the overall energy conversion efficiency (η) of the solar cell is determined by J_{sc} , V_{oc} , FF, and the intensity of the incident light (I_s) as described in equation (2.1.2), it is important to control and suppress the charge recombination during the operation in order to achieve high V_{oc} , FF, and the overall energy conversion efficiency.

$$\eta = \frac{J_{sc}V_{oc}FF}{I_s} - (2.1.2)$$

2.1.3 Inorganic Semiconductor Sensitized Solar Cells

Inorganic semiconductor sensitized solar cells (ISSCs), also known as quantum dot sensitized solar cells (QDSCs), have been developed by replacing conventional organic based sensitizers to inorganic semiconductor light absorbing materials. Over the last decades, the ISSCs extensively have attracted enormous attention due to their outstanding opto-electronic properties such as tunable energy band gaps via varied and controlled size and shape of the nanocrystals, [2.11 - 14] large optical absorption coefficients, large dipole moments for enhanced charge separation, and multiple exciton generation (MEG). [2.15 – 18] Numerous architectures for ISSCs were proposed including sensitized type solar cells [2.14, 2.18, 2.19], layered type solar cells [2.20 – 23] and multi-junction tandem solar cells. [2.24] Among all, the sensitized type solar cells was focused in this section, which the type mainly studied and investigated in this thesis.

Device Configuration of ISSCs

The device configuration of a typical ISSC is illustrated in Figure 2.1.2. A wide-bandgap semiconducting oxide such as titanium dioxide (TiO_2) or zinc oxide (ZnO) photoelectrode is synthesized on a transparent conducting oxide (TCO) substrate, usually tin doped indium oxide ($\text{Sn}:\text{In}_2\text{O}_3$, ITO) or fluorine doped tin oxide ($\text{F}:\text{SnO}_2$, FTO). Large microscopic surface area of the

photoelectrode is sensitized with thin layer of IS such as cadmium chalcogenides (CdS, CdSe) or lead chalcogenides (PbS, PbSe), while a redox liquid electrolyte fills the free space around the IS sensitized photoelectrode. The IS absorb light and inject electrons from their excited levels into the conduction band (CB) of the photoelectrode, while oxidized IS are recharged by the S^{2-}/S_n^{2-} polysulfide redox couple. Charge transportation to the front electrode (TCO) as well as transport of oxidized redox species to the counter electrode (CE) is diffusion-driven. [2.25 - 27]

Light Absorbing Materials in ISSCs

Inorganic semiconductors (IS) (or quantum dots) such as CdS, CdSe, CdTe, PbS, PbSe, Sb₂S₃, Sb₂Se₃, Bi₂S₃ and etc. have been used as the alternative light absorbers in solar cells due to their relatively small band gap, which is appropriate for light absorption. (Figure 2.1.3 [2.28]) Among the IS, cadmium and lead chalcogenide IS have been intensively studied over the past decades as the light absorbers. [2.15, 2.18, 2.29 – 37] CdS has an optical band gap of 2.25 eV, which can only absorb light up to ~550 nm. CdSe, with a band gap of 1.7 eV, can absorb light below ~720 nm. The CB edges of CdSe nanocrystals were located below the CB edge of TiO₂ film, which resulted in poor and limited electron injection from CdSe to the TiO₂, and substantial charge recombination occurred at the TiO₂/CdSe/electrolyte interfaces. To solve the above problem, co-sensitization of CdS/CdSe QDs on a TiO₂ film was proposed. [2.38, 2.39] The co-sensitization of CdS/CdSe system showed

improved device performance over individual CdS or CdSe systems and the rate of electron injection from CdSe to TiO₂ was significantly improved by the CdS interlayer. PbS-based solar cells have been intensively examined in recent years because of the small band gaps of the PbS, which allow solar energy harvesting in the near-infrared region. PbS have an energy band gap in the range of 0.9–1.1 eV, so the optical absorption edge can be extended to 1300nm. However, under light illumination, the shunt resistance of the ISSCs was smaller than in the dark; the rates of charge recombination increased at the interfaces of PbS - PbS and TiO₂ – PbS because of the increased surface states and trap states. In order to solve the interface problem, surface coating of PbS with CdCl₂ and CdS were proposed. [2.15, 2.40] The CdCl₂ and CdS passivation layer play a major role in the passivation of the mid-gap trap states and charge transport in the valence band. Larger photocurrent and voltage are achieved through decreased recombination and improved charge transport in the PbS based ISSCs.

Semiconducting Oxides in ISSCs

In ISSC system, semiconducting oxides have a critical importance, since they are one of the main constituents, the photoelectrode, in the photoelectrochemical system. Semiconducting oxide materials such as TiO₂ and ZnO are commonly used as the electron accepting and transporting materials, which is the anode, in ISSC. There are 3 major requirements for the semiconducting oxides to be used as the photoelectrode:

- (1) Appropriate energy band alignment with the light absorbers for efficient charge separation and injection.
- (2) Large surface areas that can allow anchoring a large amount of IS and offer a large interface area to separate the photogenerated charge.
- (3) Efficient charge extraction and transportation ability to suppress the charge recombination, which usually occur at the interface of semiconducting oxide/IS or semiconducting oxides/IS/electrolyte.

The CB of semiconducting oxide should be located at lower position than that of IS light absorbers for which the charge separation of generated electron-hole pair and charge injection from the CB of IS to the CB of semiconducting oxide are favored. To retain the large surface area, a mesoporous structure is typically used for the semiconducting oxide photoelectrode. The mesoporous structure typically consists of crystals with a diameter of tens of nanometers which are sintered together to form a continuous network. Their small size induces the large surface area of the film, which results in the large amount of IS sensitization. However, in terms of charge extraction and transportation, nanoparticles networking electrode is not satisfied enough because the electrons should travel millions of boundaries to reach the TCO layer. These boundaries slow down the electron transport and increase the possibility of electron recombination. To find the solution for the above problems, novel architectures of semiconducting oxide photoelectrode, such as nanorods, nanowires and nanotubes, were proposed. Nanorods and nanowires are usually known to have high electron mobility due to their single-crystalline

nature. [2.41, 2.42] Also, highly ordered nanotube structures have been produced and used as photoelectrodes for solar cells. [2.43] However, their relatively small surface area compared to that of mesoporous structures cause the reduction of IS absorption, resulted in the decrease of generated photocurrent density. Thus, the architecture that satisfies both large surface area and efficient charge extraction and transportation is needed.

2.1.4 Perovskite Solar Cells

Question about the realization of stable and efficient solar cells for commercialization using the liquid electrolyte as HTM, the development of solid-state solar cells has arisen. In 2009, MAPbI₃ based solar cell was first introduced and the perovskite material having larger bandgap by replacing iodine into bromine for liquid electrolyte type solar cell was introduced. [2.44] However, the device efficiency was only 3.8%, which was much lower than a conventional solar cell. By changing both the electrolyte formulation and the method of depositing the perovskite, the device performance reached the energy conversion efficiency of 6.5%. [2.45] MAPbI₃ is a superior light harvester compared with the more commonly used dye or other IS showing the molar extinction coefficient of about $1.5 \times 10^5 \text{ (molL}^{-1}\text{)}^{-1} \text{ cm}^{-1}$ at 550 nm, which is 2 ~ 3 times higher than the organic dyes. This means that a thinner absorbing layer would be sufficient to obtain good photovoltaic performances.

Another key advance was subsequently made by replacing the liquid electrolyte with a solid-state HTM. [2.46] Both device performance and stability were significantly improved by avoiding the liquid electrolyte and introducing the solid type HTM with much thinner photoelectrode thickness ($> 1 \mu\text{m}$) compared to the liquid type solar cell. Since then, the photovoltaic performances using the perovskite light absorbers have been dramatically increased, achieving up to approximately 20 % today. [2.47]

Metal Halide Perovskite Light Absorbing Materials in PSCs

Methyl-ammonium lead iodide ($\text{CH}_3\text{NH}_3\text{PbI}_3$, MAPbI_3) perovskite light absorbing material has been actively investigated during the past two decades due to their interesting optical and electronic properties. [2.48 – 2.55] The band energy levels of various metal halide based light absorbers are represented in Figure 2.1.4. [2.28] MAPbI_3 has a direct bandgap of 1.55 eV, which corresponds to an absorption onset of 800 nm [2.56], which makes this material a good light absorber over the whole visible solar emission spectrum. Ideally, perovskite can be represented by the simple building block ABX_3 , where A is the organic cation, B is the inorganic metal cation and X is the halide anion. A is positioned at the center of a cubic, where BX_6 formula is positioned at the corners of the cubic. At the corner, they form a BX_6 octahedral arrangement where B occupies the center of an octahedra surrounded by X which located at the corners. Figure 2.1.5 illustrates the crystal structure of metal halide perovskite materials. [2.48] One of the

amazing advantages of the perovskite light absorber is that the electrical and optical properties can be converted by simply modifying the halide anions. The electron and hole diffusion length were estimated to be approximately 129 and 105 nm for the conventional MAPbI₃, respectively, and they dramatically increased to ~1069 and ~1213 nm by simple introduction of mixed halide of iodine and chlorine. [2.57] On the other hand, their optical property significantly changes with the introduction of bromine. The band gap engineering by the chemical management of MAPb(I_{1-x}Br_x)₃ perovskites indicates that the perovskites can be controllably tuned to cover almost the entire visible spectrum, enabling the realization of colorful solar cells. [2.52]

Device Configuration of PSCs

The PSCs were derived from the conventional DSSCs or ISSCs, so the device configurations are similar to each other. However, the PSCs are able to operate in two different architectures depending on the role of the perovskite material in the device, a mesoscopic type and a planar type. First the mesoscopic type, where the perovskite functions mainly as a light absorber, and charge transport occurs in semiconducting oxide layer. Second the planar type, where most electron or hole transport occurs in the bulk of the perovskite itself. For the mesoscopic type or the bi-layered type, [2.53] similar to the DSSCs, the perovskite materials are coated onto a charge collecting photoelectrode, which TiO₂ is most commonly used, as light-absorber. The photogenerated electrons at the perovskite materials are transferred from the

perovskite light absorber to the TiO₂ mesoporous layer through which they are transported to the electrode and extracted into the circuit. The planar type architecture is based on the finding of highly efficient, ambipolar conducting property of the perovskite materials. [2.57] After light absorption and the charge generation of the perovskite, both negative and positive charge carriers are transported through the perovskite to charge collecting layers. As mentioned above, the PSCs were emerged from the DSSCs, so the architecture containing TiO₂ mesoporous structure was initially used. But the planar type has become another issue in the field of PSCs with the possibility that the thin film architecture can simplify the device fabrication process and reduce the manufacturing cost. The schematic illustrations for the two different type of PSC architectures are represented in Figure 2.1.6.

Device Structure of PSCs

Besides the classification based on the electrode structure which described in the previous section, the PSCs can be categorized into two types based on the device structure, n-i-p structure (n-type-intrinsic-p-type semiconductor) and p-i-n structure (p-type-intrinsic-n-type semiconductor). The device that contains mesoporous or planar TiO₂ layer and solid-type HTM is the n-i-p PSC. Although the devices based on n-i-p heterojunction exhibit good performance, the diffusion length of the hole is slightly shorter than that of the electron due to a larger effective mass of the hole. [2.57, 2.58] Therefore, PSCs based on p-i-n heterojunction, in which the substrate starts with the

HTM, are recently studied. [2.59 – 61] The perovskite light absorbing films are deposited on the HTM layer. With the illumination from the p-side, the device could feasibly have more efficient hole extraction and transportation. Another advantage for the p-i-n structure is the possibility of the integration of PSCs with other type of solar cells such as silicon or CIGS solar cells to build tandem devices. The device structures based on n-i-p and p-i-n structure are represented in Figure 2.1.7.

Semiconducting Oxides in PSCs

Semiconducting oxides are also important in PSCs because they serve as the charge extraction and transporting materials as in DSSCs and ISSCs. TiO_2 semiconducting oxide is most commonly used as the ETM layer, which is the anode, and NiO is used as the HTM, which is cathode in PSC. However the requirements of semiconducting oxide in PSC are quite different from the requirements in DSSCs and ISSCs, because of the low thickness of the PSCs (usually below 500nm for each layer: TCO, ETM, perovskite, HTM, metal electrode). In some PSCs, the devices even operate well without the mesoporous ETM layer. For example, PSC with the replacement of the mesoporous TiO_2 ETM layer by an insulating Al_2O_3 scaffold achieved efficient device performances. [2.46] Since the CB of Al_2O_3 is far higher than the LUMO level of the perovskite, no electron injection from the perovskite to Al_2O_3 . This indicates that the charge transport occurs only within the perovskite layer, which is similar to planar type PSC. However, it is

noteworthy that regardless of the mesoporous layer, a compact thin ETM layer is still required for both the collection of the generated electrons and hole blocking.

The 3 major requirements for the semiconducting oxides to be used as the photoelectrode in PSC:

- (1) Appropriate energy band alignment with the light absorbers for efficient charge separation and injection.
- (2) Efficient charge extraction and transportation ability to suppress the charge recombination.
- (3) Efficient electron blocking (for HTM) and hole blocking (for ETM) ability for the suppression of back electron-hole recombination.

Large surface area that can allow a large amount of light absorbers is not that necessary due to the layered type structure and low thickness of the PSC. Also, although the charge transport property is still very important in the PSC, due to the low thickness in nano-meter scale of the device, the novel architectures of semiconducting oxide photoelectrode such as nanorods, nanowires and nanotubes are not effective compared to the DSSCs. Instead, appropriate energy band alignment and electron/hole blocking properties of ETM and HTM have become very important for efficient device performance.

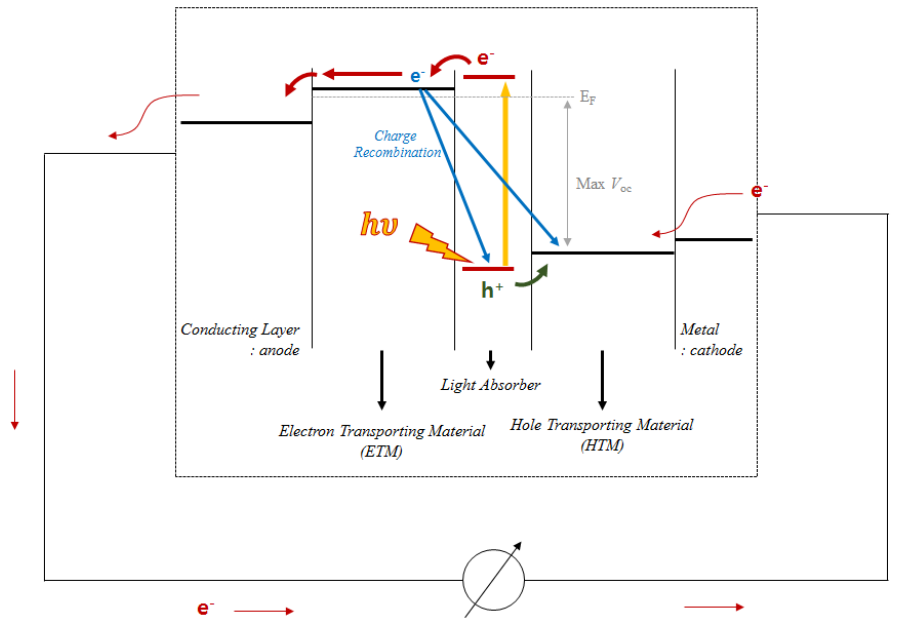


Figure 2.1.1 Schematic illustration of operating principles of a solar cell.

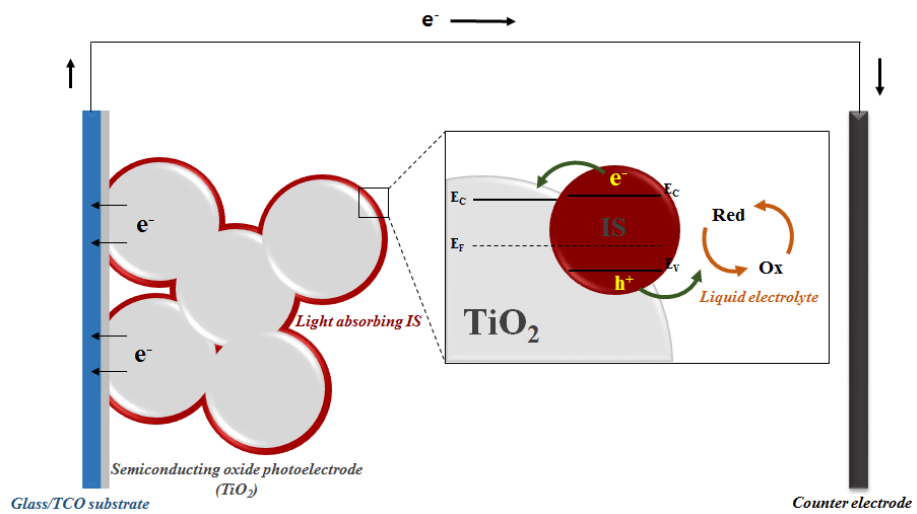


Figure 2.1.2 Device configuration of a typical ISSC.

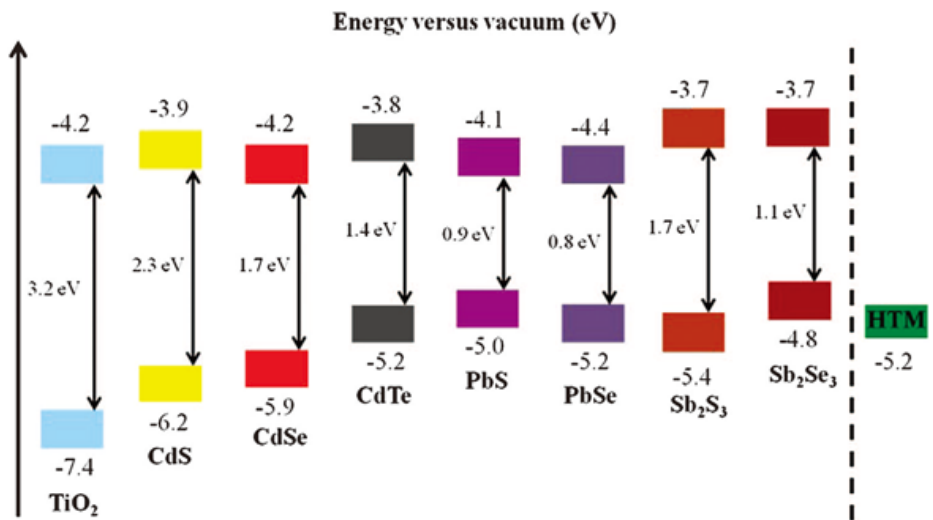


Figure 2.1.3 Band energy levels of various inorganic semiconductor based light absorbers used in ISSCs. [2.28]

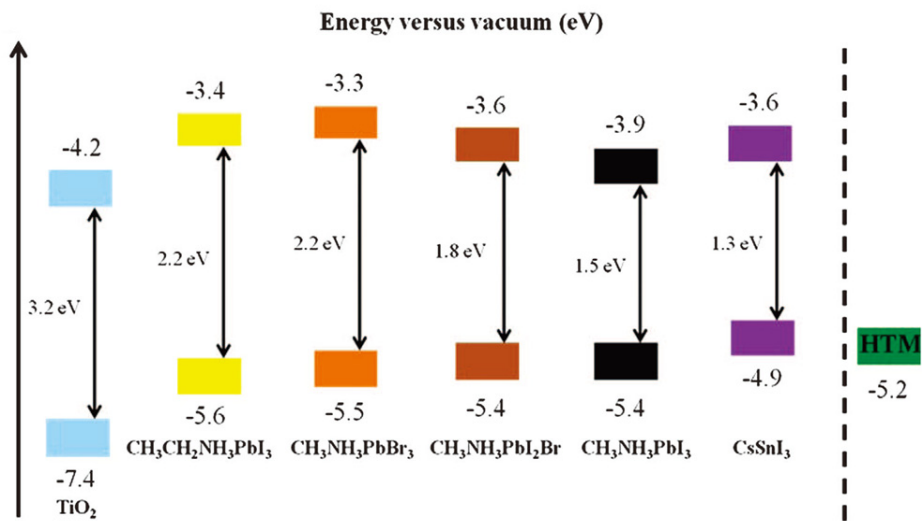


Figure 2.1.4 Band energy levels of various metal halide based light absorbers used in PSCs. [2.28]

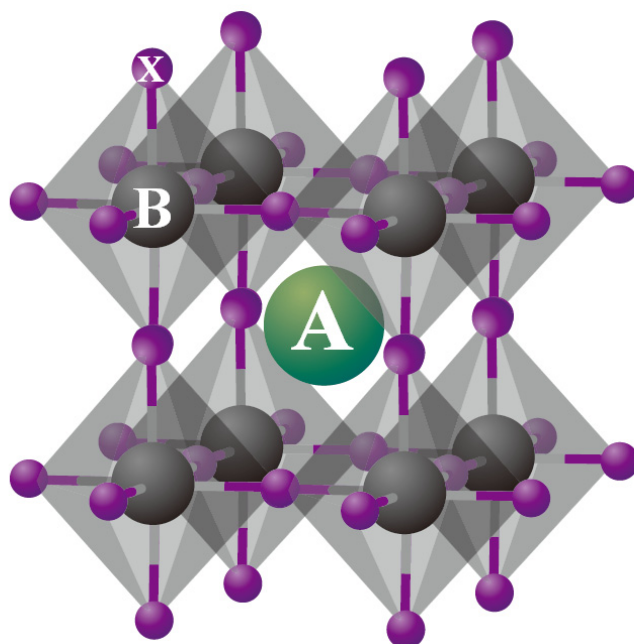
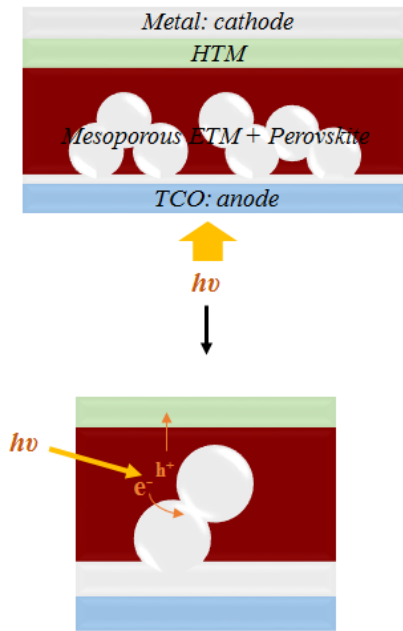


Figure 2.1.5 Crystal structure of cubic metal halide perovskites with the chemical formula ABX₃. Organic cations occupy position A and inorganic metal cations occupy position B whereas halide anions occupy X position. [2.48]

1. Mesoscopic PSCs



2. Planar PSCs

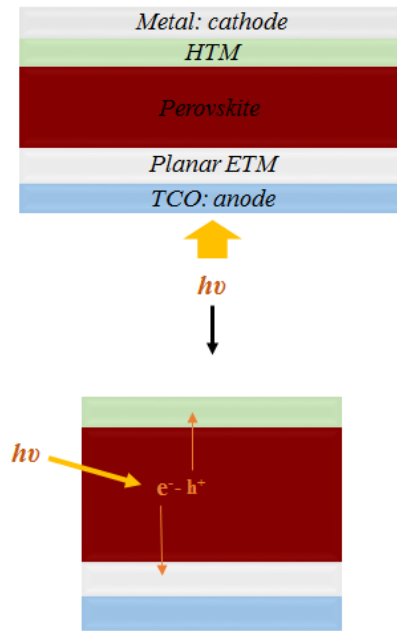


Figure 2.1.6 Schematic illustration for the two different types of PSC which classified by the photoelectrode structure.

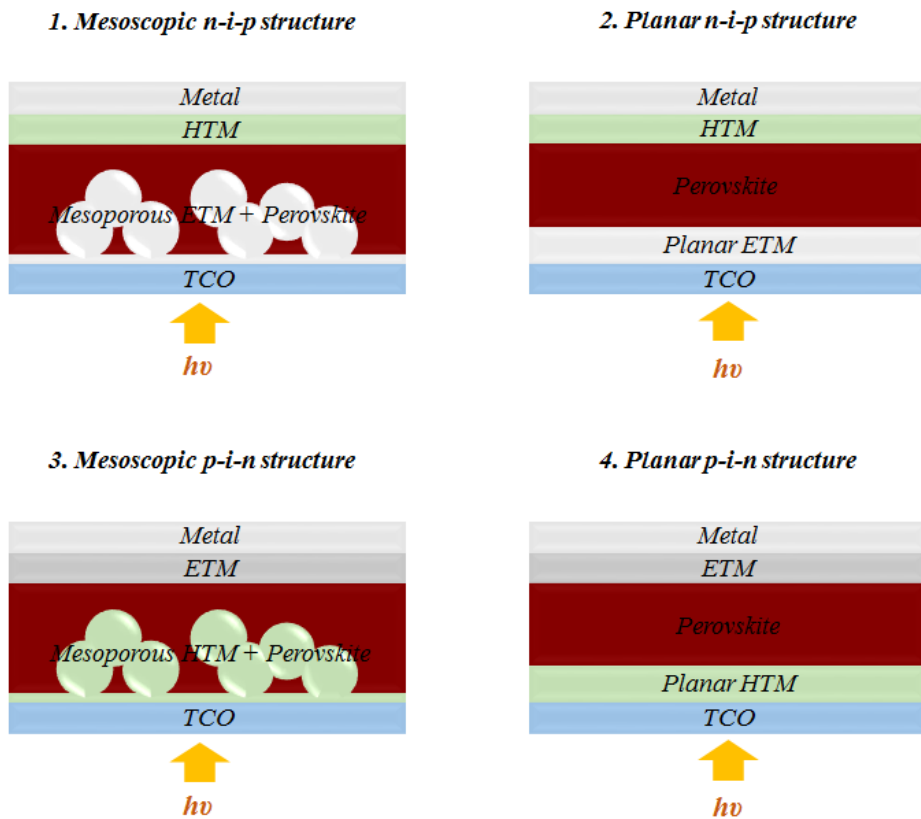


Figure 2.1.7 The PSC device structures based on n-i-p and p-i-n structure.

2.2 Nanostructured Materials by Pulsed Laser Deposition

2.2.1 Pulsed Laser Deposition

Pulsed laser deposition (PLD) has been developed as a powerful tool for fabrication in material processing, especially thin film. [2.62] The PLD technique was first used in 1965 for the preparation of semiconductors and dielectric thin films, [2.63] and was established due to the work of Dijkkamp and coworkers [2.64] on high-temperature superconductors in 1987. Figure 2.2.1 illustrates the general PLD system. In a high vacuum chamber, bulk target is fixed usually at an angle of 45° with the focused laser beam. The substrates are attached with the surface parallel to the target surface and the target-to-substrate distance is typically 2 ~ 10 cm. In order to obtain a steady ablation rate, the laser beam should be scanned over a sufficient target area (at least 0.1 cm^2). A pulsed laser beam is focused onto the surface of a solid target. The strong absorption of the electromagnetic radiation by the solid surface leads to rapid evaporation of the target materials. The evaporated materials which consist of highly excited and ionized species form a glowing plasma plume in front of the target surface when the ablation is carried out in vacuum.

There are many advantages and disadvantages for using the PLD technique. The advantages are listed as below: [2.65]

- (1) Straightforward deposition technique that only a few parameters, such as laser energy density, pulse repetition rate, background gas pressure are needed to be controlled during the process.
- (2) Relatively high deposition rate compared to other film growth techniques.
- (3) Due to high heating rate of ablated materials, much lower substrate temperature during process is demand compared to other film growth techniques.
- (4) Easy to produce multi-layered films of different materials by sequential ablation of assorted targets.
- (5) Stoichiometric transfer between the target and the deposited film. This is the result of the extremely high heating rate of the target surface (10^8 Ks^{-1}) due to pulsed laser irradiation. It leads to the congruent evaporation of the target irrespective of the evaporating point of the constituent elements or compounds of the target. Thus, PLD is the most suitable to fabricate for the materials with complex composition.

The shortcomings of PLD technique is listed below:

- (1) Splashing deposition on the films. The physical mechanisms lead to splashing of the ablated species, including the sub-surface boiling and expulsion of the liquid layer.

- (2) Deposition of film containing ununiformed particulates. The large size of particulates may greatly affect the growth of the subsequent layers as well as the electrical properties.
- (3) The narrow angular distribution of the ablated species, which is generated by the adiabatic expansion of laser, produced plasma plume and the pitting on the target surface. These features limit the usefulness of PLD in producing large-scale film.

2.2.2 Synthesis of Nanostructured Materials by PLD

The PLD is normally known as the thin film fabrication technique, but for the last two decades, there have been researches about synthesis of nanostructured semiconductor films using PLD, such as nanoclusters, nanowires/rods and porous nanostructures. First, synthesis of Si nanocluster film using PLD technique was reported by Movtchan *et al.* [2.66] Since then, a number of groups followed the research about Si-based nanocluster. [2.67 – 69] In 1998, Lieber *et al.* reported the synthesis of crystalline Si-Fe nanocomposite nanowires using PLD technique. [2.70] The fabrication mechanism of nanowires or nanorods using PLD technique is similar to that of vapor-liquid-solid (VLS) process. Various semiconducting oxides such as hematite (α - Fe₂O₃), [2.71] ZnO, [2.72, 2.73] MgO [2.74] and TiO₂ [2.74] based nanowires and nanorods were synthesized using the combination system of

PLD and VLS process. The synthesis of nanostructured films is based on the control of kinetic energy of the ablated species during process by modifying the deposition parameters. A simple formation mechanism of the nanostructured film by PLD was proposed in the previous report in our laboratory, as shown in Figure 2.2.2. [2.75] High energy laser ablates the target and forms a plasma plume which consists the ablated species based on the target material. Here, the formation of film is strongly influenced by the kinetic energy of ablated species and the thermal energy of substrate. If the thermal energy of the substrate is regulated, the formation of film only depends on the kinetic energy of the ablated species. The kinetic energy can be controlled with the deposition parameters such as laser energy density, target-to-substrate distance, and pressure of background gas. In terms of the background gas pressure, if the pressures are low, the ablated species can reach the substrate with high kinetic energy due to only a little disturbance of the background gas molecules, which resulted in the formation of a densely-packed film. If the background gas pressures are relatively high, the kinetic energy is reduced by the collision with the gas molecules before reaching the substrate, resulting in the formation of loosely-packed film. Thus, the remaining kinetic energy of the ablated species can determine the film morphology such as porosity and alignment. By controlling the experimental parameters during the PLD process, the morphology of nanostructured films can be controlled systematically. [2.75] Using this process, various semiconducting oxides were synthesized. [2.75 – 2.79] Additionally, the nanostructured semiconducting oxides synthesized by PLD were applied to

the photovoltaic devices as a photoelectrode. [2.75, 2.78, 2.79] The multi-complex nanostructured films by PLD will be in great interest for various emerging PV applications such as solar cells and photocatalysts, for direct hydrogen production and environmental remediation which need large surface area.

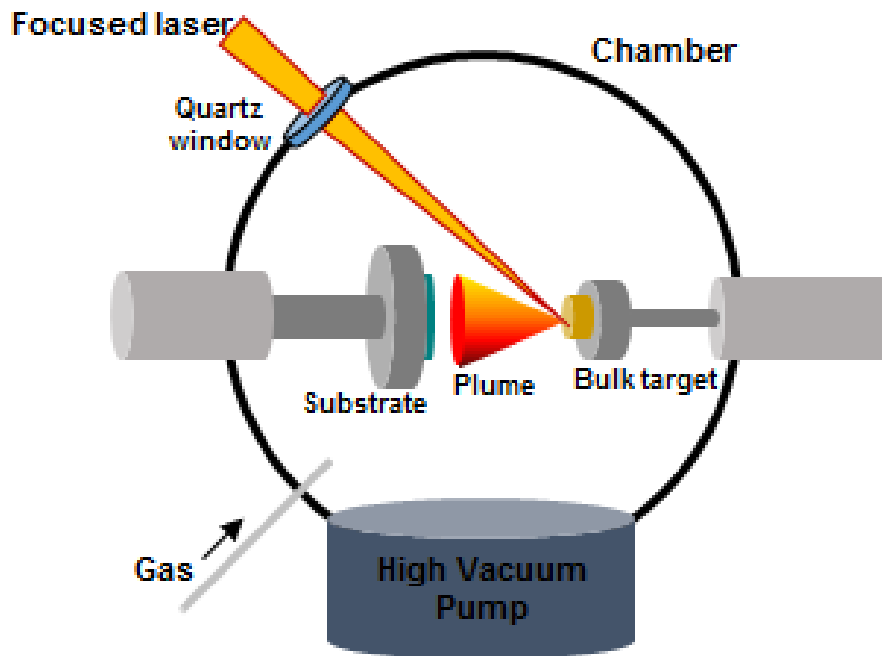


Figure 2.2.1 Schematic illustration of general PLD system.

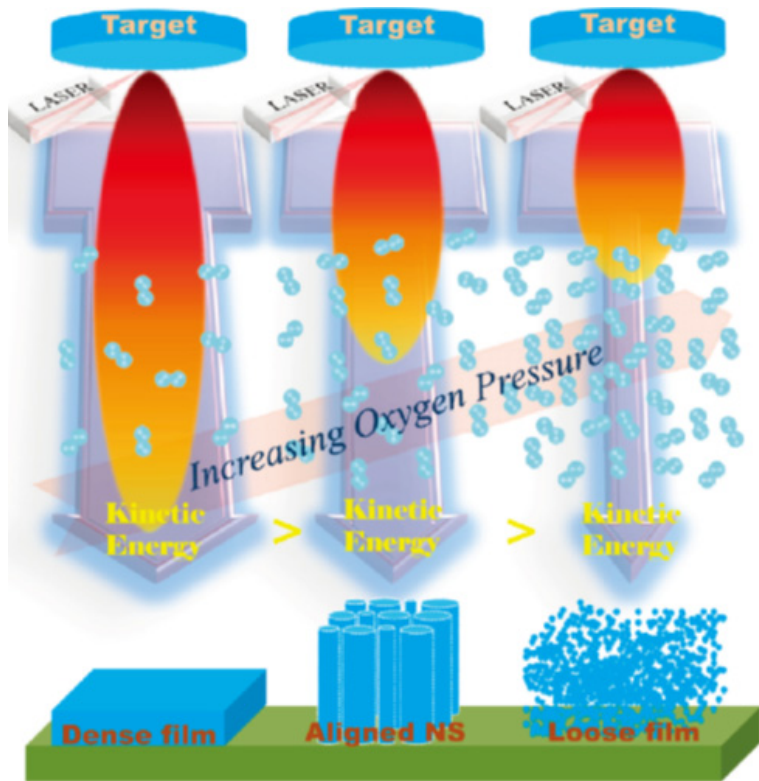


Figure 2.2.2 Synthesis of nanostructured film using PLD system. [2.75]

2.3 Materials

2.3.1 Titanium Dioxide (TiO₂)

Titanium dioxide, or also called as titania, is the naturally occurring oxide of titanium, with the chemical formula of TiO₂. TiO₂ belongs to the family of transition metal oxides. There are 3 commonly known polymorphs of TiO₂, anatase, brookite and rutile. Besides the 3 common polymorphs, there are 3 additional polymorphs, TiO₂ (B), [2.80] TiO₂ (II) with a PbO₂ structure [2.81] and TiO₂ (H) with a hollandite structure. [2.82] Rutile is the most abundant phase. The metastable anatase and brookite phases convert irreversibly to the equilibrium rutile phase upon heating above temperatures in the range 600 - 800 °C. TiO₂ is a large band semiconductor, with band gaps of 3.2, 3.02, and 2.96 eV for the anatase, rutile and brookite phases, respectively. The crystal structures for 3 main polymorphs are represented in Table 2.3.1. [2.83] Rutile TiO₂ has a tetragonal structure and contains 6 atoms per unit cell. The TiO₆ octahedron is slightly distorted. The rutile phase is stable at most temperatures and pressures up to 60 kbar, where TiO₂ (II) becomes the thermodynamically favorable phase. [2.84] The activity of the rutile phase as a photocatalyst is generally poor. [2.83] Brookite belongs to the orthorhombic crystal system. Its unit cell is composed of 8 formula units of TiO₂ and is formed by edge-sharing TiO₆ octahedra. Anatase also has a tetragonal structure but the

distortion of the TiO_6 octahedron is slightly larger for than the rutile phase. The anatase phase is preferred over other polymorphs for solar cell applications because of its relatively high electron mobility, low dielectric constant and low density. [2.80] The increased photoactivity of the anatase phase is due to the slightly higher Fermi level, lower capacity to adsorb oxygen, and higher degree of hydroxylation in the anatase phase. [2.85] In 1972, Fujishima and Honda discovered the phenomenon of photocatalytic splitting of water on a TiO_2 electrode under ultraviolet (UV) light. [2.86] Since then, tremendous efforts have been devoted to the research of TiO_2 material, which is believed to be promising material for energy conversion applications, especially in the field of photovoltaics and photocatalysts.

Doping into TiO_2

Doping of TiO_2 has been an important approach to change the optical and electrical response of semiconductor, especially in the photocatalyst applications. Electronic property of a material is closely related to its chemical composition and the chemical composition of TiO_2 can be altered by doping. It is easier to replace Ti atoms in TiO_2 with a cation than to substitute O atom with another anion because of the difference in the charge states and ionic radii. [2.87] TiO_2 has been doped with many different transition metals. Choi *et al.* performed a systematic study of TiO_2 nanoparticles doped with 21 metal ions such as Fe(III), Mo(V), Ru(III), Os(III), Re(V), V(V) and etc. by the sol-gel method and found the presence of metal ion dopants significantly

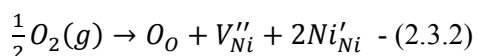
influenced the photoactivity, charge carrier recombination rates, and interfacial electron transfer rates. [2.88] From a chemical point of view, TiO₂ doping is equivalent to the introduction of defect sites like Ti³⁺ into the semiconductor lattice, where the oxidation of Ti³⁺ species is kinetically fast compared with the oxidation of Ti⁴⁺. The dopant content directly influences the rate of e⁻/h⁺ recombination by the equation (2.3.1):

$$W = \frac{2\epsilon\epsilon_0V_s}{eN_d} \quad (2.3.1)$$

where W is the thickness of the space-charge layer, ϵ is the static dielectric constant of the semiconductor, ϵ_0 is the static dielectric constant in a vacuum, V_s is the surface potential, N_d is the number of dopant donor atoms, and e is the electron charge. [2.89] As the concentration of the dopant increases, the space-charge region becomes narrower and the electron-hole pairs within the region are efficiently separated by the large electric field before recombination. Another issue for doping TiO₂ is the band gap engineering. Through metal or non-metal doping into TiO₂ lattice induce a bathochromic shift, i.e., a decrease of the band gap or introduction of intra-band gap states, which results in the absorption of more visible light. [2.88, 2.90, 2.91] By this band gap engineering, the optical property as well as the electrical property of TiO₂ can be controlled.

2.3.2 Nickel Oxide (NiO)

Nickel oxide (NiO) is an oxide semiconductor having excellent chemical stability and a wide band gap in the range of 3.6 – 4.0 eV. [2.92] It has been widely investigated over the decades owing to their interesting optical, electrical and magnetic properties. NiO has a rock salt crystalline structure (*i.e.* NaCl-type structure) and has a lattice constant of 0.417 nm. NiO thin films have been widely investigated as a promising material for the possible applications in gas sensors, [2.93] chemical sensors, [2.94] electrochromic display devices [2.95] and p-type transparent conducting electrodes [2.96] in photovoltaic applications due to their favorable energy-level alignment with several important hole-transport organic semiconductors and high work function. NiO is a Mott–Hubbard insulator at room temperature, but exhibit p-type conduction with the formation of microstructural defects, such as Ni vacancies and interstitial oxygen. [2.97] For instance, the conductivity of NiO enhances by monovalent ion doping such as lithium doping. The incorporation of lithium into NiO results in the formation of Ni³⁺ content equivalent to the amount of lithium added to the solution. [2.97] For each cation vacancy there must be two holes formed. The overall reaction can be explained as bellow (2.3.2):



where V''_{Ni} represents the Ni^{2+} vacancy and the $2Ni'_{Ni}$ represents the Ni^{3+} ions. From the above relation, Ni^{2+} cause the hole conductivity. Each vacancy of Ni^{2+} is replaced by two Ni^{3+} ions, which increase the number of holes as carriers in NiO.

Table 2.3.1 Crystal structures and properties for 3 common TiO₂ polymorphs.
[2.83]

Properties	Rutile	Anatase	Brookite
Crystal Structure	Tetragonal	Tetragonal	Orthorhombic
Lattice constant (Å)	a = 4.5936 c = 2.9587	a = 3.784 c = 9.515	a = 9.184 b = 5.447 c = 5.5154
Space group	P4 ₂ /mnm	I4 ₁ /amd	Pbca
Molecule (cell)	2	2	4
Volume/molecule (Å ³)	31.2160	34.061	32.172
Density (gcm ⁻³)	4.13	3.79	3.99
Ti-O bond length (Å)	1.949 (4) 1.980 (2)	1.937 (4) 1.965 (2)	1.87 – 2.04
O-Ti-O bond angle	81.2° 90.0°	77.7° 92.6°	77.0 - 105°

2.4 Bibliography

- [2.1] W. Siemens, *Van Nortrand's Eng. Mag.* **1885**, 32, 392.
- [2.2] D. Chapin, C. Fuller and G. Pearson, *Journal of Applied Physics* **1954**, 25, 676.
- [2.3] M. A. Green, *Prog. Photovolt: Res. Appl.* **2001**, 9, 123.
- [2.4] M. A. Green, K. Emery, Y. Hishikawa, W. Warta and E. D. Dunlop, *Prog. Photovolt: Res. Appl.* **2014**, 22, 701.
- [2.5] A. S. Brown and M. A. Green, *Phys. E* **2002**, 14, 96.
- [2.6] W. Shockley and H. J. Queisser, *J. Appl. Phys.* **1961**, 32, 510.
- [2.7] K. D. G. I. Jayawardena, L. J. Rozanski, C. A. Mills, M. J. Beliatis, N. A. Nismy and S. R. P. Silva, *Nanoscale* **2013**, 5, 8411.
- [2.8] M. K. Nazeeruddin, E. Baranoff and M. Grätzel, *Solar Energy* **2011**, 85, 1172.
- [2.9] M. K. Nazeeruddin, A. Kay, I. Rodicio, R. Humphry-Baker, E. Muller, P. Liska, N. Vlachopoulos, M. Grätzel, *J. Am. Chem. Soc.* **1993**, 115, 6382.
- [2.10] M. Grätzel, *J. Photochem. Photobiol. C: Photochem. Rev.* **2003**, 4, 145.
- [2.11] T. Takagahara and K. Takeda, *Phys. Rev. B* **1992**, 46, 15578.
- [2.12] A. L. Rogach, L. Katsikas, A. Kornowski, D. Su, A. Eychmüller and H. Weller, *Ber. Bunsen Phys. Chem.* **1996**, 100, 1772.
- [2.13] S. Kan, T. Mokari, E. Rothenberg and U. Banin, *Nat. Mater.* **2003**, 2,

- [2.14] D. Wang, H. Zhao, N. Wu, M. Khakani and D. Ma, *J. Phys. Chem. Lett.* **2010**, 1, 1030.
- [2.15] A. H. Ip, S. M. Thon, S. Hoogland, O. Voznyy, D. Zhitomirsky, R. Debnath, L. Levina, L. R. Rollny, G. H. Carey, A. Fischer, K. W. Kemp, I. J. Kramer, Z. Ning, A. J. Labelle, K. W. Chou, A. Amassian and E. H. Sargent, *Nat. Nanotech.* **2012**, 7, 577.
- [2.16] A. J. Nozik, *Chem. Phys. Lett.* **2008**, 457, 3.
- [2.17] O. E. Semonin, J. M. Luther, S. Choi, H. Y. Chen, J. Gao, A. J. Nozik and M. C Beard, *Science* **2011**, 334, 1530.
- [2.18] J. W. Lee, D. Y. Son, T. K. Ahn, H. W. Shin, I. Y. Kim, S. J. Hwang, M. J. Ko, S. Sul, H. Han and N. G. Park, *Sci. Rep.* **2013**, 3, 1050.
- [2.19] P. K. Santra and Kamat, P. V. *J. Am. Chem. Soc.* **2012**, 134, 2508.
- [2.20] J. J. Choi, Y.-F. Lim, M. E. B. Santiago-Berrios, M. Oh, B.-R. Hyun, L. Sun, A. C. Bartnik, A. Goedhart, G. G. Malliaras, H. D. Abruna, F. W. Wise and T. Hanrath, *Nano Lett.* **2009**, 9, 3749.
- [2.21] K. S. Leschkies, T. J. Beatty, M. S. Kang, D. J. Norris and E. S. Aydil, *ACS Nano* **2009**, 3, 3638.
- [2.22] H. W. Hillhouse and M. C. Beard, *Curr. Opin. Colloid Interface Sci.* **2009**, 14, 245.
- [2.23] R. Loef, A. J. Houtepen, E. Talgorn, J. Schoonman and A. Goossens, *Nano Lett.* **2009**, 9, 856.

- [2.24] M. Dürr, A. Bamedi, A. Yasuda and G. Nelles, *Appl. Phys. Lett.* **2004**, 84, 3397.
- [2.25] S. Soedergren, A. Hagfeldt, J. Olsson and S. E. Lindquist, *J. Phys. Chem.* **1994**, 98, 5552.
- [2.26] P. R. F. Barnes, A. Y. Anderson, S. E. Koops, J. R. Durrant and B. C. O'Regan, *J. Phys. Chem. C* **2009**, 113, 1126.
- [2.27] S. Tirosh, T. Dittrich, A. Ofir, L. Grinis and A. Zaban, *J. Phys. Chem. B* **2006**, 110, 16165.
- [2.28] J. H. Rhee, C. -C. Chung and E. W. -G. Diau, *NPG Asia Mater.* **2013**, 5, e68.
- [2.29] S. Ren, L. Y. Chang, S. K. Lim, J. Zhao, M. Smith, N. Zhao, V. Bulovic, M. Bawendi and S. Gradecak, *Nano Lett.* 2011, 11, 3998.
- [2.30] H. J. Lee, H. C. Leventis, S. J. Moon, P. Chen, S. Ito, S. A. Haque, T. Torres, F. Nüesch, T. Geiger, S. M. Zakeeruddin, M. Grätzel and M. K. Nazeeruddin, *Adv. Funct. Mater.* **2009**, 19, 2735.
- [2.31] T. P. Brennan, P. Ardalan, H. B. R. Lee, J. R. Bakke, I. K. Ding, M. D. McGehee and S. F. Bent, *Adv. Energy Mater.* **2011**, 1, 1169.
- [2.32] L. J. Diguna, Q. Shen, J. Kobayashi and T. Toyoda, *Appl. Phys. Lett.* **2007**, 91, 023116.
- [2.33] D. Celik, M. Krueger, C. Veit, H. F. Schleiermacher, B. Zimmermann, S. Allard, I. Dumsch, U. Scherf, F. Rauscher and P. Niyamakom *Solar Energy Mater. Solar Cells* **2012**, 98, 433.
- [2.34] Y. H. Lee, S. H. Im, J. A. Chang, J. -H. Lee and S. I. Seok, *Org. Electron.* **2012**, 13, 975.

- [2.35] M. Shalom, S. Buhbut, S. Tirosh and A. Zaban, *J. Phys. Chem. Lett.* **2012**, 3, 2436.
- [2.36] J. Gao, J. Luther, O. Semonin, R. Ellingson, A. Nozik and M. Beard, *Nano Lett.* **2011**, 11, 1002.
- [2.37] R. Plass, S. Pelet, J. Krueger, U. Bach and M. Grätzel, *J. Phys. Chem. B* **2002**, 106, 7578.
- [2.38] O. Niitsoo, S. K. Sarkar, C. Pejoux, S. Rühle, D. Cahen and G. Hodes, *J. Photochem. Photobiol. A: Chemistry* **2006**, 181, 306.
- [2.39] Y. L. Lee and Y. S. Lo, *Adv. Funct. Mater.* **2009**, 19, 604.
- [2.40] A. Braga, S. Giménez, I. Concina, A. Vomiero and I. Mora-Seró, *J. Phys. Chem. Lett.* **2011**, 2, 454.
- [2.41] R. Tena-Zaera, J. Elias, G. Wang and C. Levy-Clement, *J. Phys. Chem. C* **2007**, 111, 16706.
- [2.42] M. J. Zheng, L. D. Zhang, G. H. Li and W. Z. Shen, *Chem. Phys. Lett.* **2002**, 363, 123.
- [2.43] D. R. Baker and P. V. Kamat, *Adv. Funct. Mater.* **2009**, 19, 805.
- [2.44] A. Kojima, K. Teshima, Y. Shirai and T. Miyasaka, *J. Am. Chem. Soc.* **2009**, 131, 6050.
- [2.45] J. H. Im, C. R. Lee, J. W. Lee, S. W. Park and N. G. Park, *Nanoscale* **2011**, 3, 4088.
- [2.46] M. M. Lee, J. Teuscher, T. Miyasaka, T. N. Murakami and H. J. Snaith, *Science* **2012**, 338, 643.

- [2.47] N. J. Jeon, J. H. Noh, Y. C. Kim, W. S. Yang, S. Ryu, S. I. Seok, *Nat. Mater.* **2014**, *13*, 897.
- [2.48] M. Grätzel, *Nat. Mater.* **2014**, *13*, 838.
- [2.49] K. Liang, D. B. Mitzi and M. T. Prikas, *Chem. Mater.* **1998**, *10*, 403.
- [2.50] L. Etgar, P. Gao, Z. Xue, Q. Peng, A. K. Chandiran, B. Liu, M. K. Nazeeruddin and M. Grätzel *J. Am. Chem. Soc.* **2012**, *134*, 17396.
- [2.51] H. S. Kim, C. R. Lee, J. H. Im, K. B. Lee, T. Moehl, A. Marchioro, S. J. Moon, R. Humphry-Baker, J. H. Yum, J. E. Moser, M. Grätzel and N. G. Park, *Sci. Rep.* **2012**, *2*, 1.
- [2.52] J. H. Noh, S. H. Im, J. H. Heo, T. N. Mandal and S. I. Seok, *Nano Lett.* **2013**, *13*, 1764.
- [2.53] J. H. Heo, S. H. Im, J. H. Noh, T. N. Mandal, C. S. Lim, J. A. Chang, Y. H. Lee, H. Kim, A. Sarkar, M. K. Nazeeruddin, M. Grätzel and S. I. Seok, *Nat. Photon.* **2013**, *7*, 486.
- [2.54] J. Burschka, N. Pellet, S. J. Moon, R. Humphry-Baker, P. Gao, M. K. Nazeeruddin and M. Grätzel, *Nature* **2013**, *499*, 316.
- [2.55] M. Liu, M. B. Johnston and H. J. Snaith, *Nature* **2013**, *501*, 395.
- [2.56] T. Baikie, Y. Fang, J. M. Kadro, M. Schreyer, F. Wei, S. G. Mhaisalkar, M. Grätzel and T. J. White, *J. Mater. Chem. A* **2013**, *1*, 5628.
- [2.57] S. D. Stranks, G. E. Eperon, G. Grancini, C. Menelaou, M. J. P. Alcocer, T. Leijtens, L. M. Herz, A. Petrozza, H. J. Snaith, *Science* **2013**, *342*, 341.

- [2.58] G. Xing, N. Mathews, S. Sun, S. S. Lim, Y. M. Lam, M. Grätzel, S. Mhaisalkar and T. C. Sum, *Science* **2013**, 342, 344.
- [2.59] L. Hu, J. Peng, W. Wang, Z. Xia, J. Yuan, J. Lu, X. Huang, W. Ma, H. Song, W. Chen, Y.-B. Cheng and J. Tang, *ACS Photonics* **2014**, 1, 547.
- [2.60] J. -Y. Jeng, K. -C. Chen, T. -Y. Chiang, P. -Y. Lin, T. -D. Tsai, Y. -C. Chang, T. -F. Guo, P. Chen, T. -C. Wen and Y. -J. Hsu, *Adv. Mater.* **2014**, 26, 4107.
- [2.61] K. -C. Wang, J. -Y. Jeng, P. -S. Shen, Y. -C. Chang, E. W. -G. Diau, C. -H. Tsai, T. -Y. Chao, H. -C. Hsu, P. -Y. Lin, P. Chen, T. -F. Guo and T. -C. Wen, *Sci. Rep.* **2014**, 4, 1.
- [2.62] S.M. Metev and V.P. Veiko, *Laser Assisted Microtechnology*, Springer, Berlin, Heidelberg, **1994**.
- [2.63] H. M. Smith and A. F. Turner, *Appl. Opt.* **1965**, 4, 147.
- [2.64] D. Dijkkamp, T. Venkatesan, X. D. Wu, S. A. Shareen, N. Jiswari, Y. H. Min-Lee, W. L. McLean, and M. Croft, *Appl. Phys. Lett.* **1987**, 51, 619.
- [2.65] R. Eason, *Pulsed Laser Deposition of Thin Films*, John Wiley & Sons., Inc., Hoboken, New Jersey, **2007**.
- [2.66] I. A. Movtchan, R. W. Dreyfus, W. Marine, M. Sentis, M. Autric, G. Le Lay and N. Merk, *Thin Solid Films* 1995, 255, 286.
- [2.67] I. A. Movtchan, W. Marine, R. W. Dreyfus, H. C. Le, M. Sentis and M.

- Autric, *Appl. Surf. Sci.* **1996**, 251, 96.
- [2.68] D. B. Geohegan, A. A. Puretzky, G. Duscher and S. J. Pennycook, *Appl. Phys. Lett.* **1998**, 72, 2987.
- [2.69] D. B. Geohegan, A. A. Puretzky, G. Duscher and S.J. Pennycook, *Appl. Phys. Lett.* **1998**, 73, 371.
- [2.70] A. M. Morales and C. M. Lieber, *Science* **1998**, 279, 208.
- [2.71] J. R. Morber, Y. Ding, M. S. Haluska, Y. Li, J. P. Liu, Z. L. Wang and R. L. Snyder, *J. Phys. Chem. B* **2006**, 110, 21672.
- [2.72] J. Zuniga-perez, A. Rahm, C. Czekalla, J. Lenzner, M. Lorentz and M. Grundamann, *Nanotechnology* **2007**, 18, 195303.
- [2.73] S. Choopun, H. Tabata and T. Kawai, *J Cryst. Growth* **2005**, 274, 167.
- [2.74] K. Nagashima, T. Yanagida, H. Tanaka, S. Seki, A. Saeki, S. Tagawa and T. Kawai, *J. Am. Chem. Soc.* **2008**, 130, 5378.
- [2.75] J. H. Noh, J. H. Park, H. S. Han, D. H. Kim, B. S. Han, S. Lee, J. Y. Kim, H. S. Jung and K. S. Hong *J. Phys. Chem. C* **2012**, 116, 8102.
- [2.76] M. Fusi, V. Russo, C.S. Casari, A. Li Bassi and C.E. Bottani, *Appl. Surf. Sci.* **2009**, 255, 5334.
- [2.77] M. A. El Khakami, R. Dolbec, A. M. Serventi, M. C. Horrillo, M. Trudeau, R. G. Saint-Jacques, D. G. Rickerby, I. Sayago, *Sens. Actuatur. B: Chem.* **2001**, 77, 383.

- [2.78] F. Sauvage, F. Di Fonzo, A. Li Bassi, C. S. Casari, V. Russo, G. Divitini, C. Ducati, C. E. Bottani, P. Comte and M. Grätzel, *Nano Lett.* **2010**, 10, 2562.
- [2.79] M. H. Lee, J. H. Park, H. S. Han, H. J. Song, I. S. Cho, J. H. Noh and K. S. Hong, *Int. J. Hydrogen Energy* **2014**, 39, 17501.
- [2.80] O. Carp, C. L. Huisman and A. Reller, *Prog. in Solid State Chem.* **2004**, 32, 33.
- [2.81] P. Y. Simons, F. Dacheille and *Acta Cryst.* **1967**, 23, 334.
- [2.82] M. Latroche, L. Brohan, R. Marchand and M. Tournoux, *J. Solid. State Chem.* **1989**, 81, 78.
- [2.83] G. S. Mital and T. Manoj, *Chinese Sci. Bull.* **2011**, 56, 1639.
- [2.84] A. Norotsky, J. C. Jamieson and O. J. Kleppa, *Science* **1967**, 158, 338.
- [2.85] K. Tanaka, M. F. V. Capule and T. Hisanaga, *Chem. Phys. Lett.* **1991**, 187, 73.
- [2.86] A. Fujishima and K. Honda, *Nature* **1972**, 37, 238.
- [2.87] G. K. Mor, O. K. Varghese, M. Paulose, K. Shankar and C. A. Grimes, *Solar Energ. Mater. Solar. Cell* **2006**, 90, 2011.
- [2.88] Y. Choi, A. Termin and M. R. Hoffmann, *J. Phys. Chem.* **1994**, 98, 13669.

- [2.89] A. Fujishima, J. Ohtsuki, T. Yamashita and S. Hayakawa, *Photomed. Photobiol.* **1986**, 8, 45.
- [2.90] R. Subasri, M. Tripathi, K. Murugan, J. Revathi, G. V. N. Rao, T. N. Rao, *Mater. Chem. Phys.* **2010**, 124, 63.
- [2.91] M. Anpo and P. V. Kamat, *Environmentally benign photocatalysts: applications of titanium oxide-based materials*, Springer Science & Business Media, **2010**.
- [2.92] H. J. M. Swagten, G. J. Strijkers, P. J. H. Bloemen, M. M. H. Willekens and W. J. M. Jonge, *Phys. Rev. B* **1996**, 53, 1039.
- [2.93] I. Hotovy, J. Huran, P. Siciliano, S. Capone, L. Spiess and V. Rehacek, *Sens. Actuators B Chem.* **2001**, 78, 126.
- [2.94] H. Kumagai, M. Matsumoto, K. Toyoda, M. Obara, *J Mater. Sci. Lett.* **1996**, 15, 108.
- [2.95] M. Kitao, K. Izawa, K. Urabe, T. Komatsu, S. Kuwano and S. Yam, *Jpn. J Appl. Phys.* **1994**, 33, 6656.
- [2.96] H. Sato, T. Minami, S. Takata and T. Yamada, *Thin Solid Films* **1993**, 236, 27.
- [2.97] E. Antolini, *J Mater. Sci.* **1992**, 27, 3335.

Chapter 3. Experiments

3.1 Synthesis of Nanostructured Semiconducting Oxides

3.1.1 TiO₂ and Nb Doped TiO₂ Anatase Film

Pulsed laser deposition (PLD) system was used for the synthesis of nanostructured semiconducting oxide films using a KrF (248 nm) excimer laser. Figure 3.1.1 represents the schematic image of the PLD system. TiO₂ ceramic target was prepared using high-purity TiO₂ powders (99.99%, High Purity Chemicals, Japan) by a conventional powder method. Niobium (Nb) doped TiO₂ targets were prepared using high-purity TiO₂ (99.99%, High Purity Chemicals, Japan) and Nb₂O₅ (99.99%, High Purity Chemicals, Japan) powders. The powders were mixed by ball-milling with ZrO₂ balls using ethanol as a solvent for 24 h and then dried and granulated. The granulated powders were pressed to form disk-type pellets with a diameter of 2.5 cm and a thickness of 5 mm, followed by sintering at 1300 °C for 2 h. Using the prepared targets and the PLD system, undoped and Nb doped TiO₂ films were deposited onto commercial fluorine-doped tin oxide (FTO) substrates (TEC8, Pilkington) at room temperature and at oxygen pressures ranging from 50

mTorr to 300 mTorr with a pulse energy density of 1.5 Jcm^{-2} and a 5 Hz of repetition rate. The film thickness was controlled by the deposition time. The prepared undoped and Nb doped TiO_2 films were then annealed at $450 \text{ }^\circ\text{C}$ for 1 h in an air atmosphere to crystallize them to the anatase phase. For the better device performance, 100 nm of TiO_2 compact layer, which also deposited by the PLD method, was deposited on the FTO substrate before the deposition of the nanostructured films.

3.1.2 NiO

The nanostructured NiO films were deposited onto patterned glass/tin-doped indium oxide (ITO) substrates. The films were deposited at room temperature and at oxygen pressures ranging from 10 mTorr to 900 mTorr, with a pulse energy density of 3.0 Jcm^{-2} and a repetition rate of 5 Hz. The patterned ITO substrates were cleaned using ultra-sonication in acetone, de-ionized water and ethanol and then dried with a Nitrogen blow gun. The NiO ceramic target, which ablates the NiO material in the form of a plasma plume by a focused pulsed laser, was prepared using high-purity NiO powders (99.99%, High Purity Chemicals, Japan). The film thickness was controlled by the deposition time. The prepared films were subsequently annealed at $200 \text{ }^\circ\text{C}$ for 1 h, in an air atmosphere.

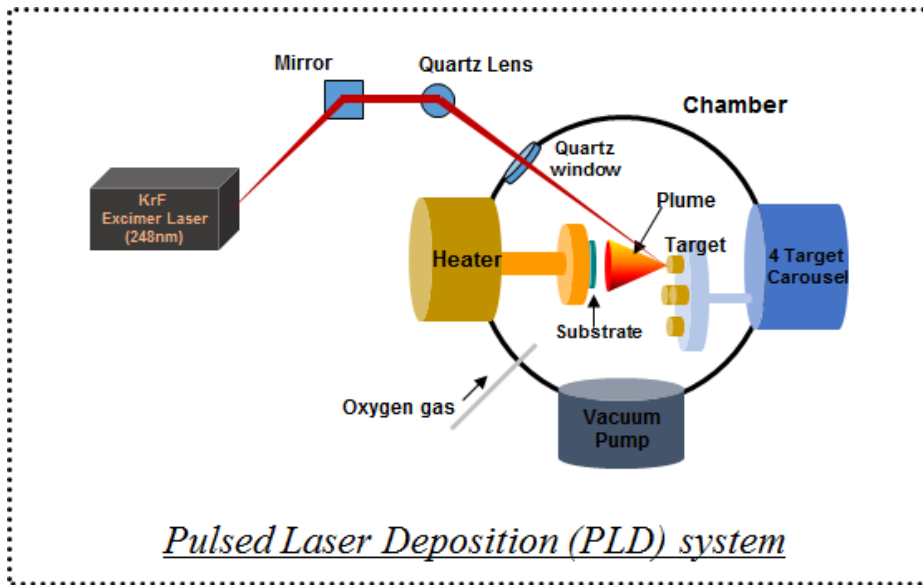


Figure 3.1.1 Schematic image of pulsed laser deposition (PLD) system.

3.2 Preparation of Light Absorbing Materials

3.2.1 Successive Ionic Layer Adsorption and Reaction (SILAR) of Light Absorbing Inorganic Semiconducting Materials

CdS and CdSe onto TiO₂ films

To assemble CdS and CdSe onto TiO₂ electrodes, successive ionic layer adsorption and reaction (SILAR) process was used. [3.1] For the CdS, the TiO₂ films were immersed in an ethanol solution of Cd(NO₃)₂·4H₂O (0.5 M) for 5 min at room temperature (RT), rinsed with ethanol, and then immersed in a methanol solution of Na₂S (0.5 M) for 5 min at RT and rinsed again with methanol. All of these procedures comprise one SILAR cycle. For CdSe, a process similar to that of the CdS was done using an ethanol solution of Cd(NO₃)₂·4H₂O (0.5 M) and an aqueous solution of Na₂SeSO₃. The Na₂SeSO₃ aqueous solution was prepared by refluxing Se powders (0.3 M) in an aqueous solution of Na₂SO₃ (0.6 M) at 70 °C for 7 h. The TiO₂ electrodes were immersed in a Cd(NO₃)₂·4H₂O ethanol solution for 5 min at RT and then in the Na₂SeSO₃ aqueous solution for 1 h at 50 °C. There were four SILAR cycles for CdS and ten SILAR cycles for CdSe. To enhance the crystalline phases of CdS and CdSe, the as-prepared electrodes were heat-treated after the

deposition process. The heat-treatment after the deposition of the CdS and CdSe were done at 300 °C and 150 °C for 30 min, respectively. [3.2] Additionally, ZnS was coated onto the CdS/CdSe-assembled photoelectrodes as a passivation layer. [3.3] The electrodes were dipped into an aqueous solution of $\text{Zn}(\text{CH}_3\text{COO})_2 \cdot 2\text{H}_2\text{O}$ (0.1 M) and Na_2S (0.5 M) for 30 s and rinsed with water for each cycle. There were two SILAR cycles for the absorption of ZnS passivation layer.

PbS and CdS onto TiO_2 films.

PbS and CdS inorganic semiconductors were assembled onto undoped and Nb doped TiO_2 films by successive ionic layer adsorption and reaction (SILAR) process. [3.4] For the PbS, the TiO_2 films were immersed in a methanol solution of 0.02 M $\text{Pb}(\text{NO}_3)_2 \cdot 4\text{H}_2\text{O}$ for 1 min, and then immersed into a solution of 0.02 M $\text{Na}_2\text{S} \cdot 9\text{H}_2\text{O}$ in methanol/water (1:1). Between the procedures, the immersed films were rinsed with methanol or methanol/water for over 1 min and then dried with Nitrogen gas. The above procedures comprise one SILAR cycle. A similar process was accomplished for the CdS adsorption, which mainly assembled as a passivation layer. [3.5] For the CdS, PbS-sensitized NTO films were immersed in an ethanol solution of 0.5 M $\text{Cd}(\text{NO}_3)_2 \cdot 4\text{H}_2\text{O}$ for 5 min, rinsed with ethanol and then immersed in a methanol solution of 0.5 M Na_2S for 5 min and rinsed again with methanol. For the ISSC preparation, there were four SILAR cycles for PbS and seven

SILAR cycles for CdS. ZnS was also coated as a passivation layer.

3.2.2 Preparation of Methyl-ammonium Lead Iodide

For the preparation of methyl-ammonium lead iodide ($\text{CH}_3\text{NH}_3\text{PbI}_3$, MAPbI_3) perovskite light absorbing material, $\text{CH}_3\text{NH}_3\text{I}$ was synthesized from 30 mL hydroiodic acid (57% in water, Aldrich) by reacting 27.86 mL methylamine (40% in methanol, Junsei Chemical Co., Ltd.) in a 250 mL round-bottomed flask at 0 °C for 5 h, by stirring. The precipitates were recovered by evaporation at 60 °C for 1 h. The products, $\text{CH}_3\text{NH}_3\text{I}$, were dissolved in ethanol, recrystallized from diethyl ether, and dried at 60 °C in a vacuum oven for 24 h. The 1 M $\text{CH}_3\text{NH}_3\text{PbI}_3$ solution was prepared by reacting the synthesized $\text{CH}_3\text{NH}_3\text{I}$ powder and PbI_2 (Aldrich) in γ -butyrolactone:DMSO = 7 : 3 at 60 °C for 1 h. The prepared MAPbI_3 precursor solution was deposited onto an ITO/NiO substrate by a consecutive two-step spin-coating process at 1,000 rpm and at 4,000 rpm for 30 and 60 s, respectively, and toluene was dripped onto the substrate during spin coating in the second spin stage. [3.6] The perovskite-precursor coated substrate was dried on a hot plate at 100 °C for 1 min.

3.3 Device Fabrication

3.3.1 Inorganic Semiconductor Sensitized Solar Cells

For the inorganic semiconductor sensitized solar cells (ISSCs) based on CdS and CdSe as a light absorber, the prepared glass/FTO/TiO₂/CdS/CdSe films were fabricated to sandwich-typed solar cells. PbS foils were used as a counter electrodes [3.7] and a polysulfide solution was infiltrated between the electrodes to be used as an electrolyte. The polysulfide redox electrolyte was composed of 1 M Na₂S, 1 M S and 0.1 M NaOH in distilled water. For the PbS and CdS based ISSCs, a Cu₂S sheet was used as a counter electrode and a polysulfide solution as an electrolyte. [3.8, 3.9] The active area of the cells were controlled to 0.16 cm² (0.4 cm x 0.4 cm) using an optical mask.

3.3.2 Perovskite Solar Cells

In order to fabricate an inverted type of perovskite heterojunction solar cells, phenyl-C61-butyric acid methyl ester (PCBM, nano-C) layer was deposited on the prepared glass/ITO/NiO/MAPbI₃ multi-layered films, to be used as an electron transporting layer (ETL). The PCBM layer was deposited by spin-coating the PCBM solution (PCBM concentration of 12 mg·ml⁻¹,

dissolved in 1:1 chloroform/chlorobenzene mixed solvent) at 1,200 rpm for 60 s. Finally, the device was completed with the evaporation of Al contact electrodes in a high vacuum, following the evaporation of the LiF (~0.5 nm) layer through a shadow mask. The active area was 0.04 cm², by masking the active area using a metal mask. All the devices were encapsulated with a glass cap to avoid exposure to oxygen and moisture.

3.4 Characterizations

3.4.1 Inorganic Semiconductor Sensitized Solar Cells

The morphologies were investigated and the characterizations of the crystalline phases of the TiO₂ films and inorganic semiconductors (IS) were accomplished using a field emission scanning electron microscope (FESEM; JSM-6330F, JEOL) and a high-resolution transmission electron microscope (HRTEM; JEM-3000F, JEOL). X-ray diffraction (XRD, D8-Advance, Bruker Miller Co.) analysis was measured to identify the crystal phases. The incorporation of Nb into the TiO₂ was confirmed by X-ray photoelectron spectroscopy (XPS) using an ESCA spectrometer (Al K α X-ray source, SIGMA PROBE). Electron probe micro-analyzer (EPMA; JXA-8900R, JEOL) was used to identify the Nb doping concentration of the NTO films and targets. An energy dispersive X-ray spectroscopy (EDS) analysis was conducted by

means of FESEM (SU-70, Hitachi) and HRTEM. The UV-visible absorption spectra of bare and IS-deposited TiO₂ films were measured by a UV-visible spectrophotometer (Lambda 35, Perkin-Elmer). The photovoltaic properties of the fabricated ISSCs were measured with a potentiostat (CHI 608C, CH Instruments, USA) and a solar simulator (AM 1.5, 100 mWcm⁻², PEC-L11, Peccell). The electrochemical impedance spectra (EIS) were measured by the same potentiostat applying the open-circuit voltage and under illumination. The external quantum efficiency (EQE) was analyzed by a Polaronix K3100 IPCE measurement system (McScience) under the illumination of a 300W Xenon lamp with a monochromator (Oriel Cornerstone). The electron transport time and electron lifetime were characterized by intensity-modulated photocurrent spectroscopy (IMPS) under a short-circuit condition and by intensity-modulated photovoltage spectroscopy (IMVS) under an open-circuit condition, respectively (Zahner, Zennium). A red light-emitting diode (LED, 627 nm) was used as the modulated light source.

3.4.2 Perovskite Solar Cells

The morphologies of the NiO films and the prepared devices were investigated using FESEM (Tescan Mira 3 LMU FEG). The XRD spectra were measured using a Rigaku SmartLab X-ray diffractometer to identify the crystal phase of the prepared films. The transmittance spectra were obtained

using an UV-visible spectrophotometer (Shimadzu UV 2550) in the wavelength range of 300 nm to 900 nm. The photovoltaic performances of the prepared devices were measured using a solar simulator (Newport, Oriel Class A, 91195 A) with a source meter (Keithley 2420) at AM 1.5 G 100 mAc^m-² of illumination and a calibrated Si-reference cell certificated by NREL. The external quantum efficiency (EQE) was measured using a power source (Newport 300 W Xenon lamp, 66920) with a monochromator (Newport Cornerstone 260) and a multimeter (Keithley 2001). Transient photovoltage decay measurements were performed using a nanosecond laser (10 Hz, NT342A-10, EKSPLA) as a small perturbation light source and a Xe lamp (150 W, Zolix) as a bias light source. The device was directly connected to a digital oscilloscope (500 MHz, DSO-X 3054A, Agilent) and the input impedance of the oscilloscope was set to 1 M Ω for an open circuit condition. The bias light intensity was controlled by neutral density filters for various open circuit voltages (V_{oc}) and a strongly attenuated laser pulse of 550 nm, which generated a voltage transient (ΔV) that did not exceed 20 mV.

3.5 Bibliography

- [3.1] Y. L. Lee and Y. S. Lo, *Adv. Funct. Mater.* **2009**, *19*, 604.
- [3.2] C. F. Chi, S. Y. Liau and Y. L. Lee, *Nanotechnology* **2010**, *21*, 25202.
- [3.3] E. M. Barea, M. Shalom, S. Giménez, I. Hod, I. Mora-Seró, A. Zaban and J. Bisquert, *J. Am. Chem. Soc.* **2010**, *132*, 6834.
- [3.4] H. J. Lee, P. Chen, S. J. Moon, F. Sauvage, K. Sivula, T. Bessho, D. Gamelin, P. Comte, S. Zakeeruddin, S. I. Seok, M. Grätzel and M. Nazeeruddin, *Langmuir* **2009**, *25*, 7602.
- [3.5] A. Braga, S. Giménez, I. Concina, A. Vomiero and I. Mora-Seró, *J. Phys. Chem. Lett.* **2011**, *2*, 454.
- [3.6] N. J. Jeon, J. H. Noh, Y. C. Kim, W. S. Yang, S. Ryu, S. I. Seok, *Nat. Mater.* **2014**, *13*, 897.
- [3.7] Z. Tachan, M. Shalom, I. Hod, S. Rühle, S. Tirosh and A. Zaban, *J. Phys. Chem. C* **2011**, *115*, 6162.
- [3.8] G. Hodes and J. Manassen, *J. Electrochem. Soc.* **1980**, *127*, 544.
- [3.9] V. González-Pedro, X. Xu, I. Mora-Seró and J. Bisquert, *ACS Nano* **2010**, *4*, 5783.

Chapter 4. Structural/Compositional Design of

***n-type* Semiconducting Oxide**

4.1 Hierarchically Organized *n-type* TiO₂ Architecture for Highly Efficient Inorganic Semiconductor Sensitized Solar Cells

4.1.1 Introduction

Recently, inorganic semiconductors (IS) have attracted much attention as alternative light absorbers for next-generation solar cells due to their unique optical and electrical properties, such as tunability of the band gap, a high extinction coefficient, and high stability. [4.1 - 4.4] In particular, CdS and CdSe have been recently studied due to their superior performance among the wide variety of inorganic sensitizers available at present, such as PbS, CdS, CdSe, CdTe and Bi₂S₃. [4.5 - 4.8] While CdS/CdSe-sensitized solar cells (CSSCs) have a structure similar to that of dye-sensitized solar cells (DSSCs), their reported efficiencies (~ 5 %) are still far lower than those (~ 12 %) of DSSCs. Many approaches have been developed to enhance the power

conversion efficiency (PCE) of CSSCs. [4.9 - 4.22] Researchers have found that polysulfide electrolyte and Au, Cu₂S or PbS counter electrode materials are better in CSSCs than the combination of iodide electrode and Pt. [4.9, 4.11 – 4.13] In an effort to modify the sensitizer, Hodes *et al.* first reported the co-sensitization of CdS/CdSe on porous TiO₂ films [4.10] and Lee *et al.* showed enhanced cell performance using the co-sensitization. [4.14] Recently, Mn-doped CdS/CdSe sensitizers showed a high power conversion efficiency (PCE) of 5.4%. [4.16]

However, other strategies are needed to overcome the low PCE. Thus far, most CSSCs used a mesoporous TiO₂ film consisting of 20 nm particles of the type that are commonly used in DSSCs as a photoelectrode due to their structural similarity to DSSCs. In CSSCs, however, inorganic semiconductors that are several nanometers thick were deposited on the surface of TiO₂ nanoparticles while organic dye molecules of ~1 nm were absorbed by the monolayer on the surface of TiO₂ in DSSCs. Thus, the development of a photoelectrode may provide a new opportunity for a breakthrough as the configuration of photoelectrodes, including sensitizers, is significantly different between CSSCs and DSSCs. For CSSCs, photoelectrodes should have a large surface area for the adsorption of inorganic sensitizers, which improves the light-harvesting ability. Also necessary is a large pore size or pathway for ion diffusion in electrolytes to avoid the blockage of pores during the CdS/CdSe deposition process. One typical approach to ameliorate the problems of photoanodes based on nanoparticles is the fabrication of 1D-structured TiO₂ photoanodes such as nanorods and nanotubes. [4.23, 4.24]

However, the efficiencies of CSSCs prepared by 1D-structured photoanodes are still low due to their small surface area, resulting in poor light harvesting abilities.

Herein, we synthesized hierarchically organized TiO₂ architectures containing both large surface area and open channels of pores using a pulsed laser deposition (PLD) system. The unique morphology of the TiO₂ architecture prepared by PLD (denoted as PLD-TiO₂) can be controlled by adjusting the kinetic energy of the ablated species during the deposition process. The relationship between the morphology and the final device performance was investigated. For the detailed investigation on the effect of the unique architecture of PLD-TiO₂, the device performance and charge collecting property based on the PLD-TiO₂ and the conventional TiO₂ nanoparticles (denoted as NP-TiO₂) were demonstrated. The large surface area and pore channels of the architecture allowed an efficient infiltration of the electrolyte and a considerable amount of IS to be absorbed with a thin and uniform layer inside the pores. These led to an enhanced electron lifetime through the creation of a pathway for facile ion diffusion.

4.1.2 Characterization of the PLD-TiO₂ Architecture

The unique morphology of the TiO₂ architecture on the glass/FTO substrate is shown in Figure 4.1.2.1. When a high-energy laser focused on the target

surface ablates the target material, a plasma plume consisting of ablated species is formed and deposited on the substrate. By controlling the kinetic energy of the ablated species by adjusting the deposition parameters of the oxygen pressure, laser power and substrate temperature, TiO₂ architectures with different densities and porosities can be fabricated systemically on the substrate. [4.25] As a result, micro-orders of tree-like hierarchically organized porous nanostructures composed of nanoparticles approximately 10 - 15 nm in size (Figure 4.1.2.1c) were successfully synthesized. Open channels of pores were also formed between the nanostructures, as verified by a plane view image of the film. The selected-area diffraction (SAD) results in Figure 4.1.2.1d and X-ray diffraction (XRD) analysis in Figure 4.1.2.2 indicate that the TiO₂ nanostructures were crystallized to anatase phase after the post-annealing process at 450 °C.

CdS was deposited on the bare TiO₂ architecture, after which CdSe was deposited on the CdS-deposited TiO₂ architecture both by SILAR method, as described in the experimental chapter. Figure 4.1.2.3a - c show transmission electron microscopy (TEM) images of bare TiO₂, CdS-deposited TiO₂ and CdS/CdSe-deposited TiO₂ particles which were scraped from each nanostructured film on FTO substrate, respectively. Photographs of each film represented at the inset of Figure 4.1.2.3a - c (right-bottom corner) obviously show that white bare PLD-TiO₂ changed to yellow and red/brown color with the deposition of CdS and CdSe, respectively. Figure 4.1.2.3d shows energy dispersive X-ray spectroscopy (EDS) results of the CdS/CdSe-deposited PLD-TiO₂ sample, indicating that CdS and CdSe were deposited onto the surface of

the PLD-TiO₂ uniformly. The crystalline phases of the CdS and CdSe were determined by a XRD analysis, as shown in Figure 4.1.2.2, demonstrating that the CdS and CdSe were well crystallized and that both have a cubic structure. Additionally, to confirm that the CdS/CdSe were well adsorbed up to the bottom of the film, an EDS analysis of a cross-section of the film was done, as shown in Figure 4.1.2.4. The uniform distribution of the Cd, S, Se and Zn elements from the top to the bottom of the architecture indicates that the CdS/CdSe layers were well coated onto the PLD-TiO₂ photoelectrode.

To investigate the morphology effect of the TiO₂ architecture, the PLD-TiO₂ films were deposited as a function of the oxygen pressure. Figure 4.1.2.5 shows the XRD diffraction patterns of TiO₂ films synthesized at different oxygen pressures. All of the films were well crystallized to anatase phase after post annealing process. Figure 4.1.2.6 shows field emission scanning electron microscopy (FESEM) images synthesized at different oxygen working pressures. The oxygen pressures during deposition significantly influenced the morphology of the films. As shown in the images, the architecture deposited at a low oxygen working pressure of 50 mTorr led to a dense film with no open channels. In contrast, the architecture deposited at a high oxygen working pressure of 300 mTorr had higher porosity with a lot of open channels, but it was expected that the volume portion of TiO₂ on the film seemed to be lower at same thickness compared to other films prepared at lower oxygen pressures. The films deposited between 100 mTorr and 200 mTorr were formed into vertically aligned nanostructured films consisting of open channels, with sufficient volume portion of TiO₂ as well. It is obvious

that the morphology of PLD-TiO₂ nano-architecture are different from the conventional NP-TiO₂ film, as shown in the figure.

In order to examine the morphology influence of the TiO₂ films on the photovoltaic performance, the photocurrent density-voltage (*J-V*) characteristics of CSSCs prepared with the PLD-TiO₂ architectures are shown in Figure 4.1.2.7a, as a function of oxygen pressures. The thickness of all porous electrodes was fixed to approximately 10 μm except for the dense electrode prepared at 50 mTorr (6 μm) as shown Figure 4.1.2.6. Their cell parameters are summarized in Table 4.1.2.1. The morphology of the architecture controlled by the oxygen pressure significantly influenced the cell performances of the prepared CSSCs, especially the short-circuit current (*J_{sc}*) and the fill factor (FF). *J_{sc}* value is mainly related to the light harvesting, charge collecting, and charge injection property of the photoelectrode. In this case, the charge injection property as a function of oxygen pressure can be disregarded because they are all same TiO₂ – CdS/CdSe system. In inorganic semiconductor sensitized solar cells (ISSCs), the distinction of conduction band edge between light absorber and TiO₂ electron acceptor serves as the driving force for electron injection from isolated light absorbers to the conduction band and/or defect states of TiO₂ electrode. [4.26 – 28] The light harvesting property is directly related to the amount of adsorbed CdS and CdSe, which is directly proportional to the internal surface area of the photoelectrode, assuming that the CdS/CdSe light absorbers are formed on the surface of the TiO₂ particles. In the photoelectrode synthesized at 50 mTorr, the CdS/CdSe could not be deposited inside because it was a dense film

without pores which was the main reason for low J_{sc} value. As the oxygen working pressure increased, nanostructured photoelectrodes with an increased surface area were formed, resulting in an increment of J_{sc} . However, J_{sc} was reduced for samples at 200 mTorr and 300 mTorr, which were due to their lack of TiO_2 itself. This result precisely corresponds with the result in the FESEM images in Figure 4.1.2.6. The charge collecting property is related to the recombination between the generated electrons and holes. The reduced recombination denotes the efficient charge collection. As shown in the FESEM images, the open channels of pores were formed and the pores in the film expanded as the oxygen pressure increased. This allowed the electrolytes to penetrate into the inside of the photoelectrode more readily, inducing the acceleration of the redox activity of the electrolytes. [4.29, 4.30] It was confirmed by the electrochemical impedance spectroscopy (EIS) analysis shown in Figure 4.1.2.7b. EIS analysis was conducted to investigate the ionic transportation of prepared CSSCs. The EIS spectra were measured at a frequency range of 10^{-1} Hz to 10^5 Hz at an open circuit potential under the illumination of one sun. According to an equivalent circuit model, Nyquist plots were fitted and the impedance data were fitted using Z View 2.2. The right semicircle in the low-frequency region (0.1 - 10 Hz) in the Nyquist plots is assigned to the impedance of the Nernst diffusion of polysulfide electrolytes. [4.31] As shown in the spectra, the resistance reduced as oxygen pressure increased. This indicates the effective ionic conduction of the polysulfide electrolyte inside the photoelectrode, resulting in the enhanced charge collection. This enhanced redox activity of the electrolytes in the TiO_2

photoelectrode would also contribute to the enhanced FF of the photoelectrode. As shown in Table 4.1.2.1, the FF of the prepared CSSCs showed a steady increment until 150 mTorr and maintains after then. As a result, due to the trade-off between the amounts of adsorbed CdS/CdSe and formation of open channels of pores, we found that the film synthesized at 150 mTorr was the most suitable structure for use as a photoelectrode for CSSCs due to its large internal surface area with sufficient amount of TiO₂ and the open channels of the pores as well.

Figure 4.1.2.8 shows the *J-V* curves of CSSCs as a function of the photoelectrode thickness prepared at 150 mTorr by PLD with the same number of SILAR cycles. The cell parameters are summarized in Table 4.1.2.2. As shown in the figure and the table, high J_{sc} value was achieved at the entire thickness range, and as a result, high PCE over 5.4% was already achieved at 6 μm electrode. The highest PCE of 5.57% was achieved with 23 μm of thickness. To investigate how the developed open-channel architecture showed a high efficiency rating of 5.57% and how the very thick architecture of 23 μm maintained the high efficiency, we investigated its cell performance in detail as compared to a conventional NP-TiO₂ photoelectrode.

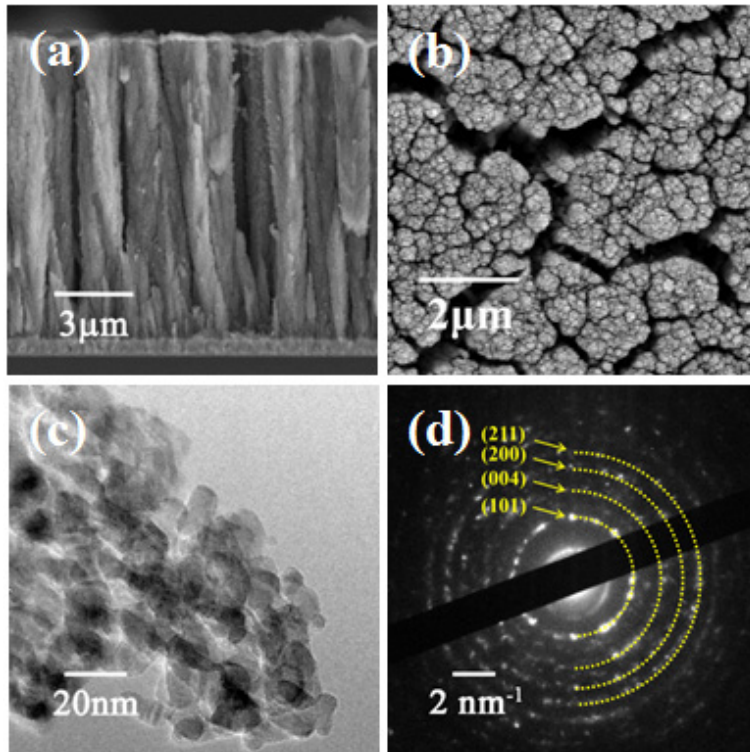


Figure 4.1.2.1 (a) Cross-sectional view and (b) plane view field emission scanning electron microscopy (FESEM) images, (c) high resolution transmission electron microscopy (HRTEM) images and (d) selected area diffraction (SAD) patterns of bare TiO₂ nanostructured films synthesized by pulsed laser deposition (PLD) method.

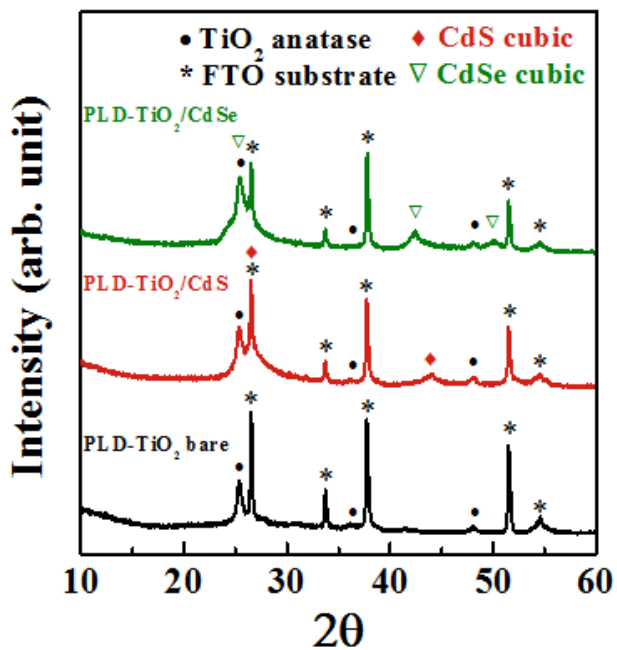


Figure 4.1.2.2 X-ray diffraction (XRD) patterns of bare, CdS and CdSe sensitized PLD-TiO₂ films. CdS and CdSe were deposited by successive ionic layer adsorption and reaction (SILAR) method.

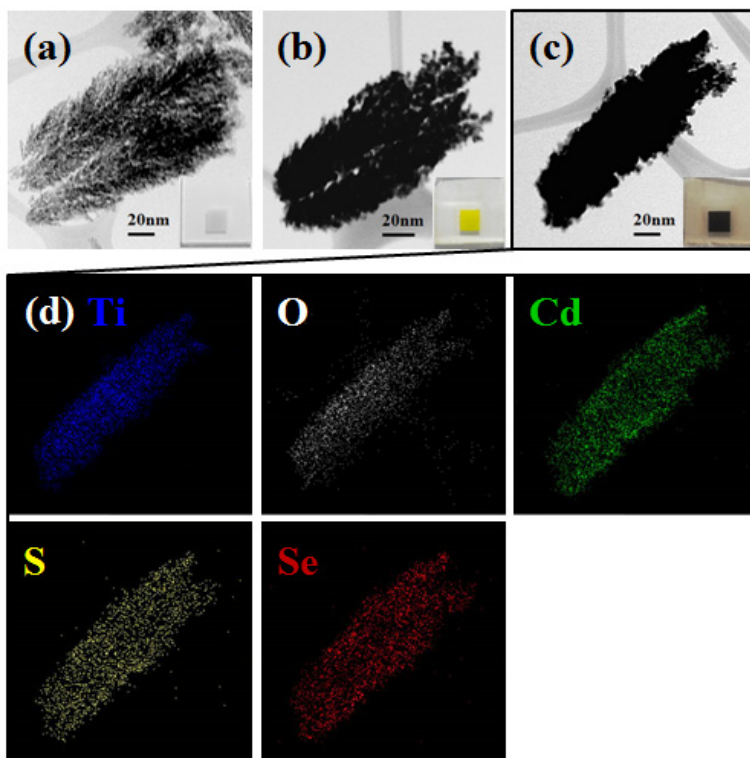


Figure 4.1.2.3 TEM images of (a) bare, (b) CdS sensitized and (c) CdS/CdSe co-sensitized PLD-TiO₂ and (d) energy dispersive X-ray spectroscopy (EDS) elemental mapping images of Ti, O, Cd, S and Se elements in CdS/CdSe co-sensitized PLD-TiO₂ sample. This indicates that the CdS and CdSe are well deposited onto TiO₂ films.

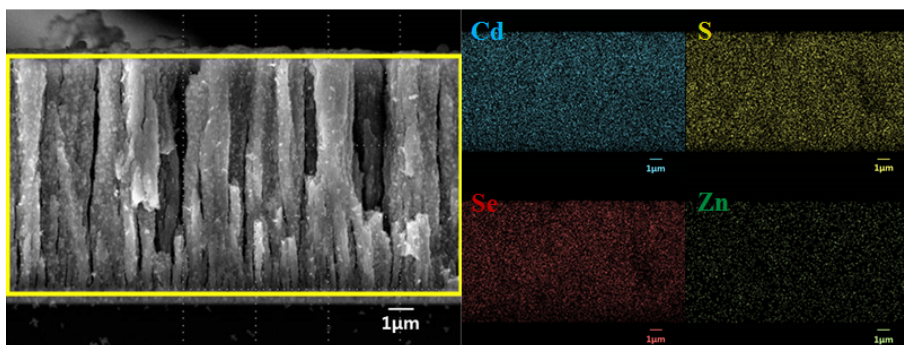


Figure 4.1.2.4 EDS elemental mapping images of Cd, S, Se, and Zn elements across the cross section of PLD-TiO₂ films.

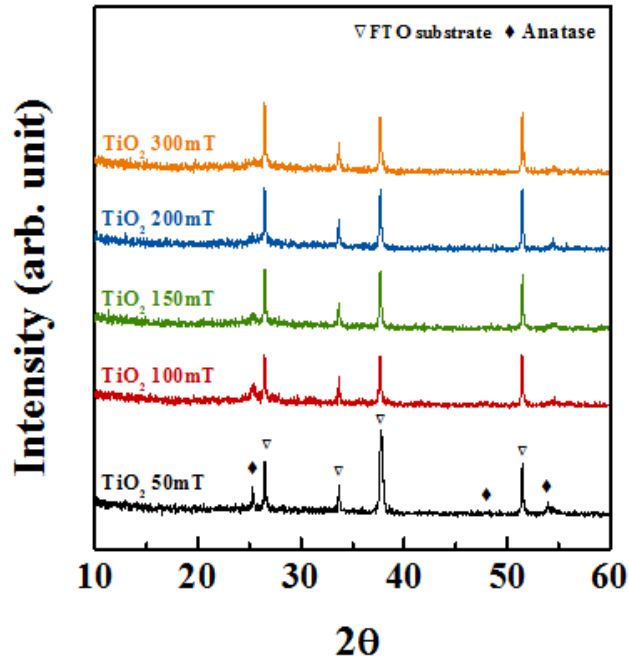


Figure 4.1.2.5 XRD patterns of PLD-TiO₂ films synthesized on glass/fluorine doped tin oxide (FTO) substrate as a function of oxygen pressure.

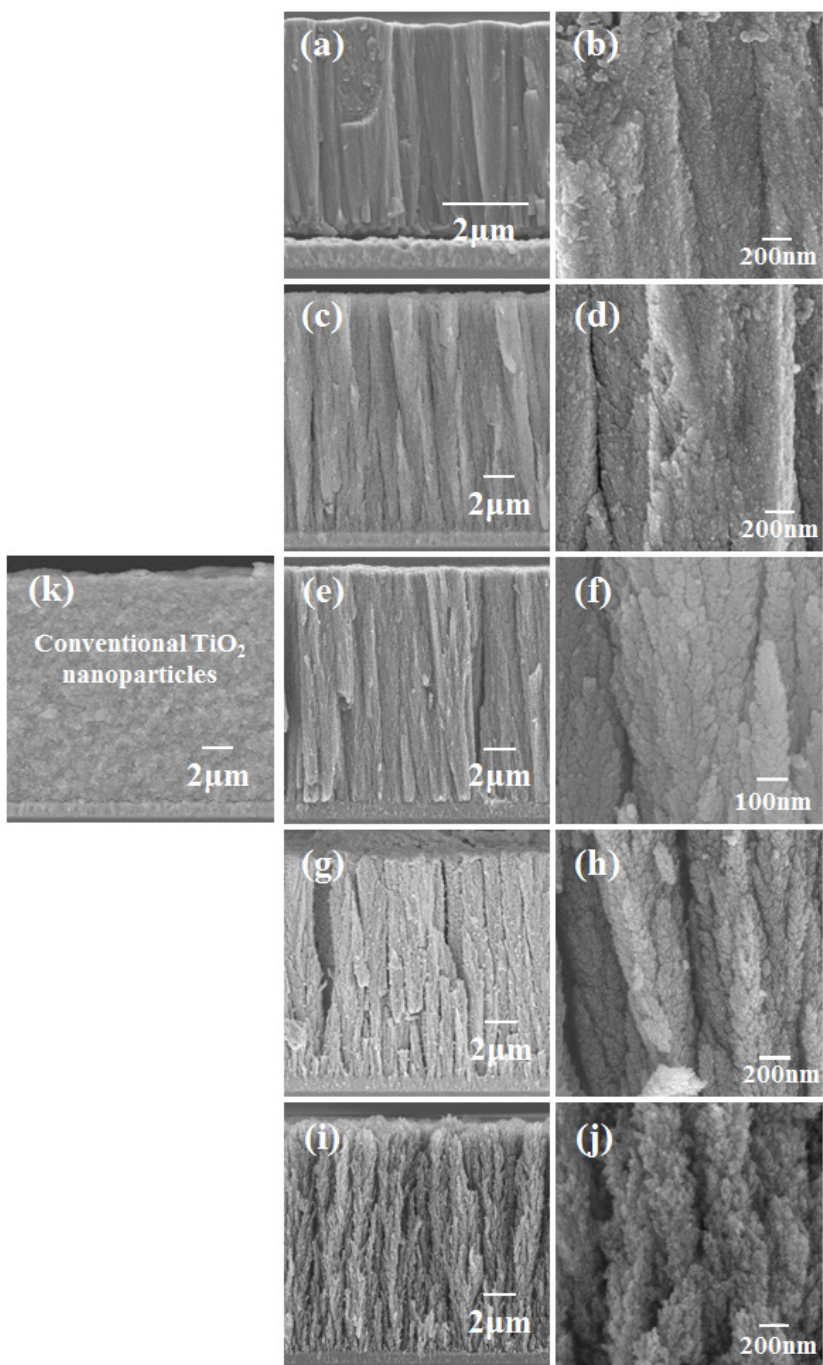


Figure 4.1.2.6 Cross sectional FESEM images of PLD-TiO₂ films synthesized at (a, b) 50 mTorr, (c, d) 100 mTorr, (e, f) 150 mTorr, (g, k) 200 mTorr and (i, j) 300 mTorr. (k) Cross sectional FESEM images of conventional TiO₂ nanoparticle film.

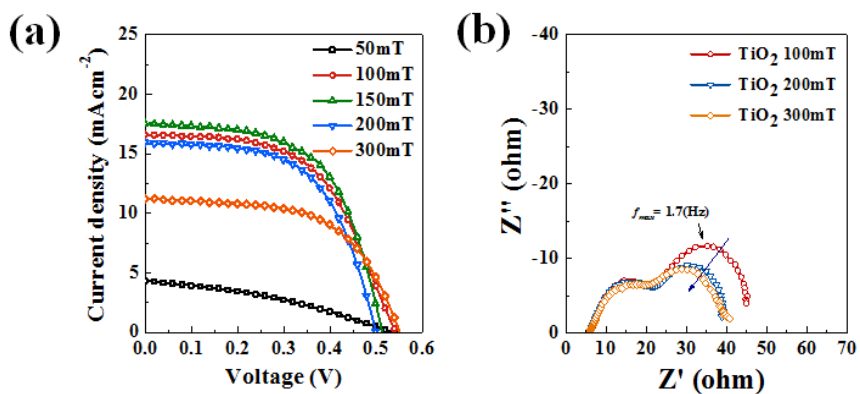


Figure 4.1.2.7 (a) The photocurrent density-voltage (J - V) curves and (b) electrochemical impedance spectroscopy (EIS) of CSSCs using PLD-TiO₂ films with the oxygen pressures of 50, 100, 150, 200 and 300 mTorr. EIS spectra of CSSCs were measured at open circuit potential under light illumination (100 mW/cm²).

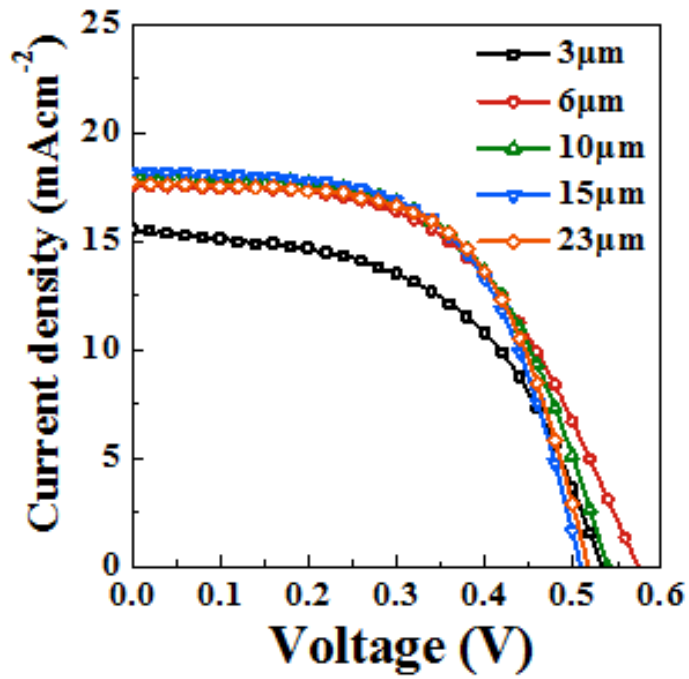


Figure 4.1.2.8 *J*-*V* curves of CSSCs fabricated from PLD-TiO₂ films with different film thickness

Table 4.1.2.1 Photovoltaic parameters of CSSCs as a function of the oxygen gas pressure and the thickness.

Oxygen Pressure	J_{sc} [mA cm ⁻²]	V_{oc} [V]	FF [%]	η [%]
50mT	4.3	0.54	35	0.83
100mT	16.6	0.54	55	4.99
150mT	17.5	0.51	59	5.33
200mT	15.9	0.50	59	4.69
300mT	11.2	0.55	58	3.61

Table 4.1.2.2 Photovoltaic parameters of CSSCs as a function of the thickness.

Thickness	J_{sc} [mA cm ⁻²]	V_{oc} [V]	FF [%]	η [%]
3 μ m	15.6	0.53	53	4.39
6 μ m	17.6	0.57	54	5.42
10 μ m	18.1	0.54	57	5.56
15 μ m	18.2	0.51	60	5.52
23 μ m	17.7	0.52	61	5.57

4.1.3 Photovoltaic Performances of PLD-TiO₂ and NP-TiO₂

In order to investigate the photovoltaic performances of PLD-TiO₂ and NP-TiO₂, devices based on PLD-TiO₂ and NP-TiO₂ were prepared. For the preparation of NP-TiO₂ films, commercial TiO₂ paste (DSL 18NR-T, Dyesol) was screen-printed onto the FTO substrates. The prepared NP-TiO₂ films were then annealed at 450 °C for 1 h to crystallize to the anatase phase. The SILAR cycles for CdS were fixed to four cycles while the thickness of the photoelectrodes was fixed to 12 μm. Figure 4.1.3.1 shows the *J*-*V* characteristics of CSSCs prepared by PLD-TiO₂ and NP-TiO₂ photoelectrodes as a function of the number of CdSe SILAR cycles. The corresponding photovoltaic parameters are summarized in Table 4.1.3.1. In CSSCs based on PLD-TiO₂ photoelectrodes, there were no significant variations in open circuit voltage (*V*_{oc}) and FF as a function of the number of CdSe SILAR cycles. However, *J*_{sc} increased from 12.1 to 16.8 mAcm⁻² with an increase in the number of SILAR cycles due to the increasing amount of CdSe, leading to improved PCE from 3.89% to 5.43%. One interesting finding is that the photoelectrodes based on NPs were ripped off from the TCO electrode during the fabrication of the CSSCs after seven SILAR cycles of CdSe, whereas the PLD-TiO₂-based CSSCs maintained their structure well, even after 10 SILAR cycles of CdSe. This was most likely due to the remarkable adhesion property of the PLD-TiO₂ architecture and its unique architecture with the open channels, which allowed them to withstand the internal stress from largely

adsorbed CdSe. At the same number of SILAR cycles, the PLD-TiO₂ photoelectrodes exhibited significantly higher PCE than the NP-TiO₂ photoelectrodes. To confirm that the cell parameters shown in Table 4.1.3.1 were typical cell performance of PLD and NP-TiO₂ CSSCs, the histograms of cell parameters of other CSSCs that fabricated in the same conditions are shown in Figure 4.1.3.2. The higher efficiency of PLD-TiO₂ were mainly due to the higher J_{sc} and FF values.

Figure 4.1.3.3a illustrates the external quantum efficiency (EQE) spectra of CdS/CdSe sensitized solar cells using PLD-TiO₂ and NP-TiO₂ photoelectrodes. Compared to the cell made with the NP photoelectrode, the EQE of the PLD-TiO₂-based cell increased from 65% to 83% at around 500 nm. In addition, higher EQE values were achieved over the entire visible range (400 nm-750 nm). The higher J_{sc} and EQE for PLD-TiO₂-based cell was attributed to enhancement in both the light-harvesting and charge collecting efficiency. For the investigation of light harvesting efficiency, UV-Vis absorption spectra of CdS/CdSe adsorbed PLD-TiO₂ and NP-TiO₂ films are represented in Figure 4.1.3.3b. The absorption spectra of the PLD-TiO₂ film showed a higher intensity level at all wavelengths compared to those of the NP-TiO₂ film. This result was mainly due to the greater amount of adsorbed CdS/CdSe on PLD-TiO₂ compared to the NP-TiO₂. The unique architecture with open channels of pores in PLD-TiO₂ photoelectrode provides an efficient pathway for CdS/CdSe to adsorb at the surface of TiO₂. The amount of Cd ions absorbed on the photoelectrodes, which can indicate the amount of adsorbed CdS/CdSe, was measured by inductively coupled plasma (ICP)

analysis and described in Table 4.1.3.2. As shown in Table 4.1.3.2, more amount of CdS/CdSe was detected on the PLD-TiO₂ than that of NP-TiO₂ photoelectrode, indicating that more CdS/CdSe semiconductors were deposited on the PLD-TiO₂. It was also confirmed by the Brunauer-Emmett-Teller (BET) measurement in Table 4.1.3.3, which clearly showed that the PLD-TiO₂ photoelectrode (95.89 m²g⁻¹) had a larger surface area than the NP photoelectrode (84.54 m²g⁻¹). Absorbed photon to current efficiency (APCE) curves of prepared devices are represented in Figure 4.1.3.4. The higher APCE value for PLD-TiO₂-based device at almost entire visible wavelength range clearly indicates the higher charge collecting efficiency of PLD-TiO₂.

For the further investigation on the origin of enhanced charge collection of the PLD-TiO₂, electron transport time and lifetime of the prepared CSSCs were analyzed by intensity-modulated photocurrent spectroscopy (IMPS) measured as a function of short-circuit current and intensity-modulated photovoltage spectroscopy (IMVS) measured as a function of open circuit voltage. The results are shown in Figure 4.1.3.5a and b, respectively. The electron transport time τ_d and lifetime τ_n can be calculated using the equation $\tau = (2\pi f_{max})^{-1}$, where f_{max} is the frequency of the minimum IMPS or IMVS imaginary component. [4.32] The electron transport time (τ_d) had higher value for PLD-TiO₂-based CSSC throughout the entire J_{sc} region, which implies a slower electron transport rate of PLD-TiO₂. The reduced electron transport rate was due to the larger surface area and the existence of empty space between the nanoparticles in the PLD-TiO₂ photoelectrode. However, the PLD-TiO₂-based CSSC had a much higher value of the electron lifetime (τ_n)

compared to the NP-TiO₂-based CSSC. The longer electron lifetime led to a longer diffusion length (L_n) according to the equation $L_n = (D_n \tau_n)^{1/2}$, where D_n is the diffusion coefficient derived from the electron transport time τ_d ($D_n = d^2/2.35\tau_d$, d = film thickness). The calculated diffusion length of the PLD-TiO₂ film is $\sim 33 \mu\text{m}$, which was much longer than that of the NP films ($\sim 20 \mu\text{m}$). The longer diffusion length of the PLD-TiO₂ photoelectrode can explain the high efficiency of the thick PLD-TiO₂ photoelectrode of $23 \mu\text{m}$. Moreover, EIS analysis was conducted to investigate the ionic transportation in PLD-TiO₂- and NP-TiO₂-based CSSCs, as shown in Figure 4.1.3.5c. As mentioned above, the right semicircle in the low-frequency region (0.1-10 Hz) in the Nyquist plots is assigned to the impedance of the Nernst diffusion of polysulfide electrolytes. [4.31] The resistance was very low in the PLD-TiO₂ photoelectrode, indicating the effective ionic conduction of the polysulfide electrolyte inside the photoelectrode. These results would also induced a longer electron lifetime due to the reduction of the recombination, which conformed to the higher J_{sc} and FF value of the PLD-TiO₂ photoelectrode.

The longer electron lifetime derived from the IMVS analysis was mainly due to the open channels of the pores in the PLD-TiO₂ film. These open channels of pores can help the CdS/CdSe solution and polysulfide electrolyte to infiltrate more deeply into the film. Schematic illustrations of the structure of the PLD-TiO₂ and NP-TiO₂ photoelectrodes are shown in Figure 4.1.3.6. First, if there are enough pathways for penetration, the CdS and CdSe can be adsorbed more effectively onto the TiO₂ surface, which reduces the back electron transfer at the TiO₂/electrolyte interfaces. This effect is valid if the

pores are larger, which corresponds to the higher J_{sc} and FF value as a function of the oxygen working pressure. Second, the open channels of the pores induce easier infiltration of polysulfide electrolytes, resulting in the improved ionic conduction. In NP-TiO₂ photoelectrodes, the S²⁻ ions have to diffuse through an erratic pore network, oxidize to S_n²⁻ ions, and diffuse back erratically to the PbS counter-electrode, leading to their poor ionic conduction. However, in the PLD-TiO₂ photoelectrode, the bulk electrolytes can diffuse more effectively into the film and diffuse back to PbS catalysts in the counter electrode due to the vertically aligned pore channels. This induces a lower equivalent concentration and a shorter diffusion time of the S_n²⁻ ions, resulting in improved ion diffusion. In consequence, better coverage of CdS/CdSe and enhanced ionic diffusion of the electrolytes due to the open pore channels may reduce the charge recombination process between the TiO₂ and S_n²⁻ ions and lead to a longer lifetime of the CSSC based on the PLD-TiO₂ photoelectrode.

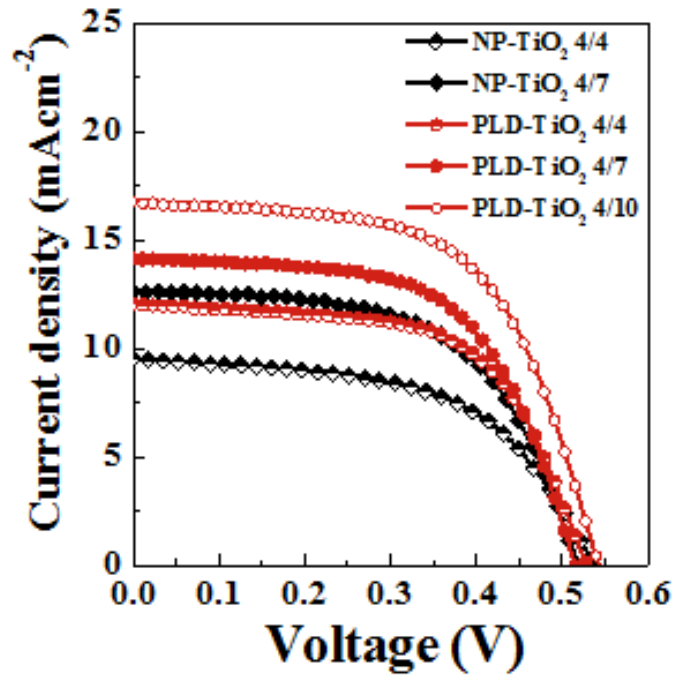


Figure 4.1.3.1 *J-V* curves of CSSCs using PLD-TiO₂ and conventional NP-TiO₂ photoelectrodes with different CdSe SILAR cycles.

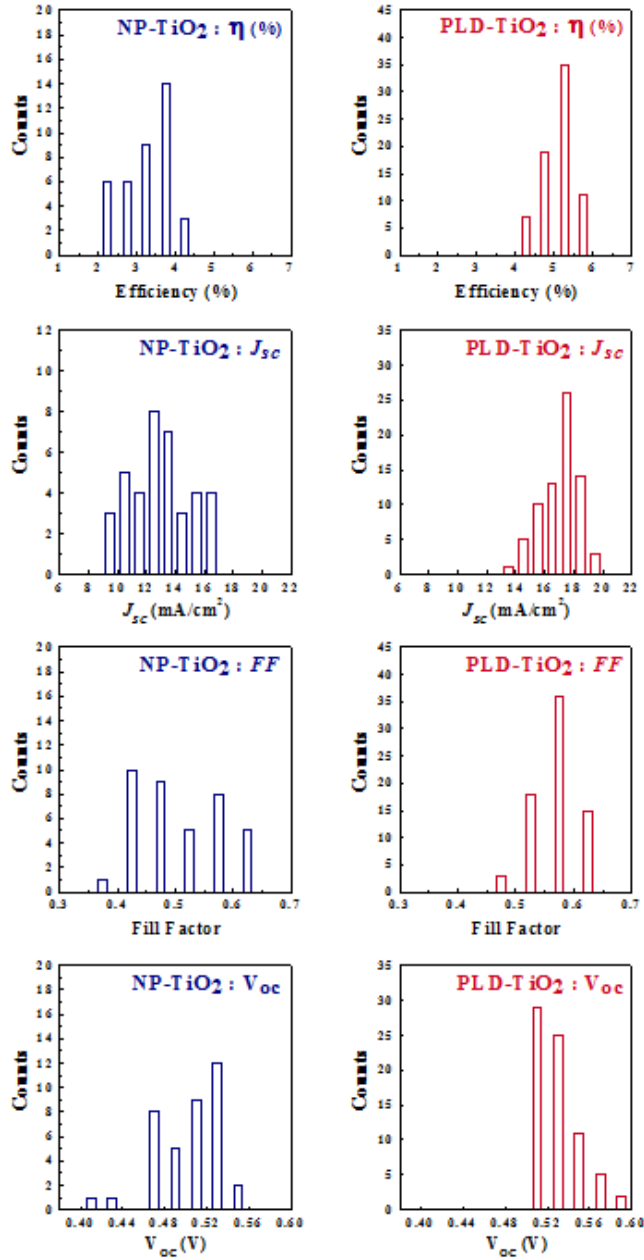


Figure 4.1.3.2 Histogram of solar cell parameters of CSSCs based on CdS/CdSe co-sensitized PLD-TiO₂ (72 cells) and NP-TiO₂ films (38 cells).

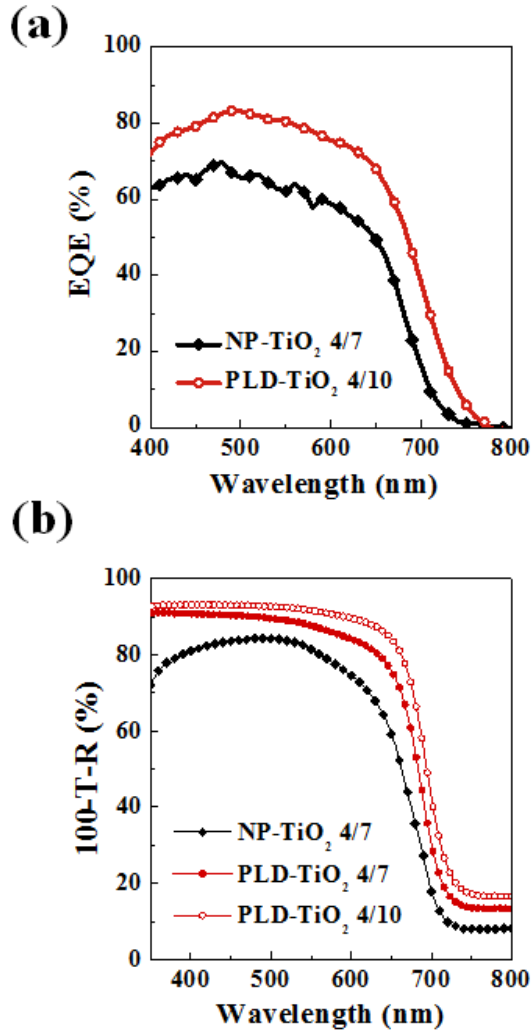


Figure 4.1.3.3 (a) External quantum efficiency (EQE) curves of solar cells based on CdS/CdSe deposited PLD-TiO₂ and NP-TiO₂ films. (b) UV-Vis absorption spectra of CdS/CdSe adsorbed PLD-TiO₂ and NP-TiO₂ films.

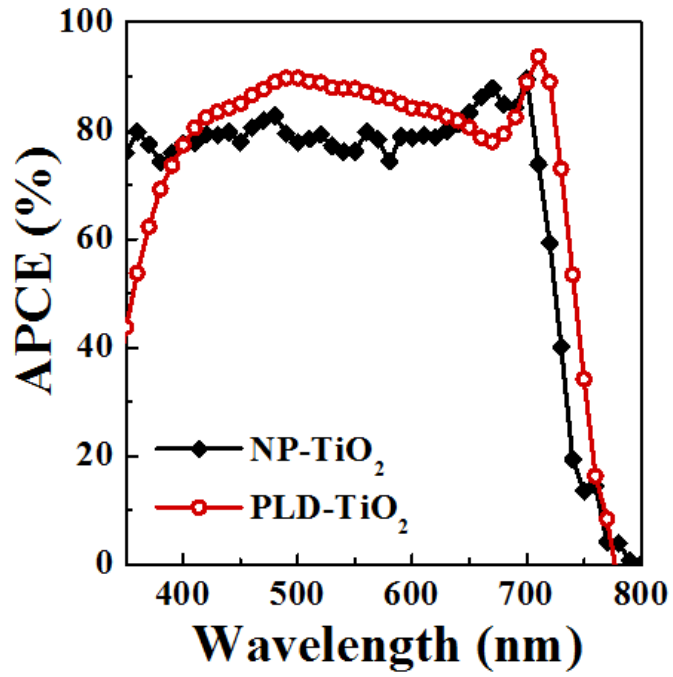


Figure 4.1.3.4 Absorbed photon to current efficiency (APCE) curves of CSSCs based on CdS/CdSe co-sensitized PLD-TiO₂ and NP-TiO₂ films.

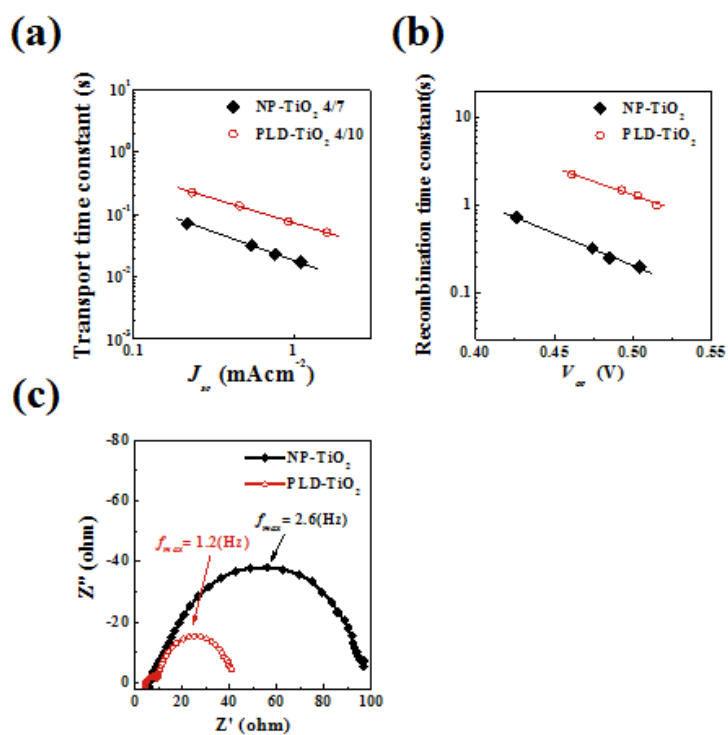


Figure 4.1.3.5 (a) Electron transport time and (b) electron lifetime of prepared CSSCs measured by intensity-modulated photocurrent spectroscopy (IMPS) and intensity-modulated photovoltage spectroscopy (IMVS). (c) EIS spectra of CSSCs based on CdS/CdSe co-sensitized PLD-TiO₂ and NP-TiO₂ films. EIS spectra of CSSCs were measured at open circuit potential under light illumination (100mW/cm²).

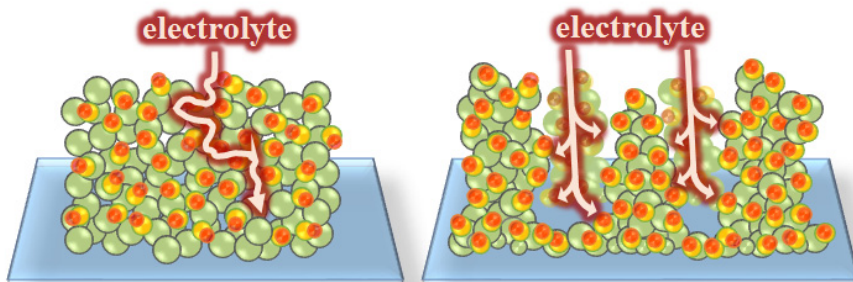


Figure 4.1.3.6 Effect of the open channels of pores on the infiltration of polysulfide electrolyte into the TiO₂ electrode. Scheme on the left is an illustration of conventional NP-TiO₂ film and the right is the vertically aligned column-like nanostructured film synthesized by PLD.

Table 4.1.3.1 Photovoltaic parameters of CSSCs using PLD-TiO₂ and conventional NP-TiO₂ with different numbers of CdSe SILAR cycles.

	J_{sc} [mA cm ⁻²]	V_{oc} [V]	FF [%]	η [%]
NP-TiO₂				
Photoelectrodes				
NP-TiO ₂ 4/4	9.5	0.54	55	2.83
NP-TiO ₂ 4/7	12.6	0.52	58	3.84
NP-TiO ₂ 4/10	-	-	-	-
PLD-TiO₂				
Photoelectrodes				
PLD-TiO ₂ 4/4	12.1	0.53	61	3.89
PLD-TiO ₂ 4/7	14.1	0.52	61	4.41
PLD-TiO ₂ 4/10	16.8	0.54	60	5.43

Table 4.1.3.2 The amount of deposited Cd ions measured by Inductively Coupled Plasma (ICP) analysis on the NP and PLD-TiO₂ photoelectrodes. CdS/CdSe-deposited electrodes were prepared with same area and thickness. The prepared samples were analyzed three times and averaged.

Sample ID (12μm)	Absorbed Cd ions	Absorbed Cd ions
	Per unit area [10 ⁻⁵ mol/cm ²]	Per unit volume [10 ⁻¹ mol/cm ³]
NP-TiO ₂ 4/7	4.0	3.3
PLD-TiO ₂ 4/7	4.8	4.0
PLD-TiO ₂ 4/10	5.3	4.4

Table 4.1.3.3 Internal surface area of PLD and NP-TiO₂ films measured by Brunauer-Emmett-Teller (BET) method.

	PLD-TiO ₂ (150 mTorr)	Conventional NP-TiO ₂
BET (m ² /g)	95.89	84.54

4.1.4 Conclusion

Hierarchically organized TiO₂ architecture with a large surface area and open pore channels was synthesized by the PLD method as a photoelectrode for ISSCs. The connection between the morphology and thickness of the architecture and the cell performance was investigated, demonstrating that CdS/CdSe-sensitized solar cells using PLD-TiO₂ prepared at an oxygen pressure of 150 mTorr show remarkable PCE of 5.57%. This was approximately 46% higher than that of CSSCs based on a conventional NP-TiO₂ photoelectrode. The enhanced efficiency was mainly due to the higher J_{sc} and FF values. The PLD-TiO₂ architecture included a greater amount of CdS/CdSe compared to the NP-TiO₂ photoelectrode due to the larger surface area and the open channels, which may relax the internal stress, resulting in a higher light harvesting property and J_{sc} value. Additionally, owing to their enhanced adhesion property compared to NP-TiO₂, the PLD-TiO₂ accomplished more SILAR cycles, resulting in the improvement of J_{sc} . IMPS and IMVS measurements showed that PLD-TiO₂ architecture had a longer electron lifetime by fivefold compared to the NP-TiO₂ photoelectrode. The open channels of pores in the PLD-TiO₂ architecture assisted the infiltration of the SILAR solution as well as polysulfide electrolyte solution, which led to better coverage of the CdS/CdSe on the surface of TiO₂ and improved S_n²⁻ ion diffusion to the counter electrode, thus slowing down the recombination process. This improved charge collecting property resulted in the improved J_{sc}

and FF value of the photovoltaic performances. Our study demonstrates the importance of a suitable form of photoelectrode architecture for inorganic semiconductor-sensitized solar cells, which may be a clue for the fabrication of efficient CSSCs comparable with other solar cell applications.

4.1.5 Bibliography

- [4.1] S. Rühle, M. Shalom and A. Zaban, *Chem. Phys. Chem.* **2010**, *11*, 2290.
- [4.2] P. V. Kamat, K. Tvrdy, D. Baker and J. G. Radich, *Chem. Rev.* **2010**, *110*, 6664.
- [4.3] W. W. Yu, L. Qu, W. Guo and X. Peng, *Chem. Mater.* **2003**, *15*, 2854.
- [4.4] M. C. Beard, *J. Phys. Chem. Lett.* **2011**, *2*, 1282.
- [4.5] R. Vogel, P. Hoyer and H. Weller, *J. Phys. Chem.* **1994**, *98*, 3183.
- [4.6] H. J. Lee, H. C. Leventis, S. J. Moon, P. Chen, S. Ito, S. A. Haque, T. Torres, F. Nüesch, T. Geiger, S. M. Zakeeruddin, M. Grätzel and M. K. Nazeeruddin, *Adv. Funct. Mater.* **2009**, *19*, 2735.
- [4.7] A. Kongkanand, K. Tvrdy, K. Takechi, M. Kuno and P. V. Kamat, *J. Am. Chem. Soc.* **2008**, *130*, 4007.
- [4.8] J. H. Bang and P. V. Kamat, *ACS Nano* **2009**, *3*, 1467.
- [4.9] G. Hodes, J. Manassen and D. Cahen, *J. Electrochem. Soc.* **1980**, *127*, 544.

- [4.10] O. Niitsoo, S. K. Sarkar, C. Pejoux, S. Rühle, D. Cahen and G. Hodes, *J. Photochem. Photobiol. A: Chemistry* **2006**, 181, 306.
- [4.11] V. Jovanovski, V. González-Pedro, S. Giménez, E. Azaceta, G. Cabañero, H. Grande, R. Tena-Zaera, I. Mora-Seró and J. Bisquert, *J. Am. Chem. Soc.* **2011**, 133, 20156.
- [4.12] S. Giménez, I. Mora-Seró, L. Macor, N. Guijarro, T. Lana-Villarreal, R. Gómez, L. J. Diguna, Q. Shen, T. Toyoda and J. Bisquert, *Nanotechnology* **2009**, 20, 295204.
- [4.13] Z. Tachan, M. Shalom, I. Hod, S. Rühle, S. Tirosh and A. Zaban, *J. Phys. Chem. C* **2011**, 115, 6162.
- [4.14] Y. L. Lee and Y. S. Lo, *Adv. Funct. Mater.* **2009**, 19, 604.
- [4.15] Z. Pan, H. Zhang, K. Cheng, Y. Hou, J. Hua and X. Zhong, *ACS Nano* **2012**, 6, 3982.
- [4.16] P. K. Santra and Kamat, P. V. *J. Am. Chem. Soc.* **2012**, 134, 2508.
- [4.17] S. Rühle, S. Yahav, S. Greenwald and A. Zaban, *J. Phys. Chem. C* **2012**, 116, 17473.
- [4.18] X. Y. Yu, J. Y. Liao, K. Q. Qiu, D. B. Kuang and C. Y. Su, *ACS Nano* **2011**, 5, 9494.
- [4.19] J. H. Im, C. R. Lee, J. W. Lee, S. W. Park and N. G. Park, *Nanoscale* **2011**, 3, 4088.
- [4.20] E. M. Barea, M. Shalom, S. Giménez, I. Hod, I. Mora-Seró, A. Zaban

- and J. Bisquert, *J. Am. Chem. Soc.* **2010**, *132*, 6834.
- [4.21] S. Q. Fan, B. Fang, J. H. Kim, J. J. Kim, J. S. Yu and J. Ko, *Appl. Phys. Lett.* **2010**, *96*, 63501.
- [4.22] B. Fang, M. Kim, S. Q. Fan, J. H. Kim, D. P. Wilkinson, J. Ko and J. S. Yu, *J. Mater. Chem.* **2011**, *21*, 8742.
- [4.23] D. R. Baker and P. V. Kamat, *Adv. Funct. Mater.* **2009**, *19*, 805.
- [4.24] M. Samadpour, S. Giménez, A. I. Zad, N. Taghavinia and I. Mora-Seró, *Phys. Chem. Chem. Phys.* **2012**, *14*, 522.
- [4.25] J. H. Noh, J. H. Park, H. S. Han, D. H. Kim, B. S. Han, S. Lee, J. Y. Kim, H. S. Jung and K. S. Hong, *J. Phys. Chem. C* **2012**, *116*, 8102.
- [4.26] H. Liu, J. Tang, I. Kramer, R. Debnath, G. Koleilat, X. Wang, A. Fisher, R. Li, L. Brzozowski, L. Levina and E. Sargent, *Adv. Mater.* **2011**, *23*, 3832.
- [4.27] A. Braga, S. Giménez, I. Concina, A. Vomiero and I. Mora-Seró, *J. Phys. Chem. Lett.* **2011**, *2*, 454.
- [4.28] D. Wang, H. Zhao, N. Wu, M. Khakani and D. Ma, *J. Phys. Chem. Lett.* **2010**, *1*, 1030.
- [4.29] Y. M. Lee, Y. H. Kim, J. H. Lee, J. H. Park, N. G. Park, W. S. Choe, M. J. Ko and P. J. Yoo, *Adv. Funct. Mater.* **2011**, *21*, 1160.
- [4.30] Y. J. Kim, M. H. Lee, H. J. Kim, G. Lim, Y. S. Choi, N. G. Park, K. Kim and W. I. Lee, *Adv. Mater.* **2009**, *21*, 3668.

[4.31] Q. Wang, J. E. Moser and M. Grätzel, *J. Phys. Chem. B* **2005**, *109*, 14945.

[4.32] J. Krüger, R. Plass, M. Grätzel, P. J. Cameron and L. M. Peter, *J. Phys. Chem. B* **2003**, *107*, 7536.

4.2 Band Engineering of *n-type* TiO₂ Electron Collecting Material by Nb Doping in Inorganic Semiconductor Sensitized Solar Cells

4.2.1 Introduction

N-type semiconducting oxide with wide band gap is one of the key materials in many photovoltaic applications such as dye or inorganic semiconductor-sensitized solar cells (D(I)SSCs), organic photovoltaic cells (OPV), and even perovskite solar cells as an electron accepting and transporting phase. [4.33 – 4.37] Among the emerging photovoltaic (PV) applications, ISSCs have been attracting great attention as alternative to conventional DSSCs due to their unique properties such as multiple exciton generation (MEG) effect, tunability of the band gap, high extinction coefficient, ease of fabrication and low cost. [4.1 – 4.4, 4.38] For the past few decades, many researchers have explored various inorganic semiconductors (IS) and achieved a remarkable enhancement of the power conversion efficiency (PCE) of ISSCs. Among the variety of IS sensitizers available, PbS have been widely studied as a low band gap (< 1.5 eV of E_g) light absorbing material for various solar cell applications [4.26, 4.39, 4.40] owing to its high extinction coefficient and large Bohr radius of 20 nm, which indicates the

easy extension of the absorption band toward the infrared region. [4.42, 4.43] However, in spite of its high theoretical short-circuit current (J_{sc}) of 38 mAcm^{-2} , [4.44] the obtained J_{sc} using PbS as a sensitizer and TiO_2 as an electron acceptor still remain far below than the theoretical value in the previous reports.

One of the main reasons for the deficient J_{sc} is known to be an inefficient electron injection efficiency of the PbS- TiO_2 system. In ISSC system, it is known that the energy difference between the conduction band (CB) edge of light absorber and electron acceptor material serves as a driving force of the electron injection. [4.26 – 28] Thus, many approaches have been investigated to enhance the electron injection ability through enlarging the energy difference by i) size control of IS, ii) introduction of dopants into IS or iii) fine-doping in the electron acceptors. [4.26, 4.28, 4.39, 4.44 – 4.46] M. C. Beard *et al.* demonstrated the effect of PbS quantum dot size on the J - V curves of PbS - ZnO heterojunction quantum dot solar cells. [4.39] Recently, N. G. Park *et al.* achieved a high PCE of 5.58% with J_{sc} of 29.98 mAcm^{-2} by controlling the CB edge of PbS quantum dots through Hg doping. [4.45] Among these three approaches, control of electrical properties for electron accepting inorganic materials such as TiO_2 and ZnO by doping is a general approach to enhance the charge collection in all emerging photovoltaic applications such as ISSC, DSSC, OPV cells and perovskite solar cells. [4.26, 4.46 – 4.51] It is reported that doping metal cation into semiconducting material is a commonly adopted method for tailoring CB position and trap/defect level distribution in semiconducting materials. [4.48 – 4.50]

Pulsed laser deposition (PLD) is one of the most suitable techniques for the composition of fabricated film to be identical with the target material. Thus, PLD is a promising technique to fine-control the composition for fabricating dopant-introduced films. [4.52 – 4.55] Additionally, the PLD technique showed that morphology change in the nanostructured films is insignificant in spite of the introduction of dopants, indicating that the effect of doping can be investigated with the exclusion of other effects such as morphology or particle size change.

Herein, we explored the influence of Niobium (Nb)-doping into nanostructured TiO₂ photoelectrode film on charge injection property in ISSCs among emerging PVs. The undoped and Nb-doped TiO₂ (NTO) nanostructures were synthesized by a PLD technique to use as a photoelectrode in the PbS based ISSCs. PbS and CdS were subsequently deposited onto the NTO films by successive ionic layer adsorption and reaction (SILAR). The solar cell performances were evaluated by using Cu₂S sheet as a counter electrode and a polysulfide solution as a redox electrolyte. The relationship between the Nb doping and the final cell performance was investigated. As a consequence, the J_{sc} value of ISSCs was greatly improved by Nb doping for approximately 41 % compared to the undoped ISSC. According to our analysis, the enhanced J_{sc} and PCE were attributed to the efficient electron injection of PbS-NTO, result from the enlarged energy difference of the CB edge between PbS and TiO₂ by Nb doping.

4.2.2 Characterization of the Nb-doped TiO₂ Nanostructured Films

The morphologies of undoped and Nb-doped TiO₂ nanostructured films synthesized by PLD are shown in Figure 4.2.2.1. The undoped, 0.5 at%, 1 at% and 1.5 at% Nb-doped TiO₂ films were denoted as 0NTO, 0.5NTO, 1NTO and 1.5NTO, respectively. As shown in the field emission scanning electron microscopy (FESEM) images in Figure 4.2.2.1, the morphology of the NTO films maintained regardless of the Nb concentration (0 ~ 1.5 at%). The NTO films were composed of 10 - 15 nm-sized nanoparticles with high crystallinity, as shown in the high resolution transmission electron microscopy (HRTEM) images in Figure 4.2.2.1i and j. The inset images in Figure 4.2.2.1i and j indicates the selected area diffraction (SAD) patterns of 0NTO and 0.5NTO, respectively. The SAD patterns and the X-ray diffraction (XRD) analysis results in Figure 4.2.2.2 reveal that 0NTO, 0.5NTO, 1NTO and 1.5NTO films were crystallized to anatase phase after the post-annealing process, without any secondary or impurity phases. Additionally, to confirm that the PbS and CdS were well adsorbed onto the NTO films, the XRD analysis of PbS- and PbS/CdS-sensitized 0.5NTO film were performed as shown in Figure 4.2.2.3. As shown in the graph, PbS (JCPDF 04-004-4329; cubic) and CdS (JCPDF 01-080-0019; cubic) were successfully synthesized and well deposited onto the NTO films by SILAR method.

Figure 4.2.2.4 represents the electron probe micro-analyzer (EPMA) results of the Nb-doped TiO₂ targets and the deposited films as a function of

Nb concentration. All of the samples were measured 5 times and averaged. As shown in the graph, the Nb concentration of all NTO targets and films were well corresponded to the theoretical Nb contents (planned Nb contents; 0, 0.5, 1.0, 1.5 and 3.0 at%), indicating that the amount of Nb in the NTO films were successfully controlled. Furthermore, the presence of Nb dopants and their chemical states were investigated by X-ray photoelectron spectroscopy (XPS). The XPS spectra of 0, 0.5, 1 and 1.5NTO films are shown in Figure 4.2.2.5a and b. Figure 4.2.2.5a demonstrates the Ti 2p peaks of the NTO films. It confirms that the TiO₂ films were synthesized without change in chemical state of Ti⁴⁺ after Nb doping. In addition, XPS spectra of Nb 3d peaks for undoped and Nb-doped films are shown in Figure 4.2.2.5b. As shown in the spectra, no Nb 3d peaks were detected in the 0NTO sample while clear Nb 3d peaks were detected in the NTO sample. The increased intensity of Nb 3d peaks with the increase of Nb concentration indicates that the Nb ions were successfully incorporated into NTO.

It is known that an introduction of dopants could affect the CB edge of TiO₂ and that the position of the CB edge could be denoted by the flat-band potential (V_{fb}) for the n-type semiconductors. [4.47 – 4.49] Thus, the measurement of V_{fb} could approximately demonstrate the change in the fermi energy (E_F) and CB edge of TiO₂ films by Nb doping. Here, the V_{fb} of NTO films were obtained using a Mott-Schottky analysis, which commonly approached to estimate the V_{fb} from the following equation (4.2.1). [4.56]

$$\frac{1}{C^2} = \frac{2}{\epsilon_s \epsilon_0 N_D} \left(V - V_{fb} - \frac{k_B T}{q} \right) \quad (4.2.1)$$

Where C is the space charge capacitance, ϵ_s and ϵ_0 are the dielectric constants of the TiO₂ films and free space, respectively, N_D is the donor density, V is the applied potential, V_{fb} is the flat-band potential, k_B is Boltzmann's constant, T is the temperature in Kelvin, and q is the electronic charge. According to the equation, the V_{fb} value can be determined from the x-intercepts of the fitted line in the Mott-Schottky plots. Figure 4.2.2.6 shows the Mott-Schottky plots of the NTO films. The Mott-Schottky analysis was performed in a three-electrode cell using NTO film as a working electrode, a convoluted Pt-wire as the counter electrode and a saturated calomel electrode (SCE) as a reference electrode. An aqueous solution of 0.1 M Na₂SO₄ was used as an electrolyte and the active area of the cells was 0.28 cm². The measurements were performed at a frequency of 100 Hz with amplitude of 10 mV. The V_{fb} values obtained from the Mott-Schottky plot were -0.504, -0.404 and -0.366 V vs. SCE for 0NTO, 0.5NTO and 1NTO, respectively, implying that the E_F of TiO₂ was positively shifted with Nb doping. The positive shift is due to the introduction of surface states by Nb dopants. [4.51] To examine the effect of Nb doping on electron injection ability of ISSCs, the cell performance of Nb-doped TiO₂ photoelectrode was investigated.

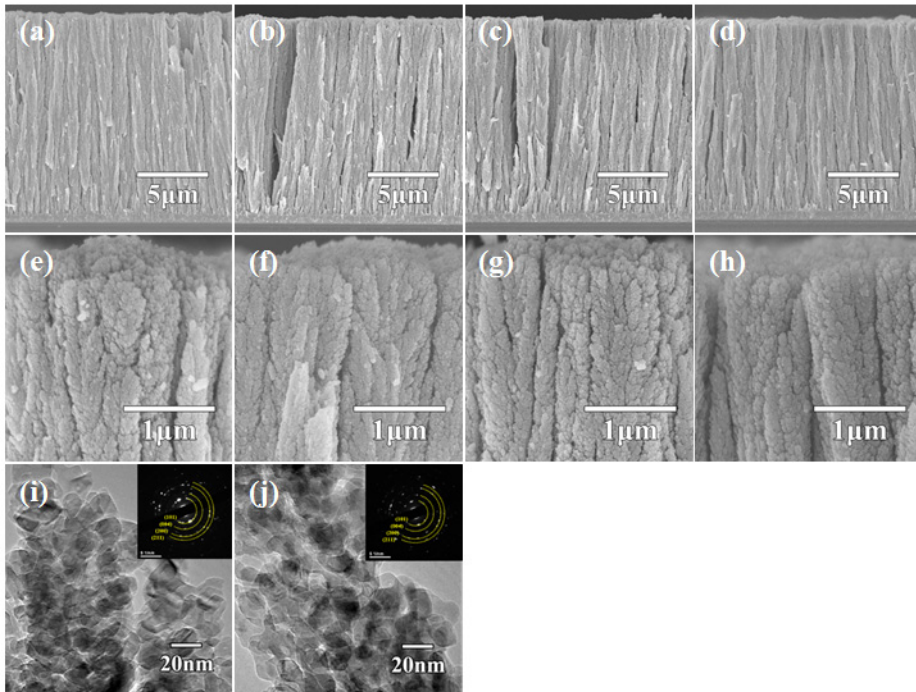


Figure 4.2.2.1 Cross-sectional FESEM images (a, e) undoped and (b, f) 0.5, (c, g) 1.0 and (d, h) 1.5 at% Nb doped TiO_2 films synthesized by PLD method. HRTEM images of (i) undoped and (j) 0.5 at% Nb doped TiO_2 films. The inset images in (i) and (j) indicates the SAD patterns of undoped and 0.5 at% Nb-doped TiO_2 , respectively.

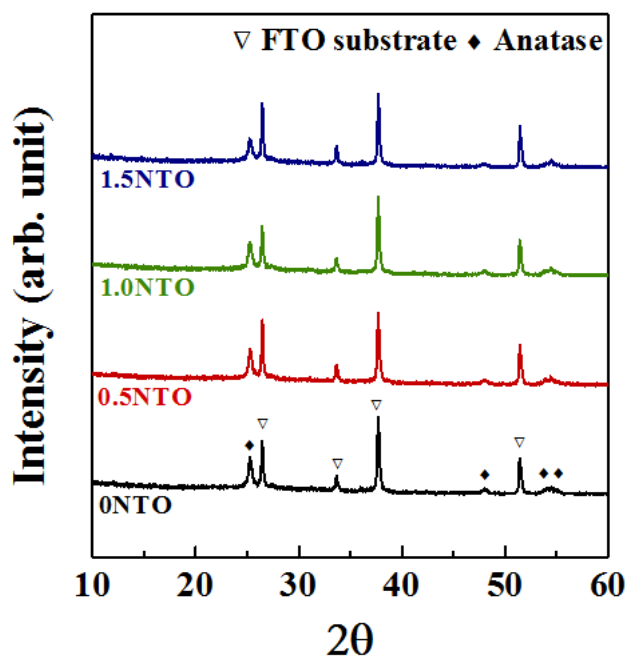


Figure 4.2.2.2 XRD patterns of undoped and Nb-doped (0.5, 1.0 and 1.5 at%) TiO₂ films

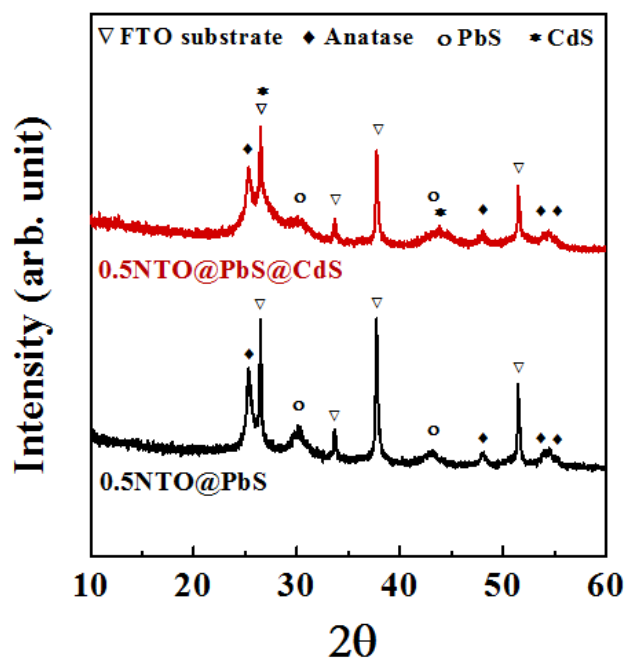


Figure 4.2.2.3 XRD patterns of PbS and PbS/CdS-sensitized Nb-doped TiO_2 films.

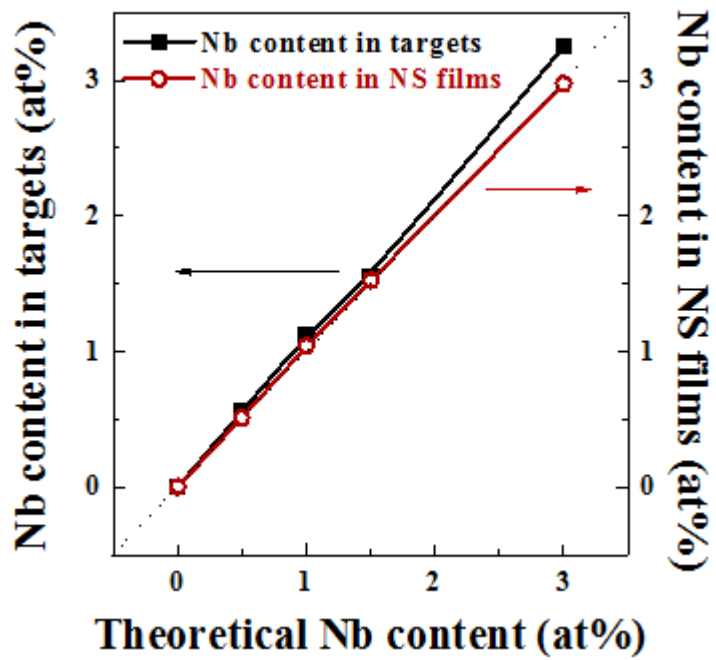


Figure 4.2.2.4 Electron probe micro-analyzer (EPMA) data of prepared Nb-doped TiO₂ targets (filled circles) and the deposited Nb-doped TiO₂ films (hollow circles) as a function of Nb concentration.

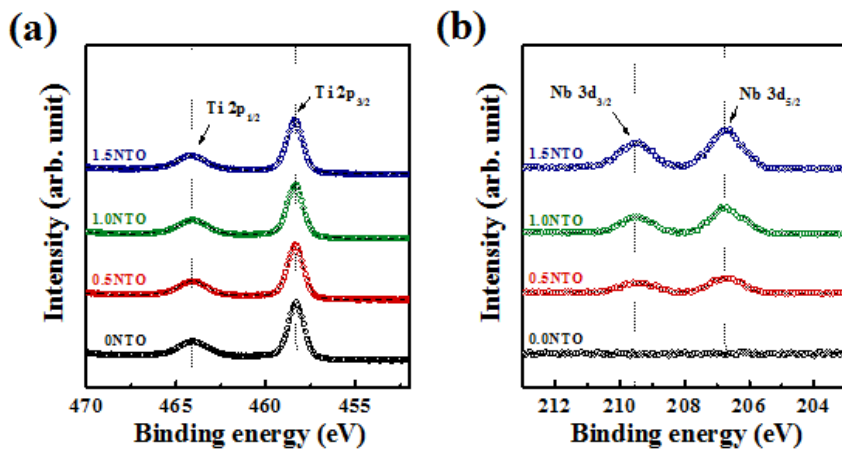


Figure 4.2.2.5 X-ray photoelectron spectroscopy (XPS) spectra of (a) Ti 2p and (b) Nb 3d peaks obtained for undoped and Nb-doped TiO₂ films.

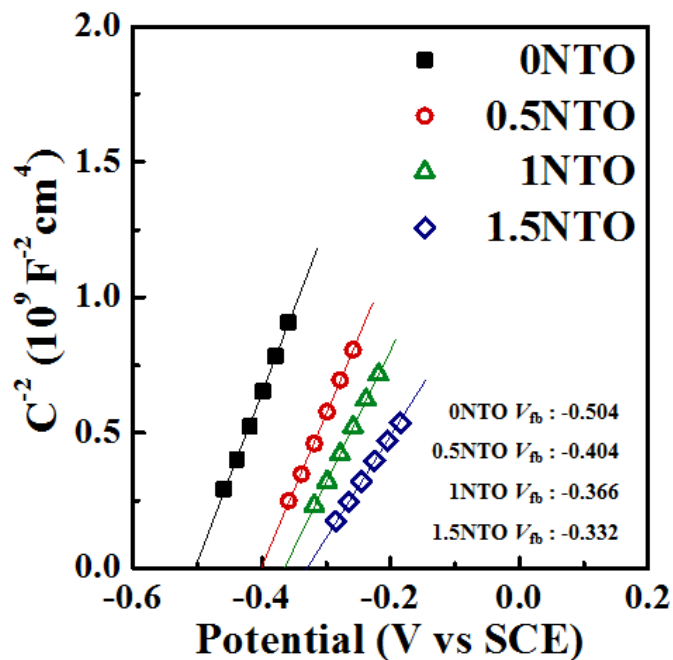


Figure 4.2.2.6 Mott–Schottky plots of the undoped, 0.5, 1.0 and 1.5 at% Nb-doped TiO₂ films. The Mott–Schottky analysis was performed in a three-electrode cell. The TiO₂ films were used as the working electrodes, convoluted Pt-wire as the counter electrode and a saturated calomel electrode (SCE) as the reference electrode. An aqueous solution of 0.1M Na₂SO₄ was used as the electrolyte.

4.2.3 Photovoltaic Performances of Undoped and Nb-doped TiO₂ Photoelectrodes

The photocurrent density-voltage (J - V) characteristics of prepared ISSCs based on NTO photoelectrodes with PbS/CdS sensitization were measured under AM 1.5 G condition (100 mWcm^{-2}) and are displayed in Figure 4.2.3.1. The mean values of the cell parameters are summarized in Table 4.2.3.1. The SILAR cycles for PbS and CdS were fixed to four and seven times, respectively, while the thickness of the photoelectrodes was fixed at $15 \mu\text{m}$. The introduction of Nb strongly influenced the cell performances of the prepared ISSCs in all device parameters including J_{sc} , open circuit voltage (V_{oc}) and fill factor (FF). As shown in the graph and the table, the J_{sc} value significantly increased with 0.5 at% of Nb doping. The 0NTO-ISSC performed a J_{sc} of 17.2 mA cm^{-2} , whereas the 0.5NTO-ISSC performed a J_{sc} of 24.4 mA cm^{-2} . However, with further increment of Nb concentrations, the J_{sc} decreased and the V_{oc} and FF of prepared ISSCs also gradually decreased with Nb doping.

The decrement of V_{oc} was due to the CB edge change of TiO₂ by Nb doping. In a solar cell system, The V_{oc} value corresponds to the energy difference between the quasi-Fermi level of TiO₂ and the redox potential of the electrolyte. [4.57] Since the CB edge positively shifted by Nb doping, which confirmed by the Mott-Schottky analysis in Figure 4.2.2.6, the V_{oc} decreased. On the other hand, the reduction of J_{sc} and FF with further

increment of Nb concentrations more than 0.5 at% can be explained by its diode characteristics. Figure 4.2.3.2 shows the dark J - V curves of prepared ISSCs as a function of Nb concentration. The onset of the dark current occurred at lower forward bias as increasing Nb doping amount, revealing that Nb doping increased the dark currents of ISSCs. The dark J - V characteristics can be described by following equation (4.2.2).

$$J_D = J_0[\exp(qV/mkT)^{-1}] - (4.2.2)$$

where J_D is the dark current density, J_0 is the exchange current density in the dark, q is the elementary charge, V is the applied voltage, k is the Boltzmann constant, T is the temperature and m is the diode ideality factor. It is reported that the FF of a device is significantly influenced by m and J_0 in the equation. [4.58] Therefore, the decreased FF of ISSCs by Nb doping may be associated with their dark J - V characteristics. From these results, we convinced that high concentration of Nb dopants over 0.5 at% in TiO_2 photoelectrode gives a negative effect on the cell performance and fine control of Nb concentration is a key factor for improving the cell performance.

In order to determine the origin of significant increase of J_{sc} through fine Nb doping (0.5 at%), the external quantum efficiency (EQE) of ISSCs based on 0NTO and 0.5NTO were measured as shown in Figure 4.2.3.3. By 0.5 at% of Nb doping, the EQE of the ISSC increased at the entire wavelength range

from 400 nm to 1100 nm. Compared to the 0NTO-ISSC, the average EQE increment of 0.5NTO-ISSC was ~8% for 400 - 500 nm range, ~28% for 500 - 800 nm range and ~58% for 800 - 1100 nm range. It is known that the EQE of solar cell is a production of light harvesting efficiency, electron injection efficiency and charge collecting efficiency.

$$EQE(\lambda) = LHE(\lambda) \times \eta_{inj}(\lambda) \times \eta_{coll}(\lambda) \quad (4.2.3)$$

The light harvesting efficiency (LHE) of the PbS/CdS sensitized 0NTO and 0.5NTO films were obtained using the absorbance spectra, as shown in Figure 4.2.3.4. [4.59, 4.60]

$$LHE = (1 - R) \times (1 - 10^{-A}) \quad (4.2.4)$$

All of the films were thick enough (15 μm) to be fully absorbing. As shown in the graph, the NTO samples showed similar LHE value at the entire wavelength range, indicating that the LHE of the samples were comparable. The LHE results correspond well with the FESEM and HRTEM images in Figure 4.2.2.1, which demonstrating the similar morphology and particle size for undoped and Nb doped films. Since the LHE of the films were comparable,

the EQE results rely on the electron injection and the charge collecting efficiency.

To investigate on the electron transportation and recombination dynamics of prepared ISSCs, intensity-modulated photocurrent spectroscopy (IMPS) was measured as a function of short-circuit current and intensity-modulated photovoltage spectroscopy (IMVS) was measured as a function of open circuit voltage. The results were illustrated in Figure 4.2.3.5a and b, respectively. The electron transport time (τ_d) and the lifetime (τ_n) can be calculated using the equation $\tau = (2\pi f_{max})^{-1}$, where f_{max} is the frequency of the minimum IMPS or IMVS imaginary component. [4.32] As represented in Figure 4.2.3.5a, the electron transport time (τ_d) of 0.5NTO-ISSC showed higher value compared to 0NTO-ISSC throughout the entire J_{sc} region, indicating that the 0.5NTO-ISSC had a slower electron transport rate. The slower electron transport of 0.5NTO-ISSCs was because of the increased trap concentration in TiO_2 by Nb doping. It is known that the trap-limited diffusion process is sensitive to the trap concentration and that the number of traps increases with the introduction of dopants. [4.48] Thus, due to the increased trap concentrations by Nb doping, the electron transport rate decreased. On the other hand, the electron lifetime (τ_n) of ISSCs increased with the introduction of Nb dopants. The increased electron lifetime may due to the enhanced electron injection from PbS to TiO_2 by the positive CB shift of TiO_2 . The detailed explanation about enhanced electron injection will be discussed later. Furthermore, from the obtained electron transport time (τ_d) and the electron lifetime (τ_n), the charge collection efficiency can be measured using the following equation (3). [4.61]

$$\eta_{cc} = 1 - \left(\frac{\tau_d}{\tau_n} \right) \quad (4.2.5)$$

In fact, the exact charge collection efficiency value cannot be calculated using the IMPS and IMVS obtained above because the transport and recombination time constants were measured at short-circuit and open-circuit conditions, respectively, but the comparison value can be calculated. Using the above equation, the comparison value of charge collection efficiency (η_{cc}) were obtained and shown in Figure 4.2.3.5c. As shown in the graph, 0.5NTO-ISSC showed slightly higher η_{cc} compared to that of 0NTO-ISSC, but the efficiency distinction was less than 2% at the entire range. The higher EQE value of 0.5NTO-ISSC in Figure 4.2.3.3 cannot be fully explained by a small increase of η_{cc} by 0.5 at% Nb doping. As a consequence, since both light harvesting and charge collecting efficiencies of prepared ISSCs were comparable, it was convinced that the enhanced EQE was attributed to its enhanced electron injection ability.

The significant enhancement of J_{sc} by 0.5 at% of Nb doping in Figure 4.2.3.1 can be explained by the enhanced electron injection ability. Figure 4.2.3.6 shows schematic illustrations of the structure and the band diagram of the undoped and Nb doped TiO₂. In ISSC system, the energy difference between the conduction band of IS and TiO₂ serves as the driving force for electron injection from the inorganic semiconductors to the conduction band

of TiO₂ electron acceptors. [4.26, 4.27] Thus, the driving force for the electron injection, which is the energy difference of CB edge between PbS and TiO₂, should be high enough for efficient electron injection. As shown in the schematic image, it is reported that the CB position of the nano-sized PbS IS and TiO₂ are similar to each other, [4.6, 4.27] which implies the relatively small driving force for the electron injection. However, after the fine doping of Nb dopants in TiO₂, the CB edge of TiO₂ was positively shifted, which confirmed by the Mott-Schottky analysis in Figure 4.2.2.6, and resulted in the enlarged driving force. This induces a faster electron injection from PbS to NTO CB, resulting in a remarkable enhancement of J_{sc} and EQE in the cell performance. In consequence, the positive shift of the CB of TiO₂ by Nb doping may improve the electron injection efficiency and lead to enhanced J_{sc} and solar cell performances of the ISSC based on the NTO photoelectrodes.

In addition, the enhanced electron injection by Nb doping may also give a positive effect on the electron lifetime obtained by IMVS in Figure 4.2.3.5b. In the previous reports, it is discussed that under light illumination, PbS itself serves as a recombination center due to the surface trap states. [4.27, 4.62] It seems possible that the faster electron injection in PbS-NTO compared to PbS-TiO₂ may induce efficient charge transfer and suppress the charge recombination.

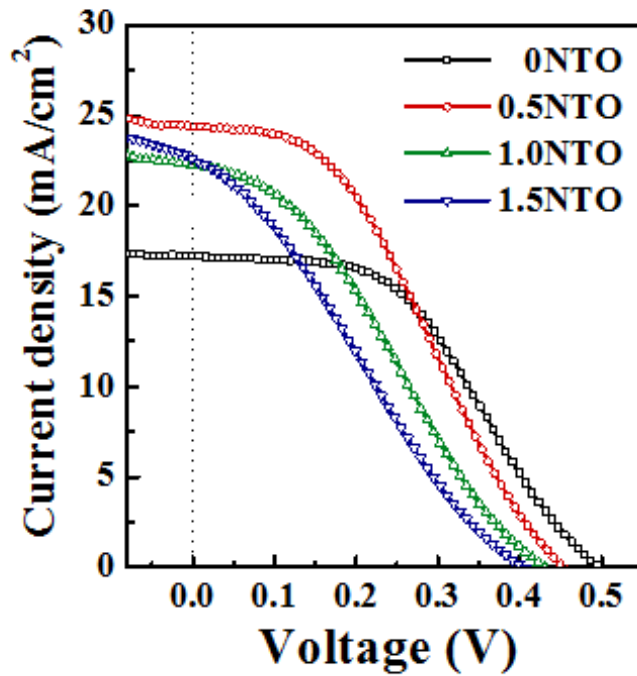


Figure 4.2.3.1 The *J-V* curves of PbS/CdS-sensitized solar cells. The PbS and CdS were adsorbed with the SILAR cycles of 4 and 7, respectively and the thickness of the cells were fixed to 15 μm .

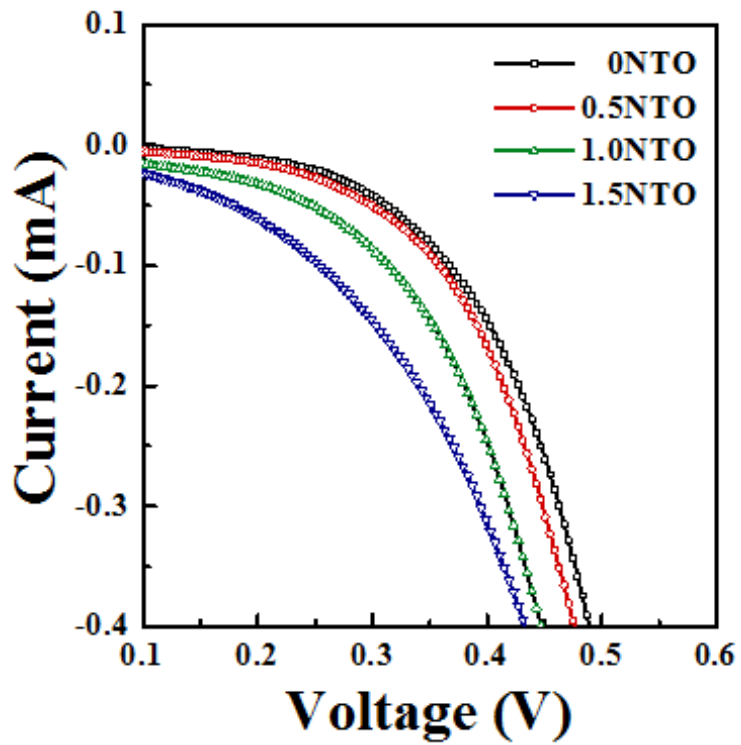


Figure 4.2.3.2 Dark currents of prepared PbS/CdS-sensitized solar cells as a function of Nb doping concentration.

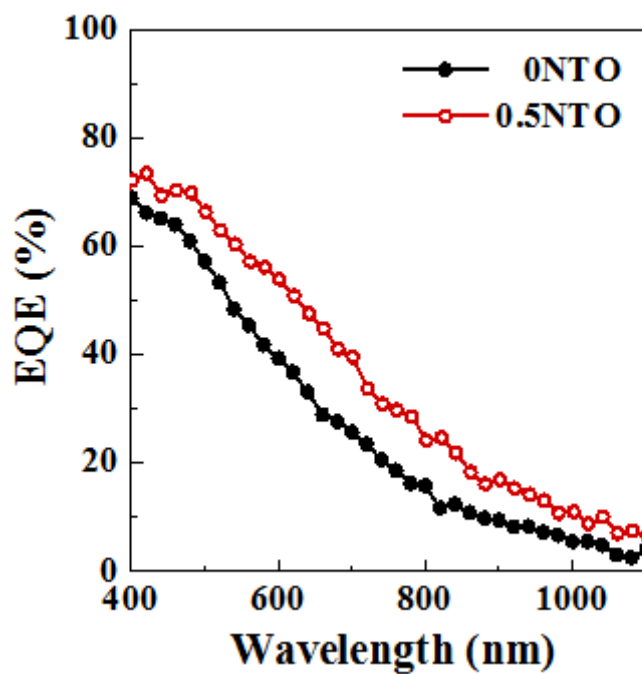


Figure 4.2.3.3 EQE spectra of PbS/CdS-sensitized solar cells based on undoped and 0.5 at% Nb-doped TiO₂ films

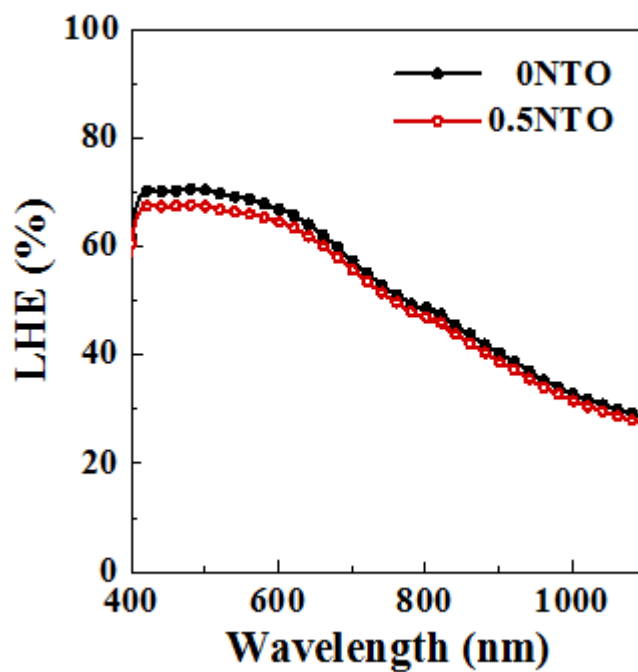


Figure 4.2.3.4 Experimentally determined light harvesting efficiency (LHE) for the PbS/CdS sensitized Nb doped TiO₂ films.

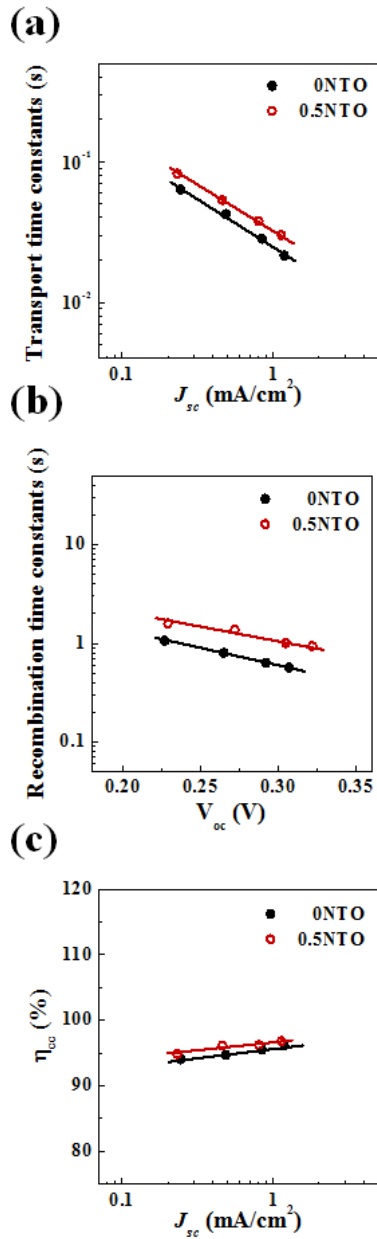


Figure 4.2.3.5 (a) Electron transport time and (b) electron lifetime of ISSCs based on undoped and 0.5 at% Nb doped TiO₂ films measured by IMPS and IMVS. A red light-emitting diode (LED, 627 nm) was used as the modulated light source and (c) the charge collection efficiency calculated with the IMPS and IMVS data.

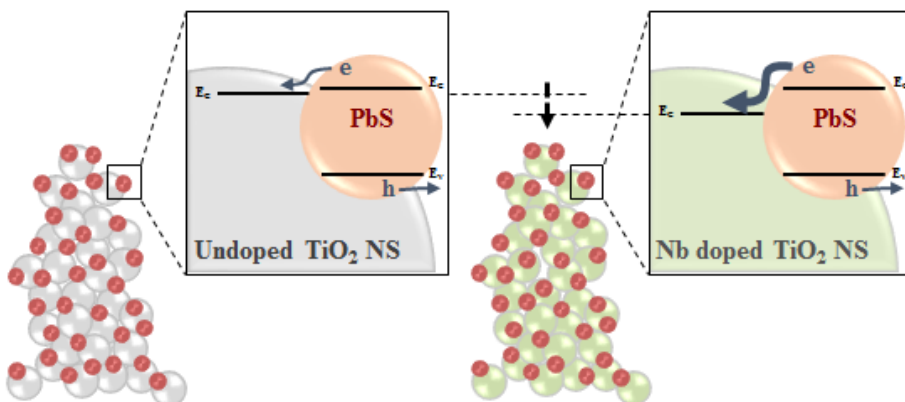


Figure 4.2.3.6 Schematic images and band diagram of PbS sensitized undoped and Nb doped TiO₂ nanostructures.

Table 4.2.3.1 Photovoltaic parameters of prepared ISSCs using undoped and Nb-doped TiO₂ films as the photoelectrode.

	J_{sc} [mA cm ⁻²]	V_{oc} [V]	FF [%]	η [%]
0 NTO	17.2	0.49	45	3.81
0.5 NTO	24.4	0.45	37	4.06
1 NTO	22.2	0.43	32	3.05
1.5 NTO	22.6	0.41	26	2.41

4.2.4 Conclusions

In summary, hierarchically organized undoped and Nb doped TiO₂ nanostructured films were prepared using PLD as a photoelectrode for ISSCs. By PLD, TiO₂ and NTO films having similar morphology and particle size were successfully synthesized. The highest PCE of 4.06% under AM 1.5 simulated solar illumination (100 mWcm⁻²) was obtained with the 0.5NTO-ISSC. The effect of the introduction of Nb dopants on the cell performances was investigated, demonstrating that the ISSCs based on 0.5NTO films showed remarkable enhancement in the EQE and J_{sc} value, compared to the 0NTO-ISSCs. The enhanced PCE and J_{sc} were mainly attributed to the enhanced electron injection ability from PbS to Nb:TiO₂, resulted from the enlargement of gaps between the CB edges of PbS and TiO₂ by the positive shift of the CB edge of TiO₂ by Nb doping. On the other hand, NTO-ISSC with Nb concentrations of 1 and 1.5 at% showed reduced the PCE, mainly owing to the decrease of J_{sc} and FF. The reduction of J_{sc} and FF was attributed to the large dark current as increase of Nb dopants. Consequently, fine-doping (0.5 at%) of Nb into TiO₂ film led to the enhanced electron injection efficiency resulting in improved J_{sc} and PCE.

4.2.5 Bibliography

- [4.33] B. O'Regan and M. Grätzel, *Nature* **1991**, 353, 737.
- [4.34] M. White, D. Olson, S. Shaheen, N. Kopidakis and D. Ginley, *Appl. Phys. Lett.* **2006**, 89, 143517
- [4.35] J. H. Heo, S. H. Im, J. H. Noh, T. Mandal, C. Lim, J. A. Chang, Y. H. Lee, H. J. Kim, A. Sarkar, M. Nazeeruddin, M. Grätzel and S. I. Seok, *Nature Photonics* **2013**, 7, 486.
- [4.36] N. J. Jeon, J. H. Noh, Y. C. Kim, W. S. Yang, S. Ryu and S. I. Seok, *Nature Materials* **2014**, 13, 897.
- [4.37] K. Wojciechowski, M. Saliba, T. Leijtens, A. Abate and H. Snaith, *Energy Environ. Sci.*, **2014**, 7, 1142.
- [4.38] A. Nozik, M. Beard, J. Luther, M. Law, R. Ellingson and J. Johnson, *Chem. Rev.* **2010**, 110, 6873.
- [4.39] J. Gao, J. Luther, O. Semonin, R. Ellingson, A. Nozik and M. Beard, *Nano Lett.* **2011**, 11, 1002.
- [4.40] R. Plass, S. Pelet, J. Krueger, U. Bach and M. Grätzel, *J. Phys. Chem. B* **2002**, 106, 7578.
- [4.41] F. Wise, *Acc. Chem. Res.* **2000**, 33, 773.
- [4.42] B. Hyun, Y. Zhong, A. Bartnik, L. Sun, H. Abruña, F. Wise, J. Goodreau, J. Matthews, T. Leslie and N. Borrelli, *ACS Nano* **2008**, 11, 2206.

- [4.43] F. Meillaud, A. Shah, C. Droz, E. Vallat-Sauvain and C. Miazza, *Sol. Ener. Mater. & Sol. Cells* **2006**, 90, 2952.
- [4.44] O. Semonin, J. Luther, S. Choi, H. Chen, J. Gao, A. Nozik and M. Beard, *Science* **2011**, 334, 1530.
- [4.45] J. W. Lee, D. Y. Son, T. K. Ahn, H. W. Shin, I. Y. Kim, S. J. Hwang, M. J. Ko, S. Sul, H. Han and N. G. Park, *Scientific Reports* **2013**, 3, 1.
- [4.46] B. Ehrler, K. Musselman, M. Böhm, F. Morgenstern, Y. Vaynzof, B. Walker, J. MacManus-Driscoll and N. Greenham, *ACS Nano* **2013**, 7, 4210
- [4.47] K. Wang and H. Teng, *Phys. Chem. Chem. Phys.* **2009**, 11, 9489.
- [4.48] X. Zhang, F. Liu, Q. Huang, G. Zhou and Z. Wang, *J. Phys. Chem. C* **2011**, 115, 12665.
- [4.49] X. Lü, X. Mou, J. Wu, D. Zhang, L. Zhang, F. Huang, F. Xu and S. Huang, *Adv. Funct. Mater.* **2010**, 20, 509.
- [4.50] N. Tsvetkov, L. Larina, O. Shevaleevskiy, E. Al-Ammar and B. T. Ahn, *Prog. Photovolt: Res. Appl.* **2012**, 20, 904.
- [4.51] M. Yang, B. Ding and J. -K. Lee, *J. Power Sources* **2014**, 245, 301.
- [4.52] Y. Furubayashia, T. Hitosugi, Y. Yamamoto, K. Inaba, G. Kinoda, Y. Hirose, T. Shimada and T. Hasegawa, *Appl. Phys. Lett.* **2005**, 86, 252101.
- [4.53] M. Diaconua, H. Schmidta, H. Hochmutha, M. Lorenza, G. Benndorfa, J. Lenznera, D. Spemann and A. Setzera, *Thin Solid Films* **2005**, 486, 117.

- [4.54] J. H. Noh, S. Lee, J. Y. Kim, J. K. Lee, H. S. Han, C. M. Cho, I. S. Cho, H. S. Jung, and K. S. Hong, *J. Phys. Chem. C* **2009**, 113, 1083.
- [4.55] S. Lee, J. H. Noh, H. S. Han, D. K. Yim, D. H. Kim, J. K. Lee, J. Y. Kim, H. S. Jung, and K. S. Hong, *J. Phys. Chem. C* **2009**, 113, 6878.
- [4.56] F. Cardon and W. Gomes, *J. Phys. D: Appl. Phys.* **1978**, 11, L63.
- [4.57] A. Hagfeldt and M. Grätzel, *Chem. Rev.* **1995**, 95, 49.
- [4.58] K. Zhu, S. R. Jang, A. J. Frank, *J. Phys. Chem. Lett.* **2011**, 2, 1070.
- [4.59] Y. Tachibana, K. Hara, K. Sayama and H. Arakawa, *Chem. Mater.* **2002**, 14, 2527.
- [4.60] P. Tiwana, P. Docampo, M. Johnston, H. Snaith and L. Herz, *ACS Nano* **2011**, 5, 5158.
- [4.61] G. Schlichthörl, N. G. Park, A. J. Frank, *J. Phys. Chem. B* **1999**, 103, 782.
- [4.62] J. H. Rhee, C. -C. Chung and E. W. -G. Diau, *NPG Asia Mater.* **2013**, 5, e68.

Chapter 5. Structural Design of *p-type*

Semiconducting Oxide

5.1 Nanostructured *p-type* NiO as an Efficient Hole

Collecting Layer in Inverted Perovskite Solar Cells

5.1.1 Introduction

Methylammonium lead iodide perovskites ($\text{CH}_3\text{NH}_3\text{PbI}_3$, MAPbI_3) have been intensively investigated as a light absorber for efficient solution-processable solar cells. This is because they exhibit many advantages, such as broad range for light absorption with high extinction coefficient, ambipolar transport property, and long electron-hole diffusion length. [5.1 – 5.14] These allow for diversity in the device architecture. In 2009, Miyasaka and coworkers adopted MAPbI_3 as an alternative to a light harvester in a dye-sensitized configuration with a mesoporous TiO_2 template. [5.2] Since then, significant progresses in solar cell performance have been established by virtue of improvement in device structures, including meso-superstructured, [5.5] mesostructured, [5.4] and bi-layer architecture. [5.8] These structures mostly employ mesoporous (mp)-metal oxide layers, which require high-

temperature processing.

Meanwhile, a planar heterojunction architecture which can avoid the use of mp-metal oxide was also reported, [5.10] where the devices based on the perovskite, such as MAPbI₃, can be fabricated with either n-i-p or p-i-n structure due to the ambipolar semiconducting characteristic of the perovskite. [5.8] However, n-i-p type MAPbI₃ planar cells sandwiched between TiO₂ and hole transporting layer suffered from a serious hysteresis, which should be reduced, in photocurrent–voltage (*J*-*V*) characteristics compared with that of p-i-n cells. [5.15, 5.16] Therefore, p-i-n type MAPbI₃ planar cells are beneficial to improving the exciton separation, and charge transportation and collection for a suppressed *J*-*V* hysteresis. In order to realize such p-i-n type solar cells, a stable p-type electrode is indispensable. To date, poly(3,4-ethylenedioxythiophene): polystyrene sulfonate (PEDOT:PSS) and NiO thin layer have been widely used as a p-type electrode for p-i-n MAPbI₃ planar cells, but the overall cell performance remains behind that of n-i-p using thin mp-metal oxide layers. This result has provoked our interest toward the use of thin nanostructured p-type NiO thin film to further improve the performance of p-i-n MAPbI₃ planar solar cells. Compared with the organic p-type hole transporting layer (HTL), such as PEDOT:PSS, inorganic NiO thin film HTL is preferred for its superior stability against degradation by the exposure to atmosphere for a long time and inherent material stability. [5.17]

There have been several approaches to prepare a NiO (or NiO_x) film, including sol-gel process, electro-deposition, sputtering, and pulsed laser

deposition (PLD), which could be adopted for fabrication of organic photovoltaic (OPV) devices and dye-sensitized solar cells (DSSCs). [5.18 – 5.21] Guo and Chen *et al.* firstly applied a thin NiO_x layer as the HTL to the MAPbI₃- phenyl-C61-butyric acid methyl ester (PCBM) heterojunction solar cell, which showed power conversion efficiency (PCE) of 7.8%. [5.22] Subsequently, a mp-NiO film was prepared on top of the NiO_x layer in order to build a mesoscopic NiO/MAPbI₃/PCBM junction device, which demonstrated a high open circuit voltage (V_{oc}) of 1.04 V and a PCE of 9.51%. [5.23] However, only a relatively low short circuit current (J_{sc}) of 13.24 mA·cm⁻² and a fill factor (FF) of 69% were achieved from the same device. They recently further improved the overall efficiency (up to 11.6%) by replacing a solution-processed NiO_x layer with a sputtered NiO_x thin film. [5.24] However, the presence of the thick mp-NiO layer still demonstrates a low external quantum efficiency (EQE) response (below 500 nm) because of its significant light absorption. Furthermore, it requires a high-temperature process of 400 °C. In general, most devices that included a NiO (or NiO_x) layer as HTL have suffered from a lower FF value (which seldom reaches 70 %), in comparison to the devices adopting PEDOT:PSS. Such problems have been partly solved in recent works, where copper was incorporated into NiO_x as a dopant, or a hybrid interfacial layer of a thin NiO film with a meso-Al₂O₃ scaffold was used. As a result, the overall PCE could be increased to over 15%. [5.25, 5.26] Despite these recent progresses, the overall performance of cells fabricated with a p-i-n architecture is still inferior to the performance of cells with the n-i-p architecture, requiring more efforts for

finding a new breakthrough in NiO-based perovskite solar cells.

Oxides are generally poor electronic conductor, due to the presence of large energy gap. Fluorine p-type oxide semiconductors are even rarer compared with the n-type oxide semiconductors. NiO is one of the rare p-type conductors thanks to its metal-deficient nature. In addition, its small electron affinity (~ 1.8 eV) and relatively large band gap (~ 3.4 eV) make it suitable as the HTL in perovskite solar cells, which would suppress the electron leakage by the high conduction band offset, and enhance the hole transport due to the small valence band offset with MAPbI₃. The high band gap also ensures high light transmittance. Nevertheless, low hole mobility in NiO, due to relatively localized orbital nature of mostly O2p character of its valence band requires that thickness of NiO HTL must be minimized to carry well the dissociated holes to cathode. However, too thin NiO HTL could induce electron leakage problem, so there must be elaborative engineering work to optimize the NiO microstructure and thickness to maximize the performances of perovskite-based solar cells.

In this study, we have prepared a well-ordered nanostructured NiO film with a good optical transparency through a PLD method. PLD is a feasible thin film growth method, where the high energy of ejected particles from the target with the help of laser plume can largely contribute to the improvement of crystalline quality of the film even at such a low temperature. In addition, the growth environment, such as oxygen partial pressure, can be easily adjusted to achieve the optimum microstructure of the film as the HTL for perovskite solar cells. Using the NiO film deposited by PLD on tin doped

indium oxide (ITO) substrate, we have fabricated a planar heterojunction of MAPbI₃-PCBM. The newly developed nanostructured NiO film exhibited a high FF value of 81.3% and an overall PCE of 17.3%.

5.1.2 Characterization of NiO Nanostructures

In PLD method, the morphology and density of the deposited materials can be varied by adjusting the deposition parameters, such as the oxygen partial pressure. [5.27, 5.28] Figure 5.1.2.1a shows the cross-sectional and plane-view field emission-scanning electron microscopy (FESEM) images of prepared NiO films by PLD. The films were prepared on the glass/ITO substrates with the post-annealing temperature of 200 °C for 1 h. Unlike the photoelectrodes used in the inorganic semiconductor sensitized solar cells (ISSCs) introduced in the previous chapter, the hole transporting NiO layers were prepared as thin layers having thickness less than 150 nm, since the perovskite solar cells are based on layered structures. From the preliminary tests, it was found that the film grown at the oxygen partial pressure of 10 mTorr (mT) caused too high series resistance to fabricate a working perovskite solar cell when the film was thicker than ~50 nm. Therefore, a 30 nm of thickness was adopted only for this oxygen partial pressure condition to compare it with other devices containing NiO films grown at higher oxygen partial pressures. Other films were deposited to the same thickness of approximately 150 nm to compare their optical transmittances and device

performances.

At a pressure of 10 mT, a highly dense and smooth NiO film was obtained. As the oxygen partial pressure increased during growth, the densely packed and planar morphology became more porous and rougher. At a pressure of 200 mT, an ordered, column-shaped NiO nanostructure was formed during growth. In contrast, at pressures over 500 mT, the surfaces appeared relatively rough containing many voids, making the morphology similar to a typical mesoscopic structure. Figure 5.1.2.1b shows the optical transmittance spectra of NiO films with different oxygen partial pressures. The 10 mT-prepared 30 nm-thick NiO demonstrated ~95% in transmittance of the bare ITO substrate over broad spectral range. The 200 mT-prepared NiO demonstrated a slightly lower transmittance compared to the 10 mT sample because of the close-packed and thick (~150 nm) film. Nevertheless, the transmittance values gradually increased with the increase of oxygen pressure for the same thickness condition. It was because the dense morphology of the film became more porous with increasing oxygen partial pressure. As a consequence, regardless of porosity (oxygen partial pressure), the prepared NiO films had a sufficient optical transparency for hole transporting layer in the photovoltaic device.

Figure 5.1.2.2 shows the X-ray diffraction (XRD) patterns of the prepared NiO films. The two main peaks appeared at 2θ value of $\sim 37.2^\circ$ and $\sim 43.2^\circ$ were assigned to planes (111) and (200) of a typical cubic structure of NiO, respectively. This implies the formation of crystallized NiO films at the oxygen pressure range of 200 - 900 mT after the post-annealing process at a

temperature of 200 °C. At 10 mT, no diffraction peak for NiO was observed owing to their low thickness and low crystallinity. Interestingly, as shown in the magnified XRD patterns, the two peaks had an opposite tendency in intensity depending on the oxygen partial pressure. At 200 mT, a relatively high diffraction of the (111) peak was demonstrated, whereas a weak intensity of the (200) peak was found. However, as the oxygen pressure increased, the intensity of the (111) peak decreased and the intensity of the (200) peak increased; the intensity ratio of the (111)/(200) peaks was 5.63, 1.52, and 1.24 for the samples processed at pressures of 200, 500 and 900 mT, respectively. Such diffraction patterns indicate that the low oxygen pressure conditions (200 mT) induced the formation of oriented NiO along the (111) plane direction during growth. In contrast, the crystallinity and the degree of preferred orientation decreased with the higher oxygen pressure conditions (500 - 900 mT). This was reflected by the loosely packed and less-ordered microstructure of 900 mT NiO film, which demonstrated in the cross sectional FESEM images in Figure 5.1.2.1a. In order to analyze the defect chemistry the prepared NiO film, their chemical states were investigated by X-ray photoelectron spectroscopy (XPS) as shown in Figure 5.1.2.3a and b. The XPS spectra shown in Figure 5.1.2.3a indicate the Ni 2p_{3/2} spectra. The peak obtained at ~854 eV and 861.3 eV in the spectra refers to the Ni²⁺ in the Ni-O octahedral bonding configuration in rock-salt NiO structure and the peak at ~856 eV refers to the Ni³⁺ peak, which implies the Ni²⁺ vacancy (metal deficiency) or oxygen excess. The Ni³⁺ are produced through Ni²⁺ to remain the electrical neutrality in the crystal. As shown in the normalized spectra, the

intensity ratio of $\text{Ni}^{3+}/\text{Ni}^{2+}$ increased with the increased oxygen pressure from 10 mT to 200 mT and maintained with further increase of oxygen pressure. This result indicates that the NiO films synthesized at higher oxygen pressure (over 200mT) contain more Ni^{2+} vacancy (or oxygen excess), which is the origin of p-type semiconducting property of NiO. On the other hand, the films synthesized at the range of 200 - 900 mT showed similar $\text{Ni}^{3+}/\text{Ni}^{2+}$ ratio, implying that the defect concentration of the films were similar to each other at the pressure over 200 mT. This tendency was verified by the O 1s XPS spectra, which shown in Figure 5.1.2.3b. The XPS results reveals that the chemical states of the NiO films were significantly influenced by the oxygen partial pressure at the low oxygen pressure range but sufficiently high oxygen pressure over 200 mT give no influence on the chemical states or p-type characteristics of the NiO films.

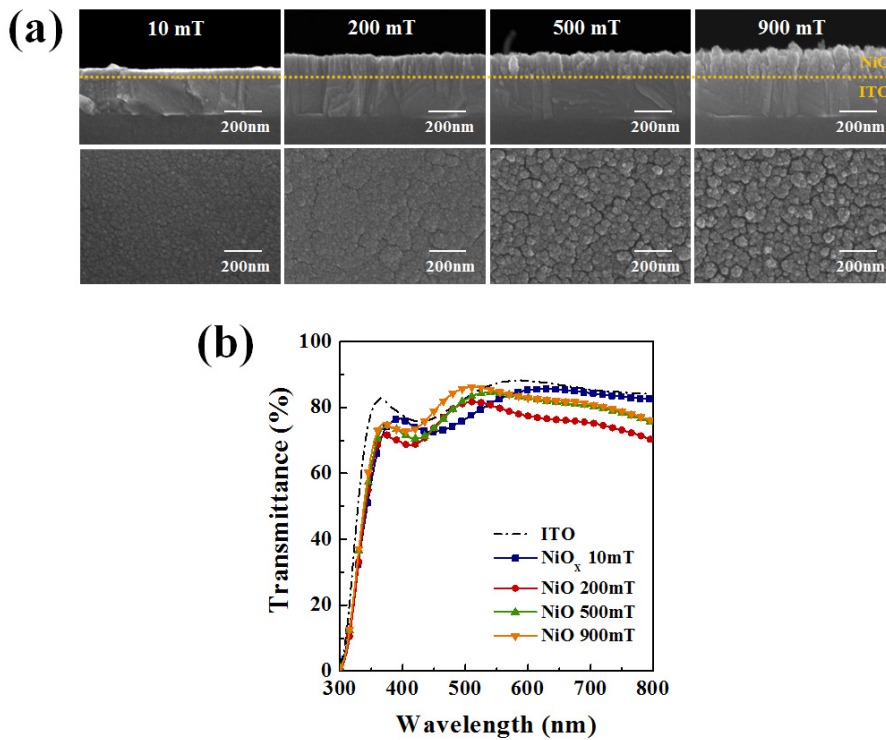


Figure 5.1.2.1 Characterization of the NiO films prepared by pulsed laser deposition (PLD) method at different oxygen partial pressures. (a) Cross-sectional and plane-view field emission scanning electron microscopy (FESEM) images and (b) transmittance spectra of the NiO films. All the prepared films were deposited on glass/tin doped indium oxide (ITO) substrates.

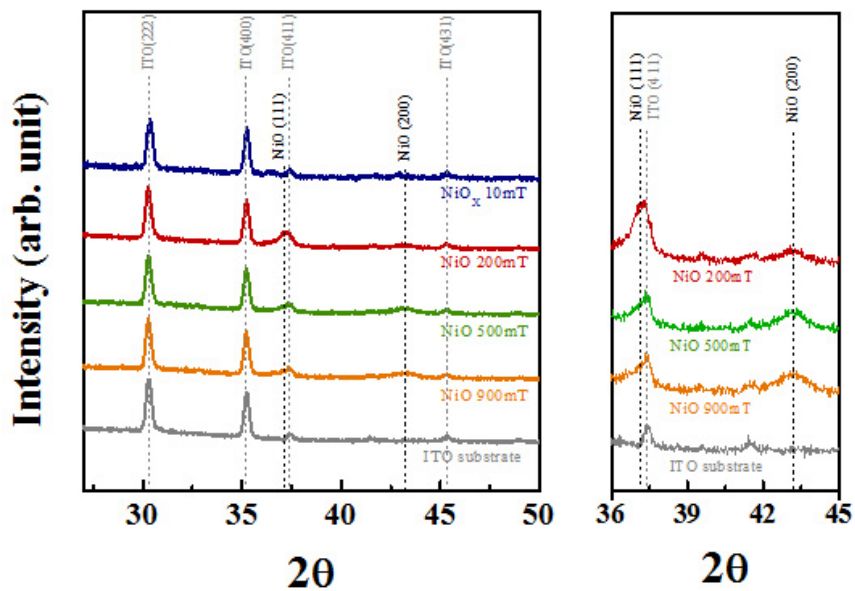


Figure 5.1.2.2 High resolution X-ray diffraction (HR-XRD) patterns of NiO films synthesized by PLD as a function of oxygen partial pressure.

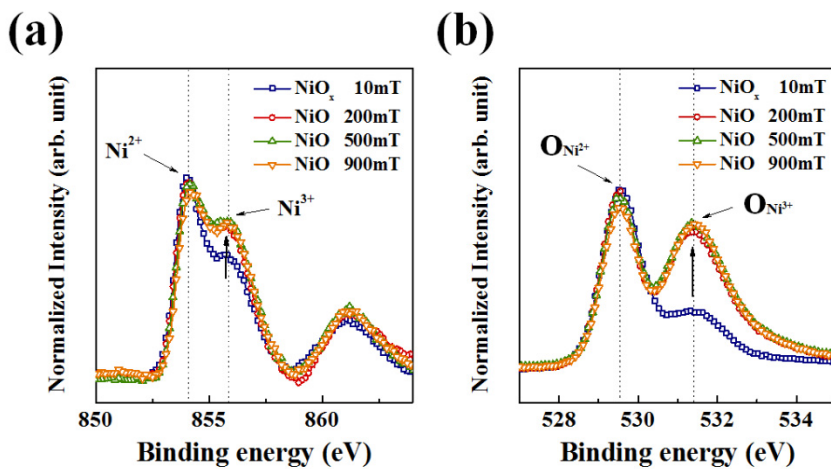


Figure 5.1.2.3 Normalized X-ray photoelectron spectroscopy (XPS) spectra of (a) Ni 2p_{3/2} and (b) O 1s peaks obtained for prepared NiO films.

5.1.3 Photovoltaic Performances of Perovskite Solar Cells Based on NiO as Hole Collecting Layer

Figure 5.1.3.1a and b depicts the XRD patterns of glass/ITO/NiO/MAPbI₃ multilayered film and an energy level diagram of each layer in the device. The XRD patterns reveals that the MAPbI₃ light absorbing layer was successfully coated on the NiO films. Figure 5.1.3.1c shows a typical cross-sectional FESEM image of a perovskite device. First, the NiO layer was prepared on top of the glass/ITO substrate through PLD under different oxygen partial pressures and deposition time. Second, a uniform and dense MAPbI₃ film (with a thickness of 300 - 350 nm) was deposited on the ITO/NiO substrate by a previously reported solvent-engineering technique, which followed by the deposition of a thin PCBM layer via spin-coating. [5.15, 5.16] Finally, the device structure was completed by vapor-depositing lithium fluoride (LiF) and the aluminum (Al) cathode. Each layer of the device is tinted with a different color. The PLD-NiO film was uniformly deposited on the glass/ITO substrate within the entire range of the active area. From the energy level diagram in Figure 5.1.3.1b, the dissociated carriers (electron and hole) in the MAPbI₃ perovskite can be extracted and transferred to the PCBM (~55 nm) and NiO (~100 nm) layer, respectively, toward each electrode. NiO has a deep valence band of -5.2 eV which is similar to that (-5.43 eV) of MAPbI₃, [5.22 – 5.24, 5.29] so a suitable (quasi-) ohmic contact could be made. In particular, such a thick NiO layer is also able to prevent electron leakage efficiently

because of the sufficiently high conduction band offset between NiO (-1.8 eV) and MAPbI₃ (-3.93 eV). [5.22 – 5.24]

To investigate the effect of NiO films with different oxygen partial pressures on the photovoltaic performance, the photocurrent density-voltage (*J-V*) characteristics of the PLD-NiO/MAPbI₃/PCBM heterojunction cells were demonstrated, which are shown in Figure 5.1.3.2. Their device parameters are summarized in Table 5.1.3.1. As mentioned above, the thickness of the PLD-NiO films was fixed to ~150 nm, except for the thin film which was prepared at 10 mT. For the thin NiO film, the optimum thickness was found to be 30 nm with the adjusted deposition time (see Figure 5.1.3.3 and Table 5.1.3.2). The resulting device demonstrates a J_{sc} of 18.6 mA·cm⁻², a V_{oc} of 0.977 V, a FF of 65%, and a PCE of 11.8%. This implies that the PLD-prepared thin NiO film worked well as HTL because of the high optical transparency and the sufficient energy level for hole extraction. However, the FF was still low, which could be attributed to the relatively low shunt resistance (R_{sh}) from the thin layer (~30 nm). For sufficient electron-blocking, the other NiO films should be thicker with a higher oxygen partial pressure. As expected, the NiO layers prepared at the oxygen partial pressure range over 200 mT showed significant enhancement in the V_{oc} and FF value compared to the 10 mT-sample. The V_{oc} value increased from 0.98 to 1.07 V with the increase of oxygen pressure to 200 mT, maintained for the sample prepared at 500 mT, and then showed slight decrease for the sample prepared at 900 mT (1.05 V). Similarly, the FF also increased from 65 to 77 % when oxygen pressure increases to 200 mT, and showed steady decrement with the

further increase of oxygen partial pressure. The improved V_{oc} and FF compared to the 10 mT-sample were mainly attributed to the increased thickness of the films, which also corresponds well with the enhanced R_{sh} shown in Table 5.1.3.1. Meanwhile, the gradual deterioration of V_{oc} , FF and also J_{sc} (17.7 to 16.1, 15.8 $\text{mA}\cdot\text{cm}^{-2}$) for the 500 and 900 mT-prepared NiO were due to the decreased charge extraction property owing to their loosely-packed and less-ordered microstructure of the NiO film containing a large number of microcracks and voids. These results were supported by the dark currents and the electron lifetime of devices based on NiO films, which described in detail below. Consequently, the highest device performance was achieved with the 200mT-film employing unique column-shaped morphology, where a J_{sc} of 17.7 $\text{mA}\cdot\text{cm}^{-2}$, a V_{oc} of 1.07 V, a FF of 77%, and an overall PCE of 14.4% were achieved.

In order to investigate the hole extraction property as a function of NiO morphology, the dark currents and electron lifetime of devices based on different NiO films were measured. Figure 5.1.3.4a demonstrates the dark J - V curve in relation to the oxygen partial pressure. For further explanation of the effect of the morphology and growth on the performance of the device, schematic illustrations of NiO with different architectures are presented in Figure 5.1.3.5. The NiO films were prepared under oxygen partial pressures of 10 mT, 200 mT, and 900 mT and were denoted as “thin” (densely-packed), “nanostructured” and “disordered” (high porosity) films, respectively. As compared with the “thin (10 mT)” film, the onsets of the dark currents of both “nanostructured (200 mT)” and “disordered (900 mT)” film were shifted to a

higher bias voltage. This result confirms the improved electron blocking property with the thicker thickness of the films from 30 nm to 150 nm. This order also correlates with their values of V_{oc} and shunt resistance in Table 5.1.3.1. Compared to the “nanostructured” film, the “disordered” film showed a higher dark current due to its loosely-packed porous microstructure, thereby causing an insufficient electron blocking/hole extraction property. Additionally in the previous reports, it is reported that the (111) oriented NiO demonstrated lower resistivity and sheet resistance compare to other growth directions, [5.30, 5.31] indicating that the (111)-preferred orientation of the “nanostructured” film may also affected the hole extraction and prevention of electron leakage at the interface between the ITO and perovskite. The effect of the morphology of the NiO film on the device performance was further examined by the transient photovoltage decay curves of devices containing “thin (10 mT)”, “nanostructured (200 mT)” and “disordered (900 mT)” NiO films, as shown in Figure 5.1.3.4b. The transient photovoltage decay experiment was performed to measure the recombination lifetime (τ_n) of each device. The τ_n of the devices were measured as a function of the light intensity. The recombination lifetime of all the samples decreased with the increase in light intensity (which can lead to a higher V_{oc}). This was mainly as a result of the increased recombination, since the concentration of carriers increased at a higher light intensity. [5.32, 5.33] As shown in Figure 5.1.3.4b, the τ_n value for the “nanostructured” NiO-based device was almost four times the τ_n value obtained for the “thin” and “disordered” samples for the entire V_{oc} range, indicating that the “nanostructured” film had a much slower recombination

rate than the other devices. The “thin” and “disordered” films demonstrated similar recombination rates. As a result of the dark current curve and the transient photovoltage decay curve, it could be confirmed that the “nanostructured” NiO film performed efficient electron blocking (suppresses recombination) and hole extraction, leading to the enhanced FF and PCE values of the device. In addition, XRD patterns and FESEM images of MAPbI₃ layers coated on the different NiO films in Figure 5.1.3.6 reveals that the crystalline phase and morphology of MAPbI₃ layer were almost the same to each other, regardless of NiO morphology.

To gain further insight into the effect of the thickness of the “nanostructured” NiO film (which was prepared at 200 mT) on the performance of the device, hybrid perovskite solar cells of MAPbI₃-PCBM (under the same conditions) were fabricated with different NiO film thicknesses. This was performed by adjusting the deposition time of NiO film; the thicknesses obtained for the films were 100, 180, 250, and 340 nm, as shown in the cross-section FESEM images in Figure 5.1.3.7a. The *J-V* curves of the device, in relation to the thickness of the NiO film, are given in Figure 5.1.3.7b. All the relevant parameters are also summarized in Table 5.1.3.3. Irrespective of the thickness of NiO films, all the samples showed a high V_{oc} of 1.03 - 1.08 V, which was superior to that of typical PEDOT:PSS-used p-i-n cells. The most notable observation was the dramatic reduction of J_{sc} (from 19.2 to 14.3 mA·cm⁻²) as the increase of the thickness of NiO films. This trend was attributed to the gradually decreasing transmittance of the thicker NiO film, as demonstrated in Figure 5.1.3.7c. This assumption could also be

supported by the fact that much lower contributions (in the range of 300 and 500 nm) for the thicker NiO film were clearly observed, as compared to those observed in the longer wavelength (see the normalized EQE spectra of Figure 5.1.3.7d). Contrastingly, the FF value was enhanced in the higher thickness, achieving high FF values of 80% for the films thicker than 180nm. The “nanostructured” NiO film had to be thick enough to allow a high FF value, which was ascribed to the improved shunt resistance of the device. Based on these findings, there could be a trade-off between the J_{sc} and the FF, regarding the NiO thickness. Thus, the optimal device performance was obtained with a thickness between 100 and 180 nm, where high values of both J_{sc} and FF could be achieved.

By further optimization and repetition for the fabrication of the “nanostructured” NiO-based perovskite solar cells, we could achieve the best performance, attaining a PCE of 17.3% under AM 1.5G 100 $\text{mW}\cdot\text{cm}^{-2}$ irradiation. This was achieved with the optimized NiO conditions (oxygen partial pressure of 200 mT and deposition time for a thickness between 100 and 180 nm) required for the further improvement of the cell performance. As shown in the J - V curve in Figure 5.1.3.8a, the relevant device parameters are a J_{sc} of 20.2 $\text{mA}\cdot\text{cm}^{-2}$, a V_{oc} of 1.06 V, and a FF of 81.3%. The integrated current density (19.6 $\text{mA}\cdot\text{cm}^{-2}$) derived from the EQE spectra in Figure 5.1.3.8b corresponds well with the measured value under simulated sunlight. In particular, our device exhibited a markedly higher FF (81.3%), in comparison to some devices with other HTMs (such as PEDOT:PSS, PEDOT:PSS/poly (N,N'-bis(4-butylphenyl)-N,N'-bis(phenyl)benzidine(poly-

TPD), PEDOT:PSS + Perfluorinated ionomer (PFI), electrodeposited poly (3-hexylthiophene) (P3HT), graphene oxide, thin NiO_x, mesoscopic NiO, Cu:NiO_x and NiO/meso-Al₂O₃) reported elsewhere. [5.17 – 5.26, 5.34 – 5.41]

Consequently, this result indicates that our “nanostructured” NiO film with a unique morphology and a preferred orientation satisfies the prerequisite for a desirable hole-transporting layer. This may be a key factor for achieving high FF and favorable PCE in MAPbI₃-PCBM device. Furthermore, the PCE of 17.3% obtained in our best cell seems reliable, considering that it was obtained from the steady-state photocurrent density near the maximum power point; as an initial value, the steady state efficiency of 17.2% was stabilized to reach 16.9% after 100 s, as displayed in Figure 5.1.3.9. In addition, *J-V* curves of 200 mT-based perovskite device under reverse and forward scan direction and various scan rates are displayed in Figure 5.1.3.10.

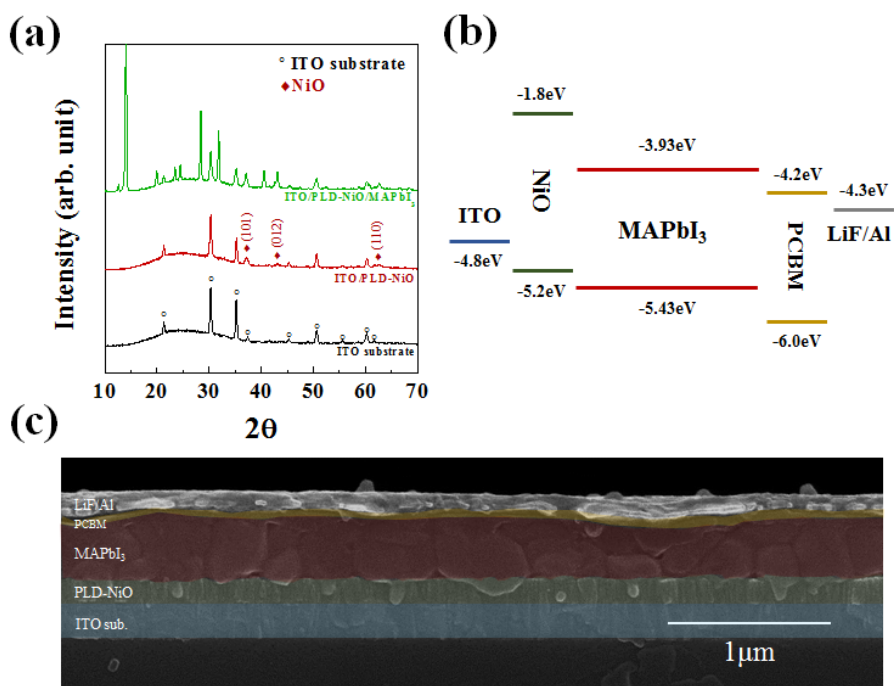


Figure 5.1.3.1 (a) XRD patterns of glass/ITO/NiO/methyl-ammonium lead iodide (MAPbI₃) multi-layered film and (b) the diagram of the device configuration and energy levels of each layer. (c) FESEM images showing the complete device structure. The various layers are tinted with different colors.

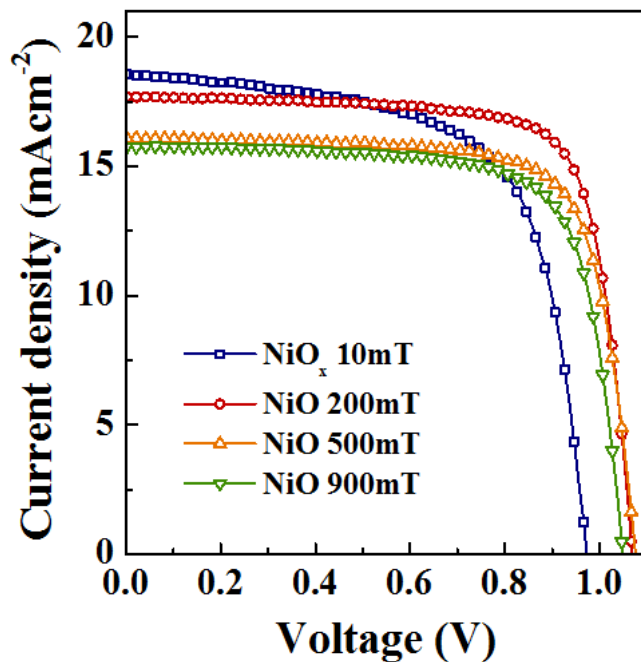


Figure 5.1.3.2 The photocurrent density-voltage (J - V) curves of perovskite solar cells based on PLD-NiO films, deposited at various oxygen partial pressures. The thickness for the NiO_x and PLD-NiO films were 30 nm and 150 ± 20 nm, respectively.

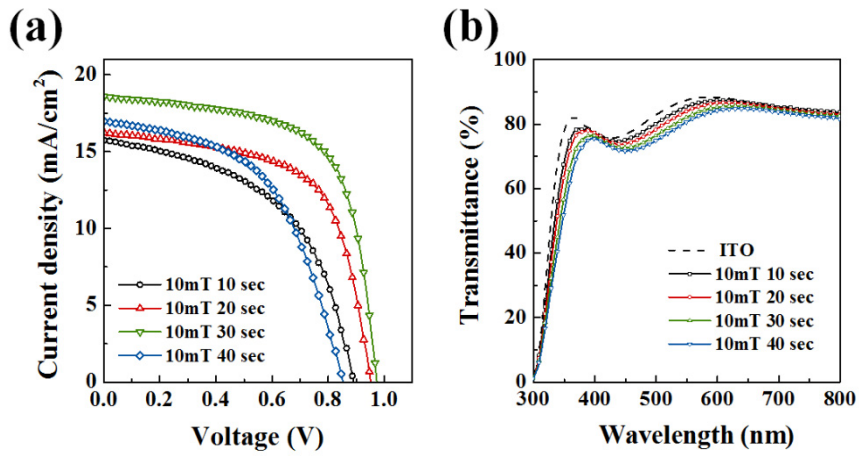


Figure 5.1.3.3 (a) J - V curves of perovskite solar cells based on dense NiO_x films with different deposition time (thickness). (b) The transmittance spectra of NiO_x films as a function of deposition time.

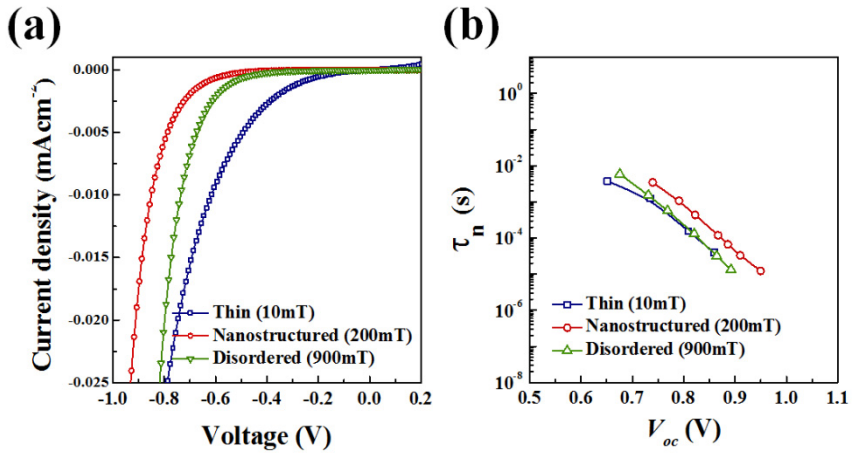


Figure 5.1.3.4 (a) Dark currents and (b) the recombination lifetime of the devices based on thin, nanostructured and disordered NiO layers. The thin, nanostructured and disordered NiO films were prepared at oxygen partial pressures of 10, 200 and 900 mT, respectively.

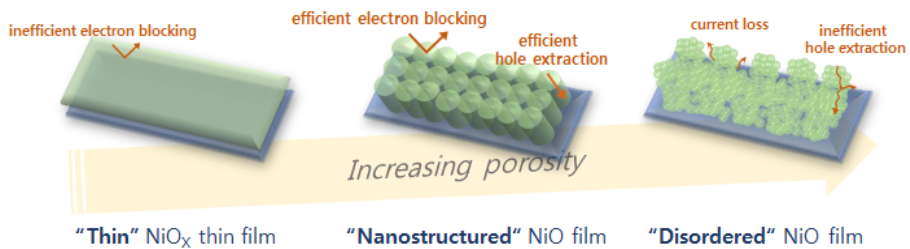


Figure 5.1.3.5 Effect of the morphology and growth of the PLD-NiO films as a hole transporting layer, on the solar cell performance. Schematic images of thin, nanostructured and disordered NiO films fabricated using PLD as an electron blocking layer/hole extraction layer in the NiO/MAPbI₃/PCBM heterojunction solar cells.

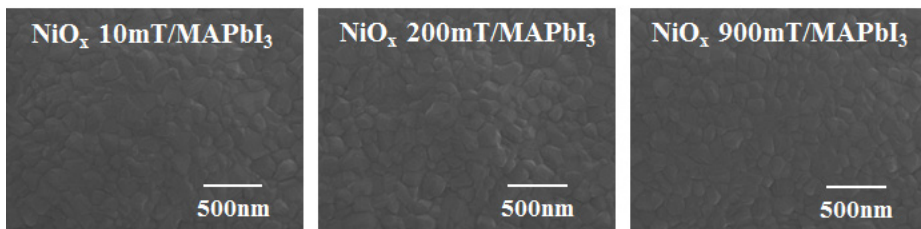
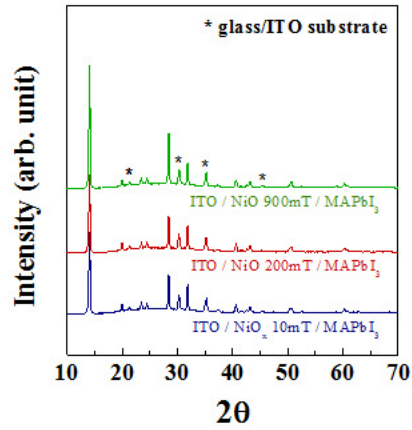


Figure 5.1.3.6 XRD patterns and plane-view FESEM images of MAPbI₃ layers coated on the NiO films synthesized at 10, 200 and 900 mT, respectively.

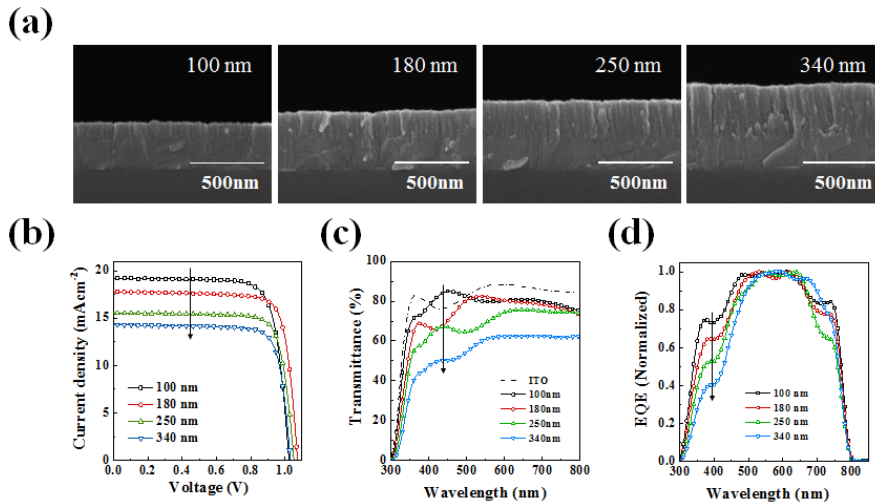


Figure 5.1.3.7 (a) Cross-sectional FESEM images of PLD-NiO films deposited at the oxygen partial pressures of 200 mT with the thickness of 100, 180, 250, 340 nm. (b) J - V characteristics of PLD-NiO based perovskite solar cells with different NiO layer thickness, measured under simulated AM 1.5 $100 \text{ mW} \cdot \text{cm}^{-2}$ sunlight. (c) The transmittance spectra of PLD-NiO films and (d) the normalized external quantum efficiency (EQE) spectra of prepared solar cells as a function of film thickness.

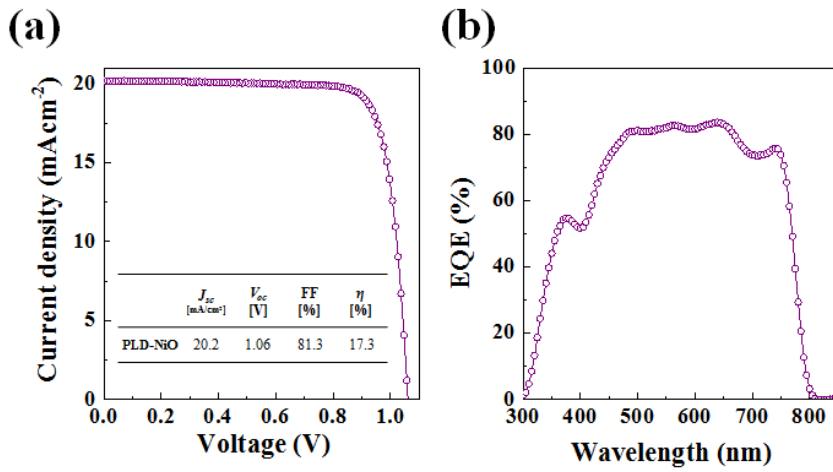


Figure 5.1.3.8 (a) J - V curves and (b) EQE spectra for the best cell using nanostructured NiO film with a thickness of 150 nm. The photovoltaic parameters of the best cell are shown in the inset table.

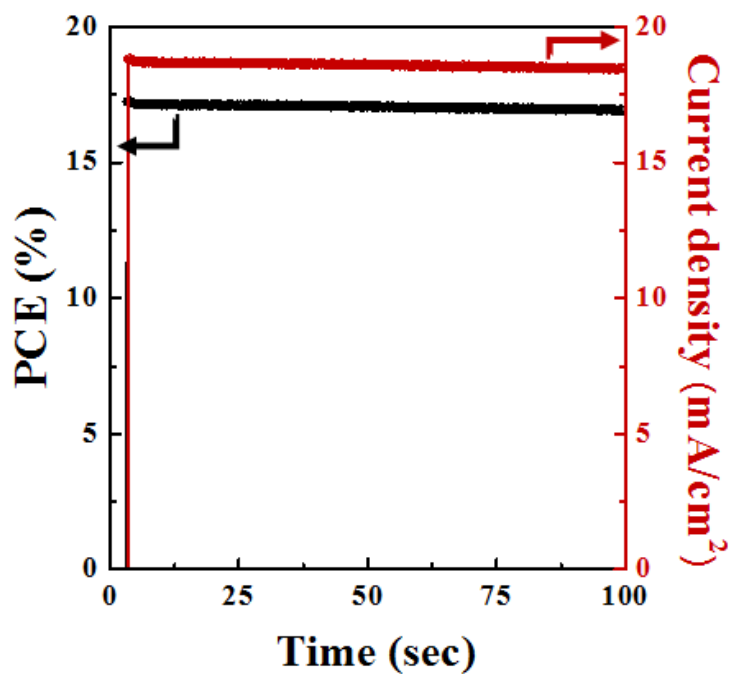


Figure 5.1.3.9 Steady-state current density measured at a maximum power point (0.906V) of the champion cell and its stabilized power output.

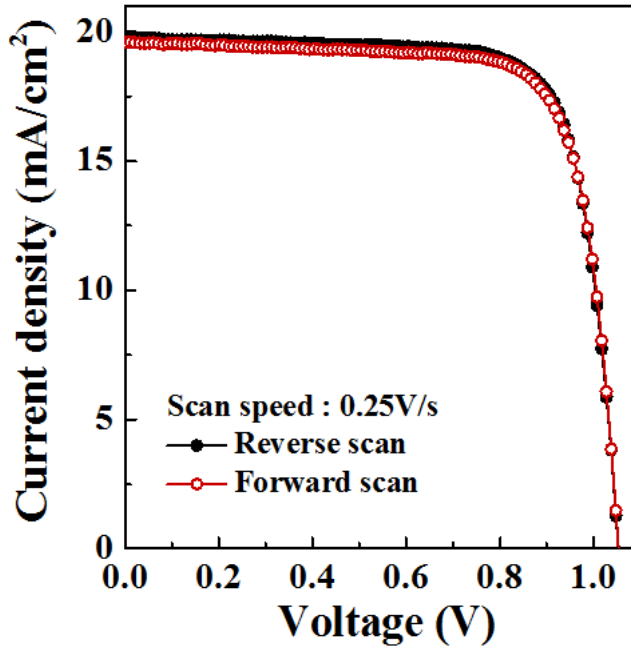


Figure 5.1.3.10 *J-V* curves of 200 mT-NiO based device under reverse (from V_{oc} to J_{sc}) and forward (from J_{sc} to V_{oc}) scan directions. The scan speed was 0.25 V/s.

Table 5.1.3.1 Photovoltaic parameters of PLD-NiO based perovskite solar cells as a function of oxygen partial pressure.

Oxygen Pressure [mTorr]	J_{sc} [mA cm ⁻²]	V_{oc} [V]	FF [%]	η [%]	R_{sh} [Ω cm ²]	R_s [Ω cm ²]
10	18.6	0.98	65	11.8	0.6k	5.5
200	17.7	1.07	77	14.4	7.8k	5.1
500	16.1	1.08	75	13.0	4.1k	5.0
900	15.8	1.05	74	12.3	1.7k	5.0

Table 5.1.3.2 Photovoltaic parameters of perovskite solar cells using dense NiO_x films with different deposition time (thickness).

NiO 10 mT Deposition Time [sec]	J_{sc} [mA cm ⁻²]	V_{oc} [V]	FF [%]	η [%]
10	15.7	0.887	51	7.2
20	16.2	0.947	63	9.6
30	18.6	0.977	65	11.8
40	17.0	0.856	52	7.6

Table 5.1.3.3 Photovoltaic parameters of PLD-NiO based perovskite solar cells as a function of film thickness.

Film Thickness [nm]	J_{sc} [mA cm ⁻²]	V_{oc} [V]	FF [%]	η [%]	R_{sh} [Ω cm ²]	R_s [Ω cm ²]
100	19.2	1.03	78	15.3	3.5k	3.8
180	17.8	1.08	80	15.3	14.5k	3.4
250	15.6	1.05	80	13.0	14.2k	4.5
340	14.3	1.03	80	11.8	5.2k	4.5

5.1.4 Conclusion

In summary, we have prepared highly transparent, nanostructured NiO films through PLD, by controlling the oxygen partial pressure and the deposition time. The photovoltaic performance was explored using PLD-prepared NiO films from a p-i-n type device of a NiO/MAPbI₃/PCBM configuration. The best-performing device exhibited a remarkable efficiency of 17.3% with a very high FF of 81.3%. The enhanced performance in a nanostructured NiO film was attributed to the slow recombination rate during the extraction and transport of the dissociated carriers. As a result, the (111)-oriented nanostructured NiO film with good optical transparency played a key role in the efficient extraction of holes and the prevention of electron leakage as an HTL in a perovskite solar cell. We expect that this nanostructured NiO film will be competitive with high-performing MAPbI₃-based n-i-p solar cells and an ideal candidate for the HTL in the p-i-n perovskite solar cell system.

5.1.5 Bibliography

- [5.1] K. Liang, D. B. Mitzi and M. T. Prikas, *Chem. Mater.* **1998**, 10, 403.
- [5.2] A. Kojima, K. Teshima, Y. Shirai and T. Miyasaka, *J. Am. Chem. Soc.* **2009**, 131, 6050.
- [5.3] J. H. Im, C. R. Lee, J. W. Lee, S. W. Park and N. G. Park *Nanoscale* **2011**, 3, 4088.
- [5.4] L. Etgar, P. Gao, Z. Xue, Q. Peng, A. K. Chandiran, B. Liu, M. K. Nazeeruddin and M. Grätzel *J. Am. Chem. Soc.* **2012**, 134, 17396.
- [5.5] M. M. Lee, J. Teuscher, T. Miyasaka, T. N. Murakami and H. J. Snaith, *Science* **2012**, 338, 643.
- [5.6] H. S. Kim, C. R. Lee, J. H. Im, K. B. Lee, T. Moehl, A. Marchioro, S. J. Moon, R. Humphry-Baker, J. H. Yum, J. E. Moser, M. Grätzel and N. G. Park, *Sci. Rep.* **2012**, 2, 1.
- [5.7] J. H. Noh, S. H. Im, J. H. Heo, T. N. Mandal and S. I. Seok, *Nano Lett.* **2013**, 13, 1764.
- [5.8] J. H. Heo, S. H. Im, J. H. Noh, T. N. Mandal, C. S. Lim, J. A. Chang, Y. H. Lee, H. Kim, A. Sarkar, M. K. Nazeeruddin, M. Grätzel and S. I. Seok, *Nat. Photon.* **2013**, 7, 486.
- [5.9] J. Burschka, N. Pellet, S. J. Moon, R. Humphry-Baker, P. Gao, M. K. Nazeeruddin and M. Grätzel, *Nature* **2013**, 499, 316.
- [5.10] M. Liu, M. B. Johnston and H. J. Snaith, *Nature* **2013**, 501, 395.

- [5.11] S. Ryu, J. H. Noh, N. J. Jeon, Y. C. Kim, W. S. Yang, J. Seo and S. I. Seok, *Energy Environ. Sci.* **2014**, 7, 2614.
- [5.12] G. Xing, N. Mathews, S. Sun, S. S. Lim, Y. M. Lam, M. Grätzel, S. Mhaisalkar and T. C. Sum, *Science* **2013**, 342, 344.
- [5.13] N. J. Jeon, H. G. Lee, Y. C. Kim, J. Seo, J. H. Noh, J. Lee, S. I. Seok, *J. Am. Chem. Soc.* **2014**, 136, 7837.
- [5.14] G. E. Eperon, S. D. Stranks, C. Menelaou, M. B. Johnston, L. M. Herza and H. J. Snaith, *Energy Environ. Sci.* **2014**, 7, 982.
- [5.15] N. J. Jeon, J. H. Noh, Y. C. Kim, W. S. Yang, S. Ryu and S. I. Seok, *Nat. Mater.* **2014**, 13, 897.
- [5.16] J. Seo, S. Park, Y. C. Kim, N. J. Jeon, J. H. Noh, S. C. Yoon and S. I. Seok, *Energy Environ. Sci.* **2014**, 7, 2642.
- [5.17] R. Betancur, M. Maymo, X. Elias, L. T. Vuong and J. Martorell, *Sol. Energy Mater. Sol. Cells* **2011**, 95, 735.
- [5.18] J. R. Manders, S. W. Tsang, M. J. Hartel, T. H. Lai, S. Chen, C. M. Am, J. R. Reynolds and F. So1, *Adv. Funct. Mater.* **2013**, 23, 2993.
- [5.19] M. D. Irwin, D. B. Buchholz, A. W. Hains, R. P. H. Chang and T. J. Marks, *PNAS* **2008**, 105, 2783.
- [5.20] L. Li, E. A. Gibson, P. Qin, G. Boschloo, M. Gorlov, A. Hagfeldt and L. Sun, *Adv. Mater.* **2010**, 22, 1759.
- [5.21] T. Ripolles-Sanchisa, A. Guerreroa, E. Azacetab, R. Tena-Zaerab and G. Garcia-Belmontea, *Sol. Energy Mater. Sol. Cells* **2013**, 17, 564.

- [5.22] J. Y. Jeng, K. C. Chen, T. Y. Chiang, P. Y. Lin, T. D. Tsai, Y. C. Chang, T. F. Guo, P. Chen, T. C. Wen and Y. J. Hsu, *Adv. Mater.* **2014**, 26, 4107.
- [5.23] K. C. Wang, J. Y. Jeng, P. S. Shen, Y. C. Chang, E. W. Diau, C. H. Tsai, T. Y. Chao, H. C. Hsu, P. Y. Lin, P. Chen, T. F. Guo and T. C. Wen *Sci. Rep.* **2014**, 4, 4756.
- [5.24] K. C. Wang, P. S. Shen, M. H. Li, S. Chen, M. W. Lin, P. Chen and T. F. Guo, *ACS Appl. Mater. Interfaces* **2014**, 6, 11851.
- [5.25] J. H. Kim, P. W. Liang, S. T. Williams, N. Cho, C. C. Chueh, M. S. Glaz, D. S. Ginger and A. K. Jen, *Adv. Mater.* **2015**, 27, 695.
- [5.26] W. Chen, Y. Wu, J. Liu, C. Qin, X. Yang, A. Islam, Y. B. Cheng and L. Han, *Energy Environ. Sci.* **2015**, 8, 629.
- [5.27] J. H. Noh, J. H. Park, H. S. Han, D. H. Kim, B. S. Han, S. Lee, J. Y. Kim, H. S. Jung and K. S. Hong *J. Phys. Chem. C* **2012**, 116, 8102.
- [5.28] J. H. Park, D. H. Kim, S. S. Shin, H. S. Han, M. H. Lee, H. S. Jung, J. H. Noh and K. S. Hong *Adv. Energy Mater.* **2014**, 4, 1300395.
- [5.29] A. S. Subbiah, A. Halder, S. Ghosh, N. Mahuli, G. Hodes and S. K. Sarkar *J. Phys. Chem. Lett.* **2014**, 5, 1748.
- [5.30] H. L. Chen and Y. S. Yang, *Thin Solid Films* **2008**, 516, 5590.
- [5.31] N. Talebiana and M. Kheiri, *Solid State Sciences* **2014**, 27, 79.
- [5.32] D. Bi, L. Yang, G. Boschloo, A. Hagfeldt and E. M. J. Johansson, *J. Phys. Chem. Lett.* **2013**, 4, 1532.

- [5.33] D. Bi, S. J. Moon, L. Häggman, G. Boschloo, L. Yang, E. M. J. Johansson, M. K. Nazeeruddin, M. Grätzel and A. Hagfeldt *RSC Adv.* **2013**, 3, 18762.
- [5.34] O. Malinkiewicz, A. Yella, Y. H. Lee, G. M. Espallargas, M. Grätzel, M. K. Nazeeruddin and H. J. Bolink *Nat. Photonics* **2014**, 8, 128.
- [5.35] K. G. Lim, H. B. Kim, J. Jeong, H. Kim, J. Y. Kim and T. W. Lee *Adv. Mater.* **2014**, 26, 6461.
- [5.36] L. M. Chen, Z. Xu, Z. Hong and Y. Yang *J. Mater. Chem.* **2010**, 20, 2575.
- [5.37] Q. Wang, Y. Shao, Q. Dong, Z. Xiao, Y. Yuan and J. Huang *Energy Environ. Sci.* **2014**, 7, 2359.
- [5.38] Z. Wu, S. Bai, J. Xiang, Z. Yuan, Y. Yang, W. Cui, X. Gao, Z. Liu, Y. Jin and B. Sun *Nanoscale* **2014**, 6, 10505.
- [5.39] W. Yan, Y. Li, W. Sun, H. Peng, S. Ye, Z. Liu, Z. Bian and C. Huang *RSC adv.* **2014**, 4, 33039.
- [5.40] Z. Xiao, Q. Dong, C. Bi, Y. Shao, Y. Yuan and J. Huang, *Adv. Mater.* **2014**, 26, 6503.
- [5.41] J. You, Z. Hong, Y. Yang, Q. Chen, M. Cai, T. B. Song, C. C. Chen, S. Lu, Y. Liu, H. Zhou and Y. Yang *ACS Nano* **2014**, 8, 1674.

Chapter 6. Conclusion

Nanostructured transparent n-type and p-type semiconducting oxides were synthesized and explored in terms of structural and compositional optimization and design to create a fundamental understanding of charge collecting properties for enhancing energy conversion efficiency in emerging photovoltaics (PVs) such as inorganic semiconductor sensitized solar cells (ISSCs) and organic-inorganic hybrid perovskite solar cells (PSCs).

First, structural design for n-type titanium dioxide (TiO_2) semiconducting oxides was proposed in photovoltaic energy conversion system. TiO_2 semiconducting oxides were synthesized in a form of hierarchically organized architecture by pulsed laser deposition (PLD) system. Unlike the conventional TiO_2 nanoparticle film, this architecture contained a large specific surface area and open channels of pores as well. The morphology of the TiO_2 architecture can be easily controlled by adjusting the kinetic energy of the ablated species, which can be controlled by the deposition parameters such as oxygen partial pressures during the process. As a result, TiO_2 architectures having various morphologies were successfully synthesized. The architecture deposited at a low oxygen pressures led to a dense film with no open channels. As the oxygen pressures increase, the architectures were formed into films having high porosity with open channels, but the volume portion of TiO_2 on the film seemed to get lower compared to the films prepared at lower oxygen pressures.

The architectures deposited between 100mTorr and 200mTorr were expected to have both sufficient open channels of pores and volume portion of TiO₂. In order to examine the morphology effect of the TiO₂ photoelectrodes on the photovoltaic performance, CdS/CdSe-sensitized solar cells (CSSCs) based on prepared TiO₂ photoelectrodes were fabricated. CdS and CdSe inorganic light absorbers were adsorbed onto the TiO₂ by Successive Ionic Layer Adsorption and Reaction (SILAR) method. The morphology of the architectures significantly influenced the cell performances. The CSSC based on 150 mT-TiO₂ photoelectrode showed the highest cell performance which attributed to both sufficient volume portion of TiO₂ and open channels of pores. For the TiO₂ films deposited at lower oxygen pressures than 150 mT showed relatively low fill factor (FF) due to the insufficient open channels of pores, whereas the films deposited at higher oxygen pressures showed high FF due to the sufficient pores, but showed low short-circuit currents (J_{sc}) due to the lack of TiO₂ volume portion. Compared to the conventional TiO₂ nanoparticle films (denoted as NP-TiO₂), TiO₂ prepared by PLD at 150mTorr (denoted as PLD-TiO₂) showed remarkable cell performances. The energy conversion efficiency of 5.57% obtained by PLD-TiO₂ was approximately 46% higher than that of NP-TiO₂ photoelectrode (3.84%). The origin of enhanced efficiency was the improved J_{sc} and FF values, which attributed to the enhanced light harvesting and charge collecting properties. The higher light harvesting property of PLD-TiO₂ architecture was confirmed by the inductively coupled plasma (ICP) analysis and the Brunauer-Emmett-Teller (BET) measurement, which clearly showed that the PLD-TiO₂ had larger

surface area than the NP-TiO₂ resulting in the larger amount of adsorbed CdS and CdSe. Additionally, owing to the enhanced adhesion property compared to NP-TiO₂, the PLD-TiO₂ can accomplish more SILAR cycles, resulting in the improvement of J_{sc} . The improved charge collecting property of PLD-TiO₂ was due to the existence of the open channels of pores. For the investigation of charge collecting property, intensity-modulated photocurrent/voltage spectroscopy (IMPS/IMVS) and electrochemical impedance spectroscopy (EIS) analysis were done. IMPS and IMVS measurements showed that PLD-TiO₂ architecture had longer electron lifetime by fivefold compared to the NP-TiO₂. The open channels of pores in the PLD-TiO₂ architecture assisted the infiltration of the SILAR solution as well as polysulfide electrolyte solution, which led to better coverage of the CdS/CdSe on the surface of TiO₂ and improvement of Sn²⁺ ion diffusion to the counter electrode. The better coverage of CdS/CdSe and improved ion diffusion of electrolyte suppressed the recombination process. The reduced resistance which related to the Nernst diffusion of polysulfide electrolyte measured by the EIS analysis also indicates the effective ionic conduction of the polysulfide electrolyte inside the PLD-TiO₂ photoelectrode.

Second, compositional design of semiconducting oxides was proposed for enhancing charge injection property between the inorganic light absorbing materials and electron accepting semiconductors in ISSCs. From the basis that the energy difference between the conduction band of inorganic semiconductor and TiO₂ serves as the driving force for electron injection and that the doping metal cation into TiO₂ is a commonly adopted method for

tailoring conduction band (CB) position and trap/defect level distribution in TiO_2 , we explored the influence of Niobium (Nb)-doping into TiO_2 photoelectrode in ISSCs. Using PLD system, the undoped and Nb-doped TiO_2 (NTO) films were successfully synthesized without any morphological or particle size change. The electron probe micro-analyzer (EPMA) and X-ray photoelectron spectroscopy (XPS) results revealed that the Nb dopants were successfully introduced into the TiO_2 lattice and the concentration of Nb dopants was successfully controlled. The CB edge of TiO_2 was positively shifted with Nb doping, which confirmed by the Mott-schottky plots. To investigate the effect of band engineering on the photovoltaic performances, PbS/CdS-sensitized solar cells based on prepared NTO films were fabricated. PbS and CdS inorganic light absorbers were adsorbed by SILAR method. The undoped, 0.5 at%, 1 at% and 1.5 at% Nb-doped TiO_2 films were denoted as 0NTO, 0.5NTO, 1NTO and 1.5NTO, respectively. The introduction of Nb strongly influenced the photovoltaic performances of the prepared ISSCs in all device parameters including J_{sc} , open circuit voltage (V_{oc}) and FF. Compared to the 0NTO-ISSCs, the 0.5NTO-ISSCs showed remarkable enhancement in the external quantum efficiency (EQE) and J_{sc} value. The EQE and J_{sc} value are related to the light harvesting, charge injection and charge collecting properties. Light harvesting efficiency obtained by optical properties of NTO films revealed that the light harvesting efficiencies were comparable. Also, the IMPS/IMVS analysis indicated that the charge collecting efficiency of 0NTO and 0.5NTO was comparable, which the efficiency distinction was less than 2 % at the entire range. Since both light

harvesting and charge collecting efficiencies of prepared ISSCs were comparable, it is convinced that the enhanced EQE and J_{sc} was attributed to its enhanced electron injection ability. The driving force for the electron injection, which is the energy distinction between CB edges of PbS and TiO₂, was enlarged after the fine Nb doping, resulting in the faster electron injection from PbS to NTO CB. As a consequence, the J_{sc} value of ISSCs was greatly improved by Nb doping for approximately 41 % compared to the undoped PSSC. On the other hand, the J_{sc} , V_{oc} and FF showed steady decrement with the increment of Nb concentration. The decrement of V_{oc} was due to the CB edge change of TiO₂ by Nb doping, since the V_{oc} value in solar cells corresponds to the energy difference between the quasi-Fermi level of TiO₂ and the redox potential of the electrolyte. The reduction of J_{sc} and FF was attributed to the increased dark currents. As a consequence, fine control of Nb concentration led to an enhanced electron injection efficiency and improved overall efficiency as well.

Finally, novel structure of p-type semiconducting oxide based hole transporting layer (HTL) was proposed for planar heterojunction perovskite solar cells (PSCs). Nanostructured nickel oxide (NiO) films were synthesized by PLD system. The films were prepared as thin layers having thickness less than 150 nm, since the perovskite solar cells are based on layered structures. Due to this low thickness, efficient electron blocking and hole extraction are the most important properties to achieve highly efficient planar PSCs. The morphology and thickness of NiO were also easily controlled by adjusting the deposition parameters such as oxygen partial pressures and deposition time.

At a pressure of 10 mT, densely-packed thin NiO film was obtained. As the oxygen partial pressures increased during growth, the densely packed and planar morphology became more porous and rougher. At a pressure of 200 mT, an ordered, column-shaped NiO nanostructured film was formed. In contrast, at pressures over 500 mT, the surfaces appeared relatively rough containing many voids, making the morphology similar to a typical mesoscopic structure. The optical transmittance spectra of prepared NiO films indicated that the films had sufficient optical transparency for hole transporting layer in the photovoltaic device. The X-ray diffraction (XRD) patterns revealed that different preferred orientation occurred in terms of oxygen pressures. At 200 mT, a relatively high diffraction of the (111) peak was demonstrated, whereas a weak intensity of the (200) peak was found. As the oxygen pressures increased, the intensity of the (111) peak decreased and the intensity of the (200) peak increased. Such diffraction patterns indicate that the nanostructured 200 mT-NiO induced the formation of oriented NiO along the (111) plane direction during growth. Since the (111) oriented NiO demonstrates lower resistivity and sheet resistance, the (111)-preferred orientation of the nanostructured NiO film may also have an effect on extracting holes and preventing electron leakage. In order to examine the morphology effect on the photovoltaic performance, PSCs based on prepared NiO films were fabricated. The thin NiO film (10 mT) showed an overall efficiency of 11.8% which implies that the thin NiO film worked well as an HTL due to the high optical transparency and the sufficient energy level for hole extraction. However the V_{oc} and FF was relatively low compared to other

NiO films. The nanostructured NiO films (200 mT) showed significant enhancement in device efficiency compared to the thin film due to the increased V_{oc} and FF. The improved V_{oc} and FF were mainly attributed to more efficient electron blocking, which resulted from the increased thickness of the films. Meanwhile, the gradual deterioration of V_{oc} , FF and also J_{sc} for the porous 500 and 900 mT-prepared NiO were due to the decreased charge extraction property owing to their loosely-packed and less-ordered microstructure of the NiO film containing a large number of microcracks and voids. These results were supported by the dark currents and the electron lifetime of the devices based on NiO films. The recombination lifetime (τ_n) of each devices were measured by transient photovoltage decay analysis. The τ_n value for the nanostructured NiO-based device showed approximately four times higher than that of thin and disordered films for the entire V_{oc} range, indicating that the nanostructured film had a much slower recombination rate. As a consequence, the nanostructured NiO film deposited at 200 mT performed both efficient electron blocking (suppresses recombination) and hole extraction, leading to the enhanced device performance. By further optimization, the best-performing device exhibited a high efficiency of 17.3 % with a very high FF of 81.3 %. We expect that this nanostructured NiO film will be an ideal candidate for the HTL in the p-i-n perovskite solar cell system.

Our study on structural and compositional design of n-type and p-type semiconducting oxides demonstrated the importance of a suitable form of electrode architecture for emerging PVs, especially in terms of charge collecting property. These findings will contribute to the development of

advanced semiconducting oxide electrodes and create breakthrough in photoelectric energy conversion systems.

Abstract (in Korean)

본 연구에서는 광·전 에너지 변환 장치에서의 광·전 변환 효율 개선을 위한 N형 및 P형 산화물 반도체 전극 물질의 설계 및 합성에 대한 연구를 진행하였다. 합성된 나노 구조체 산화물 반도체 전극을 광·전 변환 디바이스의 광전극으로 사용하여 이들의 구조 및 조성 제어와 이에 따른 디바이스에서의 전하 수집 능력의 상관관계에 대해 심도 있게 다루었다. 구체적으로, 경제적 측면에서 낮은 제조 단가로 인해 미래의 에너지 공급 문제와 환경 오염 문제를 동시에 해결할 수 있는 차세대 태양전지인 무기 감응형 태양 전지 (inorganic semiconductor sensitized solar cells) 및 유-무기 하이브리드 페로브스카이트 태양 전지 (organic-inorganic hybrid perovskite solar cells)에 관하여 연구를 진행하였다. 이러한 태양 전지들이 실제로 사용되기 위해서는 광·전 변환 효율 측면과 환경적 안정성 측면에서 여러 문제들을 극복해야만 한다. 이들 태양전지에서 N형 및 P형 산화물 반도체 전극 물질들은 디바이스에서 광·전 변환으로 생성된 전자 및 정공의 수집 능력 및 전체적인 효율 측면에서 필수적인 역할을 하기 때문에, 이들의 구조 및 조성을 설계 및 제어 함으로써 높은 광·전 변환 효율 및 안정성 개선을 이룰 수 있을 것이라 기대된다. 본 연구에서는 이러한 관점에서 높은 전하 수집 및 변환 효율을 위해 두 가지 전략을 제시하였다. 첫째로, 산화물 반도체 전극 물질의 구조 제어를 통하여 전자와 정공 사이의 재결합을 억제하고 효율적인 전하 수집을 이루는 것이다. 둘째로, 산화물 반도체 전극 물질의 조성 제어를 통해 광 흡수 물질과 전하

수집 물질 사이의 전하 주입 능력을 향상시켜 광·전 변환 효율을 높이는 것이다.

먼저 N형 산화물 반도체 물질인 이산화 티타늄 (TiO_2)과 P형 산화물 반도체 물질인 산화 니켈 (NiO) 전극 막의 구조 디자인에 대한 연구를 진행하였고, 이러한 구조 제어 효과와 태양 전지의 재결합 억제 및 전하 수집 능력 사이의 상관 관계를 밝혀 개선 가능성을 제시하였다. TiO_2 의 경우, 펄스 레이저 증착법 (pulsed laser deposition)을 이용하여 유리 기판 위에 계층적 구조를 갖는 나노 입자로 이루어진 나노 구조체로 합성하는 데 성공하였다. 이들의 성장 방법 및 이들의 무기 감응형 태양 전지에서 광전극으로서의 전하 수집 능력에 대해 연구하였다. 먼저 증착 조건 제어를 통해 TiO_2 막의 구조 제어에 성공하였고, 이들의 구조 제어가 태양 전지의 효율에 지대한 영향을 미친다는 것을 밝혀 내었다. 기존의 TiO_2 나노 입자 막과 비교하여 계층적 구조를 갖는 나노 구조체의 경우, 비표면적이 더 넓어 많은 양의 광흡수 물질 흡착이 가능하였고 또 기판과의 더 좋은 접촉 능력을 보여 광수확 특성이 향상되었다. 여기에 추가적으로 그 특유의 계층적 구조로 인해 생성된 기공 채널 덕분에 황화 카드뮴 (CdS), 셀레나이드화 카드뮴 (CdSe) 등 광흡수 무기물 및 액체 전해질이 TiO_2 막 안쪽까지 빠른 침투가 가능해져 광수확 특성이 증가하고 생성된 전자의 수명이 비약적으로 상승하는 효과를 얻었다. 이러한 TiO_2 광전극 물질의 독특한 구조로 인하여 전자-정공 재결합 억제 및 효율적인 전하 수집이 이루어졌으며, 결과적으로 기존 대비 매우 높은 광·전 변환 효율을 얻을 수 있었다. NiO 의 경우, PLD 증착법을 통해 높은 투과도를 갖는, (111)면 방향으로 우선 성장된, 기둥 모양의 NiO 나노 구조체를 합성하였고 이들을 페로

브스카이트 태양 전지의 정공 전달층 (hole transporting layer)으로 사용하기 위한 최적화 연구를 통하여 페로브스카이트 태양전지의 전극 물질로서의 가능성을 제시하였다. 디바이스의 경우 NiO 전극을 정공 전달층으로 사용하여 NiO/MAPbI₃/PCBM 다층 구조 형태의 태양 전지를 제작하였다. NiO 박막 (thin film) 혹은 포러스 (porous) 막과 비교해 보았을 때, NiO 나노 구조체 막을 전극으로 한 태양 전지의 경우 광·전 변환 효율이 비약적으로 증가하는 것을 확인하였다. 이는 나노 구조체 막의 두꺼운 두께로 인한 효과적인 전자 차단 능력과 두꺼우면서도 효과적으로 생성된 정공을 추출 및 수집하는 능력에 기인한 결과이다. 이러한 결과 나노 구조체 NiO 막을 기반으로 변환 효율 17.3%의 고효율 태양 전지 제작에 성공하였다.

둘째로, TiO₂ 산화물 반도체의 조성 제어를 통해 무기 광흡수 층과 전하 수집 물질 사이의 전하 주입 능력 향상시켜 태양 전지의 전하 수집 능력 및 효율 개선 가능성을 제시하였다. 본 연구에서는 태양 전지에서 무기 광흡수 물질과 TiO₂의 전도대 (conduction band) 차이는 무기 광흡수층에서 생성된 전자가 TiO₂로 전달되는 추진력 (driving force) 이라는 점과 TiO₂에 금속 양이온 도핑을 하면 TiO₂의 전도대가 변한다는 점에 착안하여, 니오븀 (Niobium) 도핑을 통하여 TiO₂ 전도대를 변화시켜 태양 전지 내에서의 전하 주입 능력 향상을 도모하였다. 니오븀 도핑으로 인한 TiO₂의 에너지 밴드 변형과 태양 전지 변환 효율의 상관 관계에 대해 연구하였다. 니오븀 도핑 결과, 도핑을 하지 않은 광전극에 비해 태양 전지에서 생성되는 광전류의 양이 약 41 % 정도 증가한 것을 확인할 수 있었다. 이러한 광전류 및 효율의 증가는 니오븀 도핑을 통해 TiO₂의 전도대가 낮아져 황화 납 (PbS)과 TiO₂ 사이의 전도대 차이가 커졌고, 그 결과 둘 사이의

전하 주입 능력이 향상된 것에 기인한 것이다.

본 연구는 태양전지에서 광전극으로 사용되는 산화물 반도체에 대한 연구이며, 구체적으로 이들의 구조 및 조성 설계 및 제어를 통해 소자의 전하 수집 특성 및 변환 효율 향상의 가능성으로 제시하였다. 이러한 구조 및 조성 제어를 통해 무기 감응형 및 페로브스카이트 태양전지의 광전극이 갖추어야 할 조건에 대한 방향성을 제시하였다. 이 연구를 통하여 현재 직면해 있는 차세대 태양 전지의 문제점 및 한계를 해결할 수 있는 가능성을 제시 하고자 한다.

주요어: 전하 수집, 산화물 반도체, 나노구조체, 펄스 레이저 증착법, 계층 구조, 광·전 에너지 변환, 무기 감응형 태양 전지, 페로브스카이트 태양 전지, 도핑, 황화 카드뮴, 셀레나이드화 카드뮴, 황화 납, 메틸암모늄 납 요오드화물, 이산화 티타늄, 산화 니켈

학 번: 2008-22848

Research Achievements

1) Refereed Papers

18. **J. H. Park**[†], J. Seo[†], S. Park, S. S. Shin, Y. C. Kim, N. J. Jeon, H. –W. Shin, T. K. Ahn, J. H. Noh, S. C. Yoon, C. S. Hwang and S. I. Seok*, “Efficient CH₃NH₃PbI₃ Perovskite Solar Cells Employing Nanostructured p-type NiO Electrode Formed by a Pulsed Laser Deposition”, *Adv. Mater.*, **2015**, DOI: 10.1002/adma.201500523.
17. S. S. Shin[†], W. S. Yang[†], J. H. Noh, J. H. Seok, N. J. Jeon, **J. H. Park**, J. S. Kim, W. M. Seong, Y. C. Joo and S. I. Seok*, “High performance flexible perovskite solar cells exploiting Zn₂SnO₄ prepared in solution below 100 °C as an electron transporting layer”, *Nat. Commun.*, **2015**, DOI:10.1038/ncomms8410.
16. D. H. Kim, H. S. Han, I. S. Cho, W. M. Seong, I. J. Park, **J. H. Park**, S. Shin, G. D. Park, S. Park, S. Lee*, K. S. Hong*, “CdS-sensitized 1-D single-crystalline anatase TiO₂ nanowire arrays for photo-electrochemical hydrogen production” *Int. J. Hydrogen Energy* **2015**, 40, 863.
15. M. H. Lee[†], **J. H. Park**[†], H. S. Han, H. J. Song, I. S. Cho, J. H. Noh*, K. S. Hong*, “Nanostructured Ti-doped hematite (α -Fe₂O₃) photoanodes for

- efficient photo-electrochemical water oxidation” *Int. J. Hydrogen Energy* **2014**, 39, 17501.
14. **J. H. Park**, D. H. Kim, S. S. Shin, H. S. Han, M. H. Lee, H. S. Jung, J. H. Noh*, K. S. Hong*, “A Hierarchically Organized Photoelectrode Architecture for Highly Efficient CdS/CdSe-Sensitized Solar Cells” *Adv. Energy Mater.* **2014**, 4, 1300395.
13. S. S. Shin, D. W. Kim, **J. H. Park**, D. H. Kim, J. S. Kim, K. S. Hong*, I. S. Cho*, “Anionic Ligand Assisted Synthesis of 3-D Hollow TiO₂ Architecture with Enhanced Photoelectrochemical Performance” *Langmuir* **2014**, 30, 15531.
12. G. S. Han, S. Lee, J. H. Noh, H. S. Chung, **J. H. Park**, B. S. Swain, J. -H. Im, N. -G. Park, H. S. Jung*, “3-D TiO₂ nanoparticle/ITO nanowire nanocomposite antenna for efficient charge collection in solid state dye-sensitized solar cells” *Nanoscale* **2014**, 6, 6127.
11. M. J. Kim, **J. H. Park**, K. Y. Lee, S. Lee, G. S. Han, H. J. Song, H. Shin, T. K. Ahn, H. S. Jung*, “Cerium-Doped Yttrium Aluminum Garnet Hollow Shell Phosphors Synthesized via the Kirkendall Effect” *ACS Appl. Mater. Interfaces*, **2014**, 6, 1145.
10. S. Park, C. W. Lee, I. S. Cho, S. Kim, **J. H. Park**, H. J. Kim, D. -W. Kim, S. Lee, K. S. Hong*, “Growth of anatase and rutile TiO₂@Sb:SnO₂ heterostructures and their application in photo-electrochemical water splitting” *Int. J. Hydrogen Energy* **2014**, 39, 17508.

9. G. S. Han, S. Lee, D. W. Kim, D. H. Kim, J. H. Noh, **J. H. Park**, S. Roy, T. K. Ahn, H. S. Jung*, “A Simple Method To Control Morphology of Hydroxyapatite Nano- and Microcrystals by Altering Phase Transition Route” *Cryst. Growth Des.* **2013**, 13, 3414.
8. S. S. Shin, J. S. Kim, J. H. Suk, K. D. Lee, D. W. Kim, **J. H. Park**, I. S. Cho, K. S. Hong*, J. Y. Kim*, “Improved Quantum Efficiency of Highly Efficient Perovskite BaSnO₃-Based Dye-Sensitized Solar Cells” *ACS Nano* **2013**, 7, 1027.
7. **J. H. Park**, J. H. Noh*, B. S. Han, S. S. Shin, I. J. Park, D. H. Kim, K. S. Hong*, “Influence of Niobium Doping in Hierarchically Organized Titania Nanostructure on Performance of Dye-Sensitized Solar Cells” *J. Nanosci. Nanotechnol.*, **2012**, 12, 5091.
6. J. H. Noh, **J. H. Park**, H. S. Han, D. H. Kim, B. S. Han, S. Lee, J. Y. Kim*, H. S. Jung*, K. S. Hong, “Aligned Photoelectrodes with Large Surface Area Prepared by Pulsed Laser Deposition” *J. Phys. Chem. C* **2012**, 116, 8102.
5. S. S. Shin, D. W. Kim, S. Lee, I. S. Cho*, D. H. Kim, **J. H. Park**, K. S. Hong*, “Surface Modified TiO₂ Nanostructure with 3D Urchin-Like Morphology for Dye-Sensitized Solar Cell Application” *J. Nanosci. Nanotechnol.*, **2012**, 12, 1305.
4. B. H. Kim, J. H. Park, B. Kim, D. -K. Kwon*, “Dielectric and Piezoelectric Properties of Low-Temperature Sintered Lead Zirconate Titanate Ceramics

with 0.78PbO-0.22CuO Flux Addition” *Met. Mater. Int.* **2012**, 18, 1067.

3. J. H. Noh, B. Ding, H. S. Han, J. S. Kim, **J. H. Park**, S. Park, H. S. Jung, J. -K. Lee*, K. S. Hong*, “Tin doped indium oxide core—TiO₂ shell nanowires on stainless steel mesh for flexible photo-electrochemical cells” *Appl. Phys. Lett.* **2012**, 100, 084104.
2. D. H. Kim, S. Lee, **J. H. Park**, J. H. Noh, I. J. Park, W. M. Seong, K. S. Hong*, “Transmittance optimized Nb-doped TiO₂/Sn-doped In₂O₃ multilayered photoelectrodes for dye-sensitized solar cells” *Sol. Energ. Mat. Sol. C* **2012**, 96, 276.
1. J. H. Noh, H. S. Han, S. Lee, D. H. Kim, **J. H. Park**, S. Park, J. Y. Kim, H. S. Jung*, K. S. Hong*, “A Newly Designed Nb-Doped TiO₂/Al-Doped ZnO Transparent Conducting Oxide Multilayer for Electrochemical Photoenergy Conversion Devices” *J. Phys. Chem. C* **2010**, 114, 13867.

2) Patents

6. S. Lee, I. J. Park, **J. H. Park**, D. H. Kim, D. K. Lim, T. H. Noh, K. S. Hong, G. S. Han, H. S. Jung, “Nano tube material composed of titanium oxide and Method of manufacturing the same” Korean Patent 10-12772790000 (2013).
5. K. S. Hong, J. H. Suk, S. Park, **J. H. Park**, I. S. Cho, D. W. Kim, “Method of preparing Sn-based oxide semiconductor nanopowder and method of

manufacturing photoelectric electrode using Sn-based oxide semiconductor nanopowder” U. S. Patent 13/546,833 (2012).

4. S. Lee, I. J. Park, **J. H. Park**, D. H. Kim, D. K. Yim, T. H. Noh, K. S. Hong, K. S. Han, H. S. Jung, “Titanium oxide nano tube material and method for manufacturing the same” U. S. Patent 13/197,966 (2011)

3. J. H. Noh, S. Park, H. S. Han, **J. H. Park**, J. M. Cho, S. T. Bae, I. S. Cho, S. Lee, D. K. Lee, K. S. Hong, “Substrate having an antistatic function and method for manufacturing the same” Korean Patent 10-10738780000 (2011).

2. S. Park, S. Lee, H. S. Jung, I. S. Cho, J. H. Noh, D. W. Kim, D. Kim, **J. H. Park**, K. S. Hong, “Flexible transparent electrode with good conductivity and transparency and manufacturing method thereof” Korean Patent 10-10946350000 (2011).

1. H. S. Han, J. H. Noh, J. S. Kim, **J. H. Park**, B. S. Han, K. S. Hong, “Soluble dye-sensitized solar cell and a manufacturing method using a transparent polymer film” Korean Patent 10-2011-0053408 (2011).

3) Presentations at Technical and Professional Meetings

21. **J. H. Park**, M. H. Lee, S. S. Shin, D. H. Kim, J. H. Noh, K.S. Hong, “Doping Titanium Dioxide Nanostructures with Niobium for Enhanced

- Inorganic Semiconductor Sensitized Solar Cell Performance”
NanotechItaly, Nov 27-29, 2013, Venice, Italy.
20. M. H. Lee*, **J. H. Park***, J. H. Noh, H. J. Song, H. S. Han, S. Shin, K. S. Hong, “Fabrication of oriented hematite nanostructured films as photoanodes for photo-electrochemical water oxidation” *Nanosmat-Asia*, Mar 13-15, 2013, Wuhan, China.
19. D. H. Kim, W. M. Seong, **J. H. Park**, I. J. Park, S. S. Shin, K. S. Hong, “CdS/ZnS quantum dot-sensitized anatase single crystalline 1-D TiO₂ nanowires for photoelectrochemical hydrogen production” *Nanosmat-Asia*, Mar 13-15, 2013, Wuhan, China.
18. I. J. Park, D. H. Kim, **J. H. Park**, W. M. Seong, “Enhanced photoelectrochemical efficiency with CdS QDs sensitized preferred-oriented TiO₂ nanotube arrays” *Nanosmat-Asia*, Mar 13-15, 2013, Wuhan, China.
17. B. S. Han, J. H. Noh, **J. H. Park**, K. S. Hong, “Direct fabrication of hierarchical zinc oxide nanostructure at room temperature for dye sensitized solar cell” *2012 MRS Fall Meeting and Exhibit*, Nov 25-30, 2012, Boston, USA.
16. D. H. Kim, W. M. Seong, H. S. Han, **J. H. Park**, I. J. Park, S. S. Shin, I. S. Cho, S. Lee, K. S. Hong, “CdS/CdSe/ZnS Quantum dot-sensitized anatase single crystalline branched-TiO₂ nanowire for photoelectrochemical hydrogen production” *7th Nanosmat*, Sep 18-21, 2012, Prague, Czech

Republic.

15. D. H. Kim, W. M. Seong, H. S. Han, **J. H. Park**, I. J. Park, S. S. Shin, I. S. Cho, S. Lee, K. S. Hong, "CdS Quantum Dot-Sensitized anatase single crystalline Branched-TiO₂ nanowires for Photoelectrochemical Hydrogen Production" *TechConnect World Summit, Expo & Showcase*, Jun 18-21, 2012, Santa Clara, USA.
14. **J. H. Park**, D. H. Kim, S. S. Shin, S. H. Han, H. S. Jung, J. H. Noh, K. S. Hong, "Highly Efficient CdS/CdSe Quantum-Dot Sensitized Solar Cell with Hierarchically Organized TiO₂ nanostructured films" *E-MRS Spring Meeting and Exhibit*, May 15-17, 2012, Strasbourg, France.
13. **J. H. Park**, J. H. Noh, D. H. Kim, S. S. Shin, S. H. Han, H. S. Jung, K. S. Hong, "Highly Efficient CdS/CdSe Quantum-Dot Sensitized Solar Cells with Hierarchically Organized TiO₂ Nanostructured Films" *2011 MRS Fall Meeting and exhibit*, Nov 18-Dec 2, 2011, Boston, USA.
12. S. S. Shin, D. W. Kim, S. Lee, D. H. Kim, **J. H. Park**, I. S. Cho, K. S. Hong, "Synthesis of 3D Chestnut Bur-like Rutile TiO₂ for Dye-sensitized Solar Cells" *The 3rd International Conference on Advanced Electromaterials (ICAE)*, Nov 7-10, 2011, Jeju, Korea.
11. B. S. Han, J. H. Noh, **J. H. Park**, K. S. Hong, "Room Temperature Fabrication of Mesoporous ZnO Vertical Array for Dye-Sensitized Solar Cells" *The 3rd International Conference on Advanced Electromaterials (ICAE)*, Nov 7-10, 2011, Jeju, Korea.

10. **J. H. Park**, J. H. Noh, K. S. Hong, "Hierarchically Organized M-doped TiO₂ (M=V, Nb, Ta) Photoelectrode for Dye-Sensitized Solar Cells" *Global Photovoltaic Conference (GPVC)*, Sep 28-30, 2011, Busan, Korea.
9. S. S. Shin, H. J. Song, D. W. Kim, S. Lee, I. S. Cho, **J. H. Park**, K. S. Hong, "Synthesis of Nanostructured TiO₂ and Their Surface Modification for Dye-Sensitized Solar Cells (DSSCs)" *Global Photovoltaic Conference (GPVC)*, Sep 28-30, 2011, Busan, Korea.
8. J. H. Noh, H. S. Han, S. Lee, D. H. Kim, **J. H. Park**, S. Park, K. S. Hong, "Dye Sensitized Solar Cells Employing Nb-doped TiO₂/Al-doped ZnO Transparent Conducting Multilayer Films" *35th international conference and exposition on advanced ceramics and composites (ICACC)*, Jan 23-28, 2011, Daytona Beach, Florida, USA.
7. **J. H. Park**, J. H. Noh, B. S. Han, D. H. Kim, S. S. Shin, K. S. Hong, "Hierarchically Organized M-doped Titanium Dioxide (M=V, Nb, Ta) Photoelectrode for Dye-Sensitized Solar Cells" *5th International Conference on Surfaces, Coatings and Nanostructured Materials*, Oct 19-21, 2010, Reims, France.
6. S. S. Shin, I. S. Cho, S. Lee, D. W. Kim, **J. H. Park**, K. S. Hong, "3D Urchin-like Rutile TiO₂ and its Surface modified Nanostructures: Synthesis, Characterization and Evaluation of dye-sensitized solar cells performance" *International Union of Materials Research Societies - International Conference on Electronic Materials (IUMRS-ICEM)*, Aug 22-27, 2010, KINTEX, Korea.

5. J. H. Noh, **J. H. Park**, H. S. Han, S. Lee, D. H. Kim, H. S. Jung, K. S. Hong, "Hierarchically organized nanostructured photoelectrode by laser ablation for photovoltaic device" *International Union of Materials Research Societies - International Conference on Electronic Materials (IUMRS-ICEM)*, Aug 22-27, 2010, KINTEX, Korea.
4. D. H. Kim, S. Lee, J. H. Noh, **J. H. Park**, D. K. Lim, K. S. Hong, "Dense TiO₂ layer to improve the transmittance of Nb-doped TiO₂ / Sn doped indium Oxide Multilayered photoelectrodes for the Dye-sensitized Solar Cells" *18th International Conference on Photochemical Conversion and Storage of Solar Energy (IPS)*, Jul 25-30, 2010, Seoul, Korea.
3. H. S. Han, J. H. Noh, **J. H. Park**, J. S. Kim, K. S. Hong, "Synthesis of TiO₂ nanostructures by pulsed laser deposition for organic photovoltaic cells" *217th ECS Meeting*, Apr 25-30, 2010, Vancouver, Canada.
2. J. H. Noh, **J. H. Park**, H. S. Han, S. Lee, D. H. Kim, H. S. Jung, K. S. Hong, "Synthesis of hierarchically organized nanostructured TiO₂ by pulsed laser deposition and its application to dye-sensitized solar cells" *3rd IEEE International Nanoelectronics Conference*, Jan 3-8, 2010, Hong Kong.
1. **J. H. Park**, J. H. Noh, K. S. Hong, "Structural and Photoluminescent Properties of Y₃Al₅O₁₂:Ce Thin Films prepared using Pulsed Laser Deposition" *Joint Symposium of International Workshop on Piezoelectric Materials and Applications in Actuators (IWPMA 2009) & International Symposium on Electroceramics (ISE 2009)*, Nov 8-11, 2009, Jeju, Korea.